

---


Electronic Theses and Dissertations, 2004-2019

---

2009

## Effect of Sodium And Absorber Thickness on Cigs2 Thin Film Solar Cells

Parag Vasekar  
*University of Central Florida*

 Part of the [Engineering Science and Materials Commons](#), and the [Mechanical Engineering Commons](#)  
Find similar works at: <https://stars.library.ucf.edu/etd>  
University of Central Florida Libraries <http://library.ucf.edu>

This Doctoral Dissertation (Open Access) is brought to you for free and open access by STARS. It has been accepted for inclusion in Electronic Theses and Dissertations, 2004-2019 by an authorized administrator of STARS. For more information, please contact [STARS@ucf.edu](mailto:STARS@ucf.edu).

---

### STARS Citation

Vasekar, Parag, "Effect of Sodium And Absorber Thickness on Cigs2 Thin Film Solar Cells" (2009).  
*Electronic Theses and Dissertations, 2004-2019*. 6134.  
<https://stars.library.ucf.edu/etd/6134>

**EFFECT OF SODIUM AND ABSORBER THICKNESS ON CIGS2 THIN  
FILM SOLAR CELLS**

by

PARAG S. VASEKAR  
M.S. Vanderbilt University , 2004

A dissertation submitted in partial fulfillment of the requirements  
for the degree of Doctor of Philosophy  
in the Department of Mechanical Materials and Aerospace Engineering  
in the College of Engineering and Computer Science  
at the University of Central Florida  
Orlando, Florida

Spring Term  
2009

Major Professor: Neelkanth G. Dhere.

© 2009 Parag S. Vasekar

## ABSTRACT

Chalcopyrites are important contenders among solar cell technologies due to direct band gap and higher absorption coefficient.  $\text{CuIn}_{1-x}\text{Ga}_x\text{S}_2$  (CIGS2) thin-film solar cells are of interest for space power applications because of near optimum bandgap of 1.5 eV for AM0 solar radiation outside the earth's atmosphere. The record efficiency of 11.99% has been achieved on a 2.7  $\mu\text{m}$  CIGS2 thin film prepared by sulfurization at FSEC PV Materials Laboratory. Since CIGS2 films are typically grown in copper-rich regime, excess cuprous sulfide which helps in the formation of CIGS2 is etched away. This makes CIGS2 nearly stoichiometric. However, it is difficult to adjust Cu/(In+Ga) ratio in the desired range 0.7 to 0.9. A solution to this is to grow CIGS2 in copper-deficient regime. However, it is difficult to produce device quality films without the support of cuprous sulfide. This work is one of the very few attempts in which device quality films were formed even in copper-deficient regimes with the addition of sodium. Also, recent research endeavors in the CIGS2 thin film photovoltaic community are directed towards thinner films because the availability and cost of indium as well as gallium are limiting factors. The required amounts of rare and expensive metals can be lowered by using thinner films. The solar cell performance in the thinner absorbers deteriorates due to the detrimental effects of the larger fraction of grain boundaries. It is essential to hasten the grain growth through coalescence to retain high efficiency in devices prepared using thinner films. Large grain size that is desirable for obtaining high efficiency cells can be achieved by creating conditions of fewer nucleation sites and large mobilities of the deposited species. Sodium has been found to play a vital role by enhancing the atomic mobility and improving the coalescence even in thinner films. This work

presents a study of morphology and device properties of CIGS<sub>2</sub> thin films with Copper-deficient absorbers after minute amounts of sodium are introduced on the Mo-coated substrate in the form of sodium fluoride layer prior to sputter deposition of copper-gallium alloy and indium. Photovoltaic conversion efficiency of 9.15% was obtained for copper-deficient absorbers. In a parallel set of experiments, copper-rich precursors were used to produce absorbers of lower thickness range values and the parameters were optimized. Photovoltaic conversion efficiency of 10.12% was obtained for an absorber of thickness 1.5  $\mu\text{m}$  and an efficiency of 9.62% was obtained for an absorber of thickness 1.2  $\mu\text{m}$ .

## **ACKNOWLEDGMENTS**

I would like to take this opportunity to express my deepest gratitude towards Dr. Neelkanth G. Dhere, for giving me this opportunity to work on this project. I enjoyed working under his supervision and appreciate his constant guidance and encouragement. I would like to thank Dr. Helge Heinrich, Dr. Christine Klemenz, Dr. Kalapathy Sundaram and Dr. Arvinda Kar for serving on my final examination committee and for their invaluable suggestions. This research work was supported by National renewable Energy Laboratory (NREL). I would like to thank the following people for their assistance on this project: Helio Moutinho and Bobby To from National Renewable Energy laboratory. Special words of thanks go to Mr. Sachin Kulkarni, Mr. Shirish Pethe, Mr. Vinay Hadagali, Mr. Bhaskar Kumar and Mr. Ashwani Kaul at Florida Solar Energy Center (FSEC).

I have enjoyed working at PV Materials Laboratory of Florida Solar Energy Center. Finally I would like to thank my parents and friends for their support.

## TABLE OF CONTENTS

LIST OF FIGURES .....	ix
LIST OF TABLES .....	xiii
LIST OF ACRONYMS/ABBREVIATIONS .....	xiv
1. INTRODUCTION .....	1
1.1 Overview of Photovoltaics.....	1
1.2. Basics of a solar cell .....	3
1.3 Solar radiation.....	5
1.4. Semiconductors and band structure .....	7
1.4.1. Homojunction .....	11
1.4.2. Heterojunction.....	14
1.5. Current-voltage characteristics .....	16
1.6. Motivation and definition of scientific problem .....	24
2. MATERIALS REVIEW .....	30
2.1 CIGS <sub>2</sub> thin film solar cells .....	30
2.2 Optical properties.....	31
2.3 Crystal Structure .....	32
2.4 Phase diagram .....	34
2.4 Heterojunction partner – Cadmium sulfide (CdS) .....	36
2.5 Transparent conducting oxide window bilayer– intrinsic ZnO and Zinc oxide doped with aluminum (ZnO:Al) .....	37

3. EXPERIMENTAL TECHNIQUE .....	39
3.1 Substrate preparation .....	39
3.2. NaF deposition .....	40
3.3 Deposition of Copper gallium and indium metallic precursors .....	40
3.4. Sulfurization.....	41
3.5. CdS deposition.....	42
3.6. Front contact bilayer deposition.....	44
3.7. Contact Fingers deposition .....	44
3.8. Antireflection coating .....	45
3.9. Materials Characterization.....	46
3.10. Current-Voltage characterization.....	47
3.11. Electrical characterization.....	47
4. RESULTS AND DISCUSSIONS.....	49
4.A. Cu-deficient CIGS <sub>2</sub> absorbers .....	49
4.A.1 Introduction.....	49
4.A.2. Materials Characterization .....	49
4.A.3. Photovoltaic characteristics.....	56
4.B. Cu-rich thinner CIGS <sub>2</sub> absorbers.....	64
4.B.1. Introduction .....	64
4.B.2. Optimization of precursor thickness .....	65
4.B.3. Optimization of undoped-ZnO thickness .....	65
4. B.4. Introduction of post-sulfurization dwell.....	66
4. B.5. Materials Characterization .....	66



4. B.6. Electrical characterization .....	74
4. B.7. Photovoltaic Characterization of the highest efficiency cells .....	81
5. CONCLUSIONS AND RECOMMENDATIONS FOR FUTURE WORK.....	86
5.1 Conclusions.....	86
5.2. Recommendations for future work .....	88
REFERENCES .....	89

## LIST OF FIGURES

Figure 1 : Solar spectrum.....	5
Figure 2 : Standard AM 1.5 Solar Spectrum.....	6
Figure 3 : Bandgap in a semiconductor .....	8
Figure 4 : Homojunction in a semiconductor .....	11
Figure 5 : Semiconductor heterojunction.....	14
Figure 6 : I -V characteristic of solar cell in dark and under illumination drawn in forth quadrant .....	20
Figure 7 : Equivalent circuit of a solar cell.....	21
Figure 8 : Effect of series and shunt resistance on current-voltage curve .....	22
Figure 9 : Alpha phase widening due to sodium addition in CIGSeS .....	26
Figure 10 : Dependence of the absorption coefficient on the photon energy for selected semiconductors [6].....	32
Figure 11 : Schematic diagram of the crystal structure of $\text{CuInS}_2$ .....	33
Figure 12 : Ternary component diagram of Cu-In-S [60].....	35
Figure 13 : Pseudo binary phase diagram of $\text{Cu}_2\text{S-In}_2\text{S}_3$ [60]. .....	36
Figure 14 : DC and RF magnetron sputtering units.....	41
Figure 15 : Sulfurization furnace .....	42
Figure 16 : Set-up for the Chemical Bath Deposition.....	43
Figure 17 : Thermal evaporation setup. ....	45
Figure 18 : Cross-sectional view of CIGS2 thin film solar cell.....	46
Figure 19 : Optical micrographs of a sample without NaF.....	50

Figure 20 : Optical micrographs of a sample with 40 Å NaF .....	50
Figure 21 : Optical micrographs of a sample with 80 Å NaF .....	51
Figure 22 : Optical micrographs of a sample with 120 Å NaF .....	51
Figure 23 : SEM images of a sample without NaF .....	52
Figure 24 : SEM images of a sample with 40 Å NaF .....	53
Figure 25 : SEM images of a sample with 80 Å NaF .....	53
Figure 26 : SEM images of a sample with 120 Å NaF .....	54
Figure 27 : XEDS spectra of indium rich hillocks region .....	54
Figure 28 : XEDS spectra of film .....	55
Figure 29 : XRD patterns of CIGS2 thin films for A] without NaF, B] 40 Å NaF, C] 80 Å NaF and with D] 120 Å NaF .....	56
Figure 30 : I-V characteristics for sample without NaF .....	57
Figure 31 : Q-E characteristics for sample without NaF .....	58
Figure 32 : I-V characteristics for sample with 40 Å NaF .....	58
Figure 33 : Q-E characteristics for sample with 40 Å NaF .....	59
Figure 34 : I-V characteristics for sample with 80 Å NaF .....	60
Figure 35 : Q-E characteristics for sample with 80 Å NaF .....	60
Figure 36 : Trends in performance after addition of 80 Å NaF .....	61
Figure 37 : I-V characteristics for sample with 120 Å NaF .....	61
Figure 38 : Q-E characteristics for sample with 120 Å NaF .....	62
Figure 39 : Trends in performance after addition of 120 Å NaF .....	62
Figure 40 : Comparative Q-E curves .....	63
Figure 41 : 1.5 μm absorber sample without dwell. ....	67

Figure 42 : 1.5 $\mu\text{m}$ absorber sample with end dwell at 500°C for 30 minutes.....	67
Figure 43 : 1.2 $\mu\text{m}$ absorber sample with end dwell at 500°C for 30 minutes.....	68
Figure 44 : XRD spectra for 1.5 $\mu\text{m}$ and 1.2 $\mu\text{m}$ absorbers (with end dwell) .....	69
Figure 45 : AES depth profile for a 1.5 $\mu\text{m}$ absorber sample (with end dwell) .....	70
Figure 46 : AES depth profile for a 1.2 $\mu\text{m}$ absorber sample (with end dwell) .....	70
Figure 47 : TEM overview of the 1.2 $\mu\text{m}$ absorber sample solar cell .....	71
Figure 48 : TEM cross-section of the sample .....	72
Figure 49 : TEM image showing position of the line scan in the cross-section .....	72
Figure 50 : Line profile of the components of the solar cell against the position on the line.....	73
Figure 51 : I-V characteristics of the 1657 cell.....	74
Figure 52 : Plot of $dJ/dV$ v/s $V$ .....	75
Figure 53 : Plot of the diode factor, $A$ and reverse saturation current, $J_0$ versus $\ln [J (\text{dark})]$ ....	76
Figure 54 : Bandgap determination.....	76
Figure 55 : $1/C^2$ versus $V$ .....	77
Figure 56 : Carrier density dependence on position relative to the junction. ....	77
Figure 57 : Fermi level relative to the valence band as a function of distance from the p-n junction. ....	78
Figure 58 : LBIC images.....	79
Figure 59 : LBIC at different operating biases. ....	79
Figure 60 : High resolution of the square portion from Figure 59.....	80
Figure 61 : Cross-sections of the features shown in Figure 60.....	81
Figure 62 : I-V characteristics of CIGS2 solar cell of 1.5 $\mu\text{m}$ absorber (with end dwell).....	82
Figure 63 : Q-E characteristics of CIGS2 solar cell of 1.5 $\mu\text{m}$ absorber (with end dwell) .....	83

Figure 64 : I-V characteristics of CIGS2 solar cell of 1.2 $\mu\text{m}$ absorber (with end dwell).....	83
Figure 65 : Q-E characteristics of CIGS2 solar cell of 1.2 $\mu\text{m}$ absorber (with end dwell) .....	84
Figure 66 : Trends in photovoltaic performance towards optimization of 1.5 $\mu\text{m}$ Cu-rich CIGS2 films .....	85

## LIST OF TABLES

Table I : Photovoltaic characteristics showing effect of addition of sodium.....	63
Table II : Trade-off showing efficiency and material consumption/sputtering time .....	87

## LIST OF ACRONYMS/ABBREVIATIONS

ACRONYM	Definition of Acronym
CIS	Copper indium diselenide
CIGS	Copper indium gallium diselenide
CIGS <sub>2</sub>	Copper indium gallium disulfide
CIGSS	Copper indium gallium selenide sulfide
CdS	Cadmium sulfide
ZnS	zinc sulfide
i:ZnO	intrinsic zinc oxide
ZnO:Al	Aluminum doped zinc oxide
Cu	Copper
In	indium
Ga	Gallium
Se	Selenium
S	Sulfur
Mo	molybdenum
DESe	Diethylselenide
FCC	Face centered cubic
V <sub>oc</sub>	Open circuit voltage
J <sub>sc</sub>	Short circuit current density
FF	Fill Factor
R <sub>s</sub>	Series resistance

R <sub>p</sub>	Shunt resistance
kV	kilo volts
eV	electron volts
EPMA	Electron Probe Micro Analysis
SEM	Scanning Electron Microscopy
AES	Auger Electron Spectroscopy
XEDS	X-ray Energy Dispersive Spectroscopy
XRD	X-ray diffraction
nm	nano meter (10 <sup>-9</sup> meter)
μm	micro meter (10 <sup>-6</sup> meter)
°C	Degree Celsius
X	times
%	percentage



# **1. INTRODUCTION**

## **1.1 Overview of Photovoltaics**

Mankind is always in the quest of renewable sources of energy. Most of the energy that is generated today is obtained as derivatives of fossil fuels (coal, oil, natural gas). Worldwide demand for energy is growing continuously, while the utilization of the conventional energy resources may have reached its peak and its exhaustion may be on the offing. Also, there is release of greenhouse gases into the atmosphere due to burning of fossil fuels, while environmental problems are caused by uranium and the storage or disposal of nuclear waste. The interference of mankind with nature has reached a level that requires urgent re-evaluation of possible energy supply strategies with a focus on sustainability, unless major changes in climate and environment are accepted. Solar energy is the Earth's major renewable energy resource and abundantly available. Therefore, the exploitation of the energy irradiated by the Sun is the potential key to a sustainable energy production in future. There is no emission of toxic or greenhouse gases during the conversion of sunlight into electricity using photovoltaic cells, nor is there any noise pollution. Photovoltaic systems can be installed in principle wherever the solar insolation is adequate, in urban or rural, grid-connected or stand-alone configurations, the electricity produced can be used locally or fed into the grid, and the electricity generation is decentralized and therefore, less vulnerable. In contrast to these numerous advantages, Photovoltaics has to face really only three drawbacks [1]:

- (i) The sunlight is intermittent and also depends on season, which is related to the lack of inexpensive and efficient methods to store electrical energy,
- (ii) Its cost, although prices for photovoltaic systems are dropping, and a fair cost evaluation including indirect costs and governmental subsidies is seldom taken into account, and
- (iii) The knowledge about this technology is not widely spread. .

Silicon technology for photovoltaics is the first generation technology, mostly because silicon is abundantly available and already was in the research phase because of microelectronics. Silicon is an indirect band-gap material (1.12 eV) and needs approximately 100  $\mu\text{m}$  for effective absorption of the solar spectrum. The production process for device grade silicon from silica is costly and also there is tough competition from the microelectronics industry. Laboratory level efficiency of 24.4% [2] has been reported for silicon, while the module level efficiency is 22.7% [3]. The silicon technology has been approaching lower limit in terms of the production costs. Thin film technology is the second generation technology. Since their inception in the seventies, thin-film solar cells were aimed to achieve a better power-to-weight ratio for space applications. Today, the drive towards the development of thin-film solar cells is mainly due to their potential to reduce manufacturing costs and material utilization. The earliest thin-film cells were based on  $\text{Cu}_2\text{S}/\text{CdS}$  [4]. But they suffered from poor stability owing to the high diffusivity of Copper. Amorphous hydrogenated silicon (a-Si:H) cells entered the market in the eighties [5]. Today they have able competitors in CdTe and Chalcopyrite-based cells [6]. One of the problems with thin-film materials other than a-Si:H is that they are not used elsewhere in the electronics industry. Therefore, little expertise is available [7] . Also, presently the most efficient (single-junction) thin-film solar cells are made with polycrystalline

$\text{CuIn}_{(1-x)}\text{Ga}_x\text{Se}_2$  (commonly abbreviated as  $\text{Cu}(\text{In,Ga})\text{Se}_2$  or CIGS) or CdTe absorbers. The highest efficiencies reported for CIGS solar cells to date are 19.2% [7], and 21.5% under concentrated sunlight (14 suns) [8]. With CdTe, cell efficiencies up to 16.5% were demonstrated [9]. Among the advantages of CIGS and CdTe cells over single-crystal Si cells is that sunlight is absorbed much more efficiently in these compounds owing to their direct band gap, such that absorber thickness of a few microns is sufficient to absorb most of the useful part of the sunlight. The required layers are so thin that the cells are flexible when grown on a sufficiently thin substrate. Solar cells are small-area devices. Since the electrical current delivered by a solar cell depends on the illuminated area, the cell cannot be made arbitrarily large without suffering severe current loss due to the limited conductivity of the transparent conducting front contact. Therefore, individual small-area cells must be connected in series, which results in a large-area device that delivers comparatively high voltages and low currents. The energy required for the fabrication of thin-film modules is comparatively small. Third generation solar cells include multiple band gap and quantum dot solar cells [1], as well as organic and dye-sensitized solar cells.

## **1.2. Basics of a solar cell**

A solar cell is nothing but a p-n junction diode which produces electricity upon incidence of light. This property of a solar cell makes it one of the most important resources of renewable energy, which is capable of utilizing the abundantly available sunlight and thereby contribute towards solving the energy problems. Absorption of a quantum of sunlight having energy  $h\nu$  greater than the bandgap  $E_g$  of the semiconductor results in the excitation of an electron from the valence band to the conduction band. Here  $h$  is the Planck's constant and  $\nu$  is the frequency of

the absorbed light quantum. The excitation of the electron leaves behind a hole in the valence band. A semiconductor such as silicon can be doped with a donor impurity such as phosphorus to obtain a n-type semiconductor in which the majority free charge carriers are electrons, while intrinsic point defects such as vacancies, interstitials and antisites act as dopants in the chalcopyrite type thin-film solar cells. A p-type semiconductor with holes as majority free charge carriers can be obtained for example by doping silicon with an acceptor impurity such as boron. When a p-type semiconductor is joined to an n-type semiconductor, holes from the p-region tend to diffuse to the n-region and electrons from the n-region tend to diffuse to the p-region because of the concentration gradients. Recombination of diffusing free carriers with the oppositely charged majority carriers creates a region depleted of free carriers. The dopant ions in the depletion regions are no more compensated. This gives rise to a barrier or built-in electric field which opposes further diffusion of free carriers. Electron-hole pairs generated within a diffusion length of the p-n junction region are separated by the built-in field at the junction. The photogenerated electrons from the p-type region diffuse towards the junction and are propelled to the n-type region by the field. Similarly holes from the n-type region diffuse towards the junction and are propelled to the p-type region by the field. The holes then flow towards the p-type contact where they recombine with electrons which have originated in the n-type region and have done work on an external load. Thus it can be seen that each photon of energy  $h\nu > E_g$  absorbed in the useful collection volume can provide one electron for flow in the external circuit.

If each photon incident on a solar cell had an energy  $h\nu$  equal to or slightly greater than the semiconductor bandgap  $E_g$ , the energy conversion will be very efficient. However, the solar spectrum extends from ultraviolet to infrared, virtually all the radiation energy being emitted in the wavelength range  $2 \times 10^{-7}$  to  $4 \times 10^{-6}$  m. The photons having energy  $h\nu < E_g$  are not absorbed

by the semiconductor. Moreover, for the absorbed photons with energy  $h\nu > E_g$  only the fraction equivalent to up to the bandgap  $E_g$  can be converted to electricity, the excess being lost as heat in the semiconductor. A lower bandgap semiconductor will absorb higher fraction of photons from the sunlight thus providing higher current but its voltage will be lower. On the other hand, a higher bandgap semiconductor will provide higher voltage. However, since it will absorb lower fraction photons from the sunlight, the current obtained from it will be lower. Hence it is necessary to choose an appropriate bandgap of a semiconductor for a terrestrial or space application.

### 1.3 Solar radiation

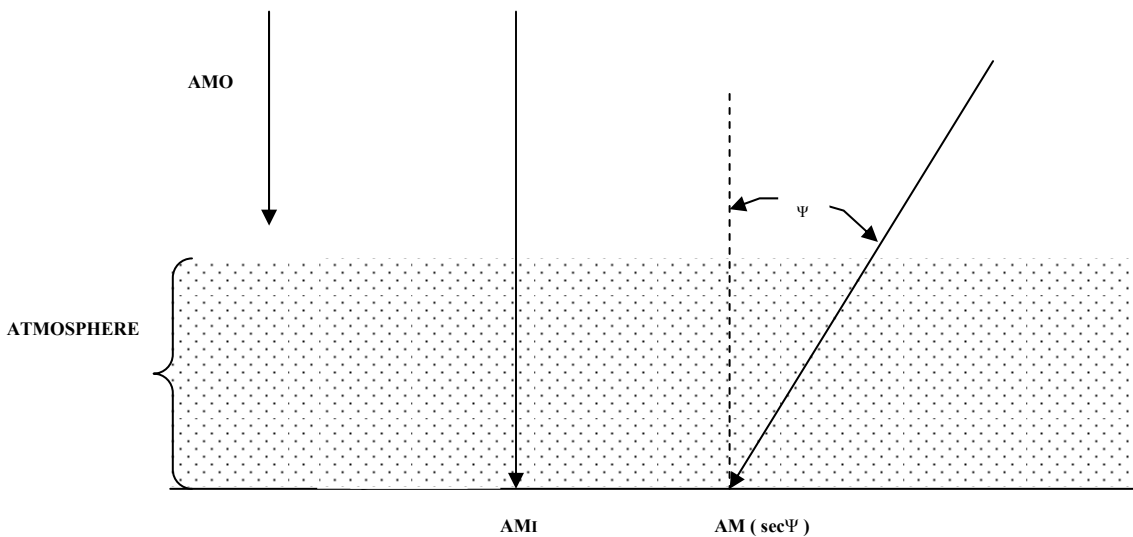


Figure 1 : Solar spectrum

In space the radiation intensity or the solar constant is  $1353 \text{ W/m}^2$  and is referred to as  $AM_0$ . The absorption of the spectrum increases with an increase in the thickness of the atmospheric layer. Air mass (AM) counts for the absorption in the atmosphere and how it affects the spectral content and intensity of the solar radiation entering the earth. For the thickness  $T_0$  of

the atmosphere, the path length T through the atmosphere for radiation from the sun incident at an angle  $\Psi$  relative to the normal to the earth's surface is given by [10],

$$T = T_0 / \cos \Psi,$$

The ratio T/T<sub>0</sub> is known as air mass co-efficient. The solar cells are generally evaluated for their performance at AM1.5 corresponding to the solar constant of 1 kW/m<sup>2</sup>. The solar constant on the earth's surface is always lower than that in space due to the spectral absorption by the atmosphere. Air Mass value at different earth location is given by the equation,

$$AM = (1 + (L/H)^2)^{1/2}$$

Where, L = Length of the shadow cast by an object of height H at that location.

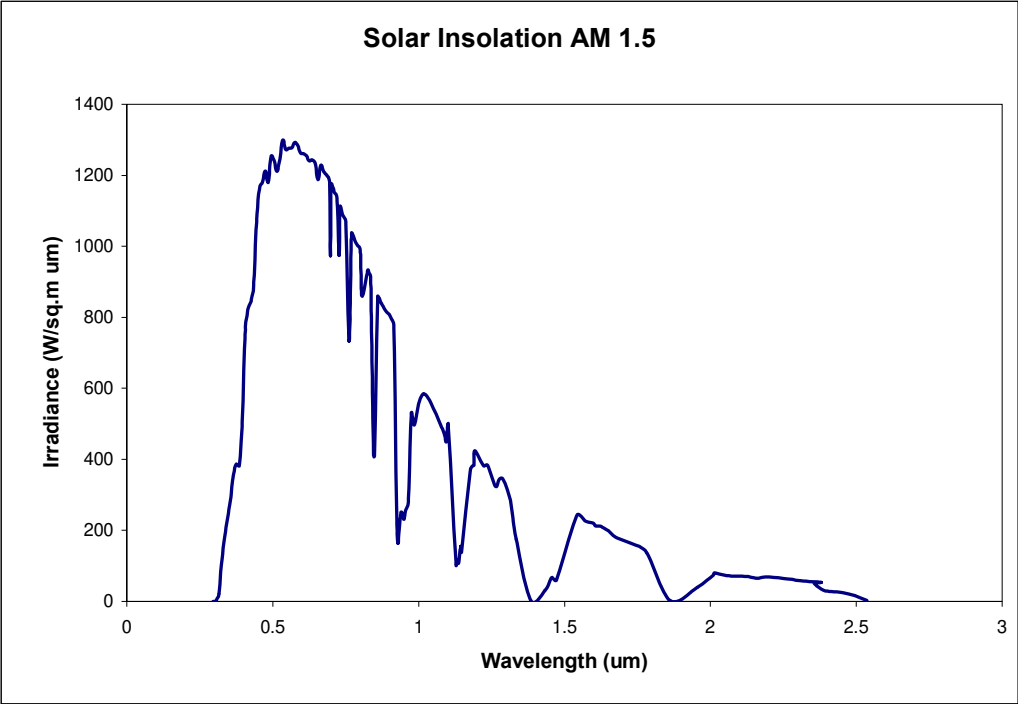


Figure 2 : Standard AM 1.5 Solar Spectrum

### 1.4. Semiconductors and band structure

In an atom, the positive charge lies on the nucleus and is compensated by electrons having negative charge, thus rendering the whole system electrically neutral. The electrons experience a Coulombic force by the nucleus, hence the electrons possess certain allowed energies. Electron of a free atom can occupy one of the series of energy levels below  $E = 0$ , given by [11],

$$E_n = \frac{-Z^2 m_o q^4}{8\epsilon_o^2 h^2 n^2} \dots\dots\dots (1)$$

Where,

$Z$  – atomic number,  $m_o$  - mass of free electron,  $q$  - charge of electron,  $\epsilon_o$  – permittivity of free space,  $h$  – Planck’s constant and  $n$  – positive integer representing energy levels.

According to Pauli’s exclusion principle each energy level can have a maximum two electrons with opposite spins. Hence at equilibrium not all the electrons fill the lowest energy level. These energy levels are further subdivided in sub-shells governed by the quantum numbers (Principal, Azimuthal, Magnetic and Spin).

Equation 1 indicates energy levels for an individual atom in isolation. However when the atoms are in the vicinity of each other, the energy levels start interacting. When two similar atoms having 2 electrons are brought together the energy level cannot accommodate 4 electrons as it violates Pauli’s exclusion principle. As a result of this interaction the energy level splits into two slightly separated energy levels. If  $N$  numbers of atoms interact then the original energy level is split into  $N$  different allowed energy levels to accommodate  $2N$  electrons. When the atomic spacing equals the crystal lattice spacing, the regions of allowed energy level are typically separated by a forbidden energy gap in which electrons cannot exist.

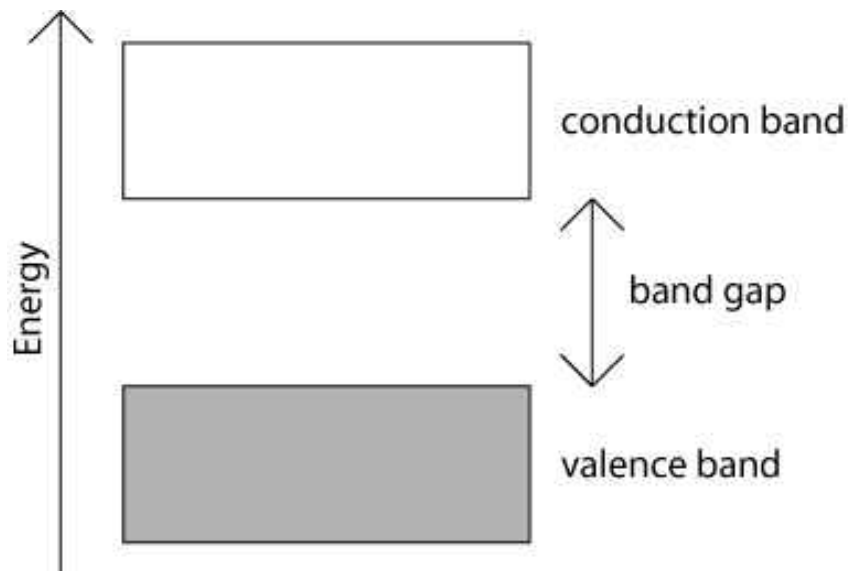


Figure 3 : Bandgap in a semiconductor

Semiconductors are materials with negative temperature coefficient. At  $T = 0$  K in a pure material, this gap separates one entirely filled band (valence band) from one that is entirely empty (conduction band). There exists a band gap,  $E_g$ . For  $T > 0$  K, a finite number of electronic states are occupied in the conduction band (“free electrons”) and a finite number of states are unoccupied in the valence-band (“free holes”). These free electrons and holes can get into motion since a quasi-continuum of higher or lower states are available to them respectively. They respond to electric fields and concentration gradients that allow for macroscopic current flow. The equilibrium concentrations of electrons and holes can be modified by extrinsic dopants, but also by defect levels (additional states within the band gap) that are intrinsic to the semiconductor. The occupation of conduction- and valence-band states is governed by Fermi-Dirac statistics [11]. Equation 2 describes the probability of electron occupation in the



conduction band and, similarly,  $1-f(E)$  describes the probability of finding holes in the valence band.

$$f(E) = \frac{1}{e^{\frac{E-E_f}{kT}} + 1} \dots\dots\dots (2)$$

where  $k$  is the Boltzmann constant and  $T$  the absolute temperature. Semiconductors are classified as n-type or p-type depending on whether electrons or holes are the majority carriers. Fermi energy is also defined as the energy where probability of carrier occupancy is 50%. The product  $kT$  gives thermal energy and its value is 0.026 eV at room temperature. Addition of P to Si shifts Fermi level near conduction band, while addition of B to Si shifts the Fermi level near valence band.

The Fermi function represents only the probability of occupancy, hence total states available for carrier occupancy can be found out by using the density of allowed states. The density of states is zero in the forbidden gap while it is non zero in the allowed energy bands. Density of states can be calculated by solving the time-independent Schrödinger equation. The density of states at energy  $E$  near the conduction band edge is given by [12],

$$g_c(E) = \frac{m_n^* \sqrt{2m_n^* (E - E_c)}}{\pi^2 \hbar^3} \text{cm}^{-3} \text{eV}^{-1} \dots\dots\dots (3)$$

Similarly density of states at energy  $E$  near the valence band edge is given by [12],

$$g_v(E) = \frac{m_p^* \sqrt{2m_p^* (E_v - E)}}{\pi^2 \hbar^3} \text{cm}^{-3} \text{eV}^{-1} \dots\dots\dots (4)$$

Where

$m_n^*$  is effective mass of electron;

$m_p^*$  is effective mass of hole;

$E_c$  is conduction band minima;

$E_v$  is valence band maxima.

The carrier concentration at any energy level can be expressed as the product of probability of occupancy and the number of available states. Therefore electron concentration in the conduction band can be expressed as [11]:

$$n_o = \int_{E_c}^{\infty} g_c(E) f(E) dE \dots\dots\dots (5)$$

Solving the integral, we get,

$$n_o = N_c e^{(E_f - E_c) / kT} \dots\dots\dots (6)$$

Where

$$N_c = 2 \left( \frac{2\pi m_n^* kT}{h^2} \right)^{3/2} \dots\dots\dots (7)$$

$N_c$  is a constant at fixed temperature, known as effective density of states in the conduction band

Similarly,

$$N_v = 2 \left( \frac{2\pi m_p^* kT}{h^2} \right)^{3/2} \dots\dots\dots (8)$$

$N_v$  is a constant at fixed temperature, known as effective density of states in the valence band.

### 1.4.1. Homojunction

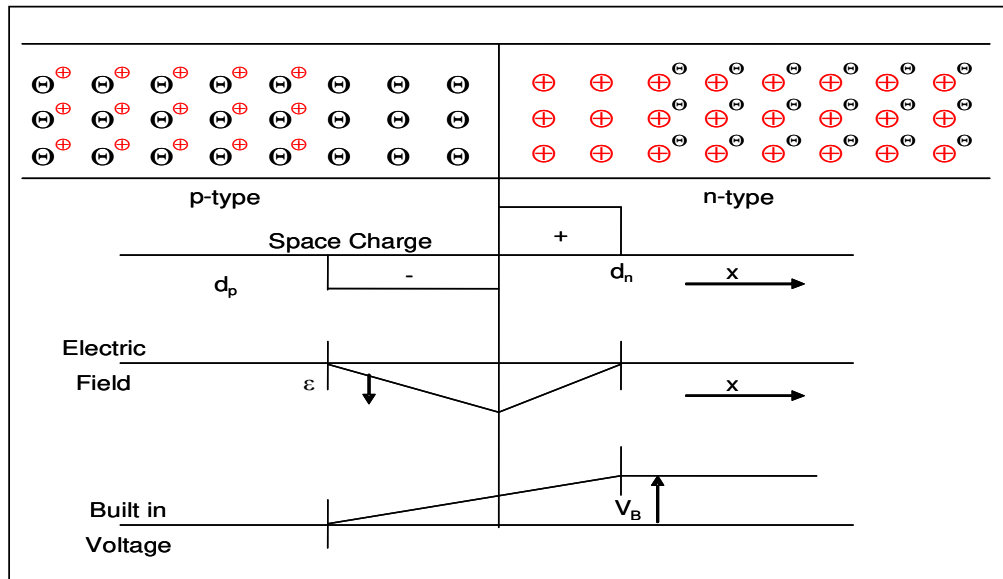


Figure 4 : Homojunction in a semiconductor

When a p-type semiconductor is joined to a n-type semiconductor, holes from the p-region tend to diffuse to the n-region and electrons from the n-region tend to diffuse to the p-region because of the concentration gradients. Recombination of diffusing free carriers with the oppositely charged majority carriers creates a region depleted of free carriers. The dopant ions in the depletion regions are no more compensated. This gives rise to a barrier or built-in electric field which opposes further diffusion of free carriers. Electron-hole pairs generated within a diffusion length of the p-n junction region are separated by the built-in field at the junction. Under equilibrium, the magnitude of the field balances the tendency of electrons to drift from the n-type region into the p-type region to the tendency of electrons to drift in the opposite direction under the influence of the built-in field. The Fermi level is constant throughout the entire system.

At equilibrium electrons and holes currents are zero. Under this condition the electric field (E) generated by diffusion of charge carriers is given by the following relation [11]:

$$E = -\frac{kT}{qn} \frac{dn}{dx} \dots\dots\dots(9)$$

Where

k is the Boltzmann constant;

T is the temperature in Kelvin;

q is the charge of an electron;

n is free electron concentration in equilibrium;

dn/dx is change in electron concentration.

The built-in potential is an integral of the electric field from p-region to n-region and is given as [11]:

$$V_B = \frac{kT}{q} \ln \frac{N_A N_D}{n_i^2} \dots\dots\dots(10)$$

Where

$N_A$  is acceptor concentration;

$N_D$  is donor concentration;

$n_i$  is intrinsic carrier concentration.

The width of depletion region is determined by impurity concentration, built-in voltage and applied voltage. At equilibrium, the depletion width depends only on the built-in voltage.

Total depletion width is given by the relation [11]:

$$x = x_n + x_p = \sqrt{\frac{2\epsilon_s V_B (N_A + N_D)}{q(N_A N_D)}} \dots\dots\dots (11)$$

Where

$x_n$  is depletion width on n-type material;

$x_p$  is depletion width on p-type material

$\epsilon_s$  is permittivity of the material.

Under non-equilibrium conditions, the Voltage applied  $V_a$  is taken into account as [11]:

$$x = \sqrt{\frac{2\epsilon_s (V_B - V_a)(N_A + N_D)}{q(N_A N_D)}} \dots\dots\dots (12)$$

The depletion width increases under reverse bias ( $-V_a$ ) while it decreases under forward biased condition ( $+V_a$ ).

### 1.4.2. Heterojunction

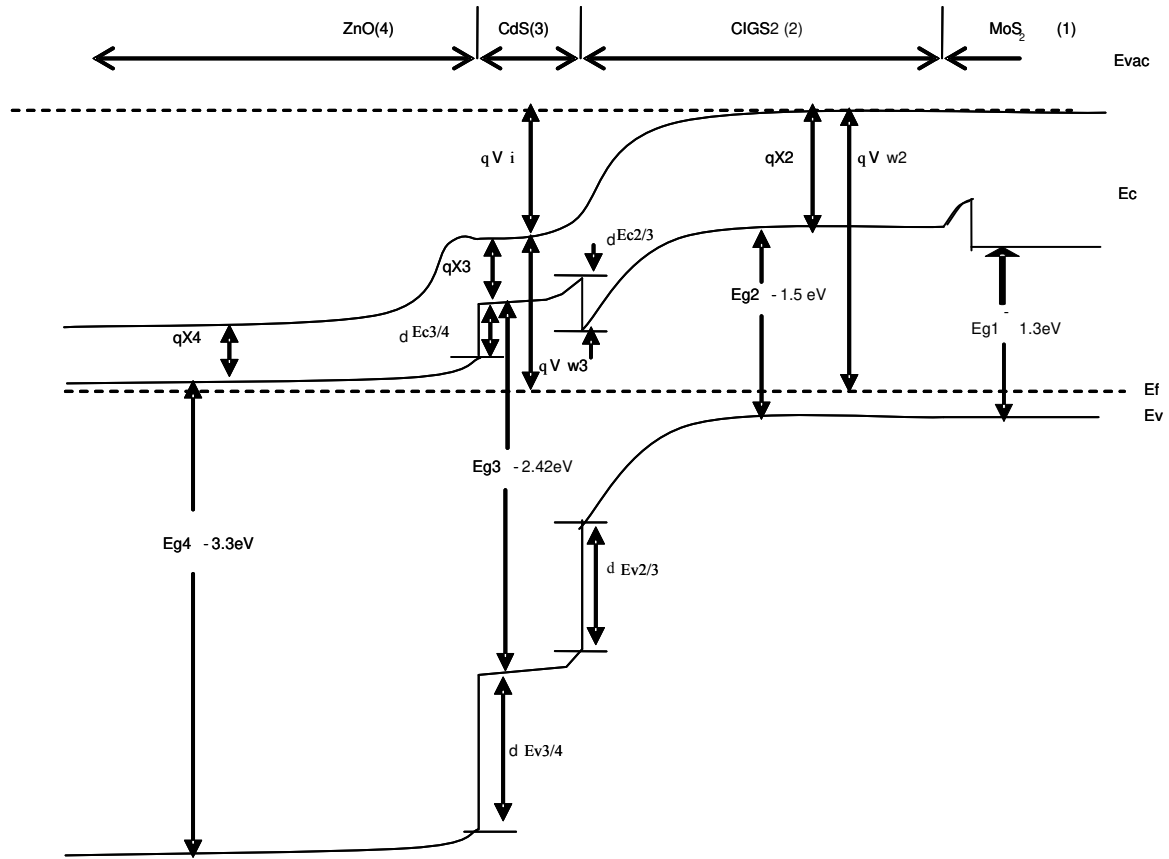


Figure 5 : Semiconductor heterojunction

Where,

The numbers 1, 2, 3 and 4 refer to MoS<sub>2</sub>, CIGS<sub>2</sub>, CdS and ZnO respectively.

Eg<sub>1</sub>, Eg<sub>2</sub>, Eg<sub>3</sub> and Eg<sub>4</sub> – Bandgaps

qX<sub>2</sub>, qX<sub>3</sub> and qX<sub>4</sub> – electron affinities

qVw<sub>2</sub>, qVw<sub>3</sub> – work functions

qV<sub>i</sub> – Built-in potential at p-n junction

dEc<sub>2/3</sub> – Conduction band offset between CIGS<sub>2</sub> and CdS

dEv<sub>2/3</sub> – Valence band offset between CIGS<sub>2</sub> and CdS

$dE_{c3/4}$  – Conduction band offset between CdS and ZnO

$dE_{v3/4}$  –Valence band offset between CdS and ZnO

Heterojunction involves some additional features in the band diagram as compared to a homojunction. To form a heterojunction, two semiconductors of different bandgaps are grown together such as p-type CIGS2 and n-type CdS as shown in the Figure 5. In the case of a heterojunction system, the electron affinities of the individual semiconductors are also different due to the difference in the work functions. For maintaining the vacuum level, a discontinuity has to occur in the conduction band as well as valence band at the interface. The discontinuity in the conduction band at the interface can be written as [11]:

$$dE_{c2/3} = X_2 - X_3$$

The discontinuities at the interface affect the near-by space-charge regions. In the quasi-neutral region, the separation between the conduction band edge and the Fermi level is determined by doping in that material [11]:

$$E_{c3} - E_f = kT \ln \left( \frac{N_{c3}}{N_{D3}} \right) \dots\dots\dots (13)$$

Where,  $N_{c3}$  – density of state in conduction band of CdS,  $N_{D3}$  – donor dopant density.

$$E_{c2} - E_f = E_{g2} - (E_f - E_{v2}) = E_{g2} - kT \ln \left( \frac{N_{v2}}{N_{a2}} \right) \dots\dots\dots (14)$$

Where,  $N_{v2}$ - density of states in valence band of CIGS,  $N_{a2}$ - acceptor dopant density

The total difference in the conduction band edge between the neutral regions in the two semiconductors is given by [11]:

$$E_{c2} - E_{c3} = E_{g2} - kT \ln\left(\frac{N_{c3}N_{v2}}{N_{d3}N_{a2}}\right) \dots\dots\dots (15)$$

It can be seen that it does not depend on the electron affinities.

The role of the spike as a barrier to the electron flow from n-type to p-type depends on the built-in potential drop on each side. If concentration of holes in p-type material is lower as compared to that of electrons in the n-type material, the majority of band bending occurs in the p-type material side and the top of the spike is lower than the conduction band edge in the neutral region of the p-type material. The barrier to the flow of electrons from n-type to p-type is the difference in the conduction band edges in the neutral region of the two materials. However, if the doping is other way round, then the majority of band bending occurs in the n-type material and the top of spike can be higher than the conduction band edge in the neutral region of the p-type material. Here the barrier to electron flow from n to p type is higher.

### **1.5. Current-voltage characteristics**

A solar cell is nothing but a p-n junction diode under no illumination. Under forward bias, excess electrons flow in the p region while excess holes flow in the n region. The potential barrier across the junction reduces. Under reverse bias, the situation is exactly opposite and the potential barrier across the junction increases. There is an exponentially increasing relation between the minority carrier concentration and the applied voltage. The relationship is valid at the depletion layer boundaries [11].



$$n_p = n_{po} e^{qV_a/kT} \dots\dots\dots (16)$$

$$p_n = p_{no} e^{qV_a/kT} \dots\dots\dots (17)$$

Where

$n_p$  is the injected minority carrier concentration in p region;

$n_{po}$  is the minority carrier concentration at the depletion region boundary under thermal equilibrium;

$p_n$  is the injected minority carrier concentration in n region;

$p_{no}$  is the injected minority carrier concentration the depletion region boundary under thermal equilibrium.

The excess minority carrier concentration decreases exponentially away from the junction. The decay depends on the diffusion constant and the carrier lifetime [11].

$$\hat{n} = \hat{n}_o e^{-x/\sqrt{D_n\tau_n}} \dots\dots\dots (18)$$

$$\hat{p} = \hat{p}_o e^{-x/\sqrt{D_p\tau_p}} \dots\dots\dots (19)$$

Where

$D_n$  and  $D_p$  are the diffusion constants of electron and hole minority carriers;

$\tau_n$  and  $\tau_p$  are the lifetime of electron and hole minority carriers;

$\hat{n}$  is the injected electron carrier concentration in p-region;

$\hat{n}_o$  is the injected electron carrier concentration at depletion width edge;

$\hat{p}$  is the injected hole carrier concentration in n-region;

$\hat{p}_o$  is the injected hole carrier concentration at depletion width edge

The total current is the sum of hole and electron currents [11]:

$$I = I_p + I_n = qA \left( \sqrt{\frac{D_p}{\tau_p}} \hat{p}_o + \sqrt{\frac{D_n}{\tau_n}} \hat{n}_o \right) \dots\dots\dots (20)$$

Where, A is the junction area

It is known that  $n_p = n_{po} + \hat{n}_o$  and also  $p_n = p_{no} + \hat{p}_o$

$$n_{po} = n_i^2 / N_A \dots\dots\dots (21)$$

$$p_{no} = n_i^2 / N_D \dots\dots\dots (22)$$

Where

$n_i$  is the intrinsic carrier concentration

Therefore,

$$\hat{n}_o = n_{po} \left( e^{qV_a / kT} - 1 \right) \approx \frac{n_i^2}{N_A} \left( e^{qV_a / kT} - 1 \right) \dots\dots\dots (23)$$

$$\hat{p}_o = p_{no} \left( e^{qV_a / kT} - 1 \right) \approx \frac{n_i^2}{N_D} \left( e^{qV_a / kT} - 1 \right) \dots\dots\dots (24)$$

Hence, the total current can be written as [11],

$$I = qAn_i^2 \left( \sqrt{\frac{D_p}{\tau_p N_D}} + \sqrt{\frac{D_n}{\tau_n N_A}} \right) (e^{qV_a / kT} - 1) \dots\dots\dots (25)$$

Under reverse biased condition, reverse saturation current is [1]:

$$I_o = -qAn_i^2 \left( \sqrt{\frac{D_p}{\tau_p N_D}} + \sqrt{\frac{D_n}{\tau_n N_A}} \right) \dots\dots\dots (26)$$

From equations 25 and 26,

$$I = I_o (e^{qV_a / kT} - 1) \dots\dots\dots (27)$$

Under illumination, the photo generated current has to be taken into account;

Therefore equation 27 becomes [1]:

$$I = I_o (e^{qV_a / kT} - 1) - I_L \dots\dots\dots (28)$$

Where,

$I_L$  is photogenerated current.

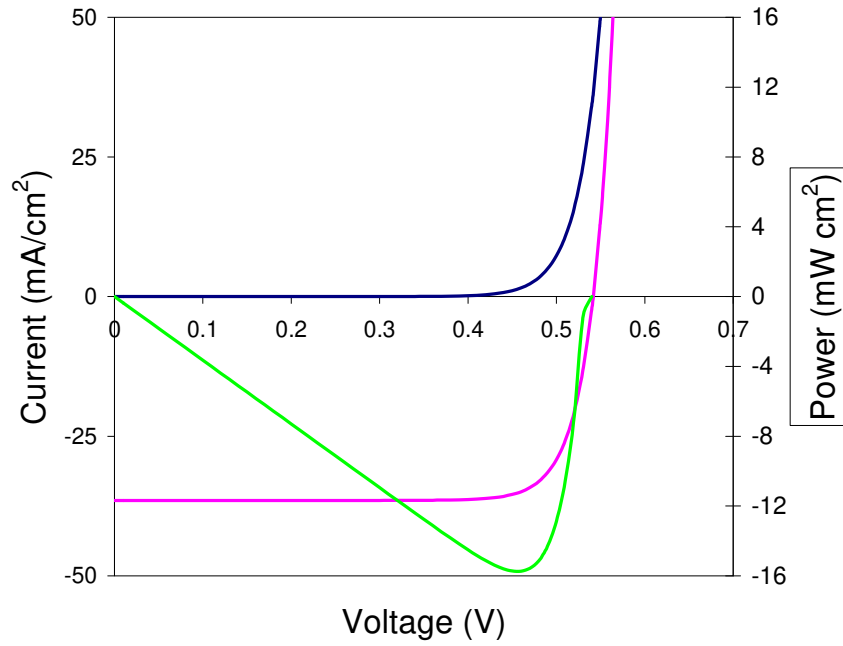


Figure 6 : I -V characteristic of solar cell in dark and under illumination drawn in forth quadrant

When a cell is not connected to an external circuit and light is shone upon it, the generated free charge carriers flow across the built-in electric field and build up charge on the other side of the cell till it just balances the built-in field. The corresponding built up potential is called open circuit voltage ( $V_{oc}$ ) and it is the maximum voltage a cell can provide. It is given by the relation [12]:

$$V_{oc} = \frac{kT}{q} \ln\left(\frac{I_L}{I_o} + 1\right) \approx \frac{kT}{q} \ln \frac{I_L}{I_o} \dots\dots\dots (29)$$

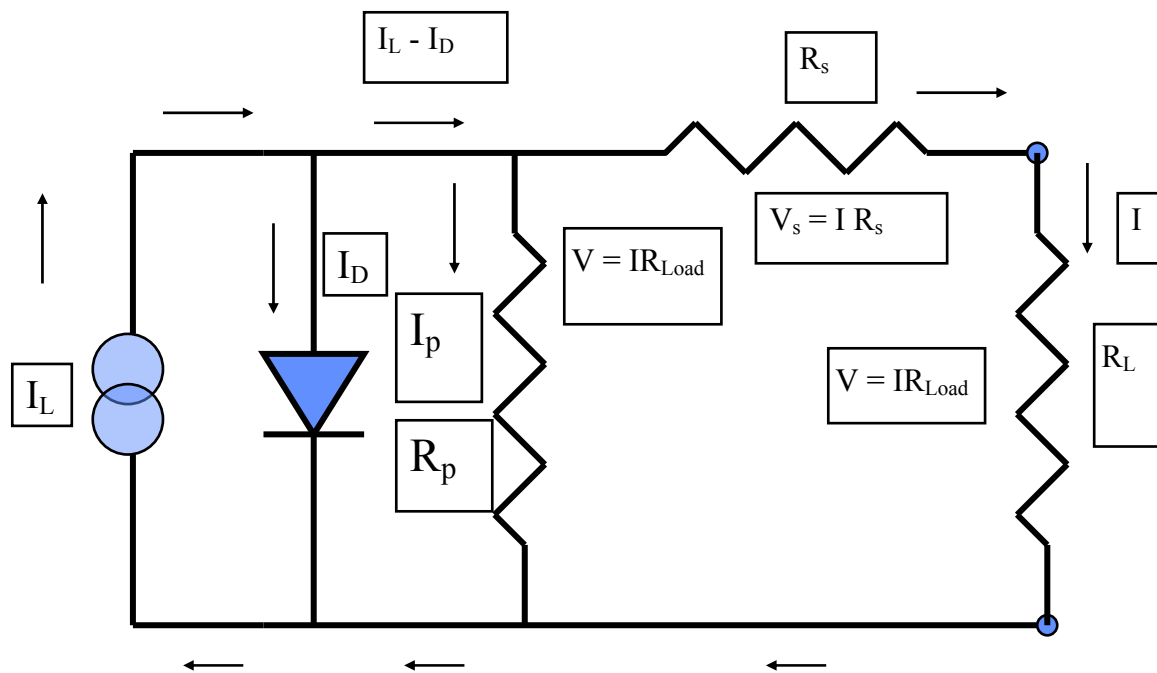


Figure 7 : Equivalent circuit of a solar cell

Equivalent circuit of a solar cell is shown in Figure 7 where  $I_L$  is light generated current,  $I_D$  is diode current,  $I_p$  is current through parallel resistance and  $I = I_L - I_D - I_p$ . Excitation of excess carriers due to illumination results in flow of photogenerated current. The photogenerated current is represented by a constant current source  $J_L$  in parallel with the junction. Effect of series resistance,  $R_s$  and shunt resistance,  $R_p$  on the I-V curve is shown in Figure 8. An increase in the series resistance does not affect the open circuit voltage,  $V_{oc}$  while the short circuit current,  $J_{sc}$  can be reduced with significant increase in the series resistance. Similarly, a reduction of shunt resistance does not affect short circuit current density, while significant reduction in the shunt resistance affects the open circuit voltage considerably.

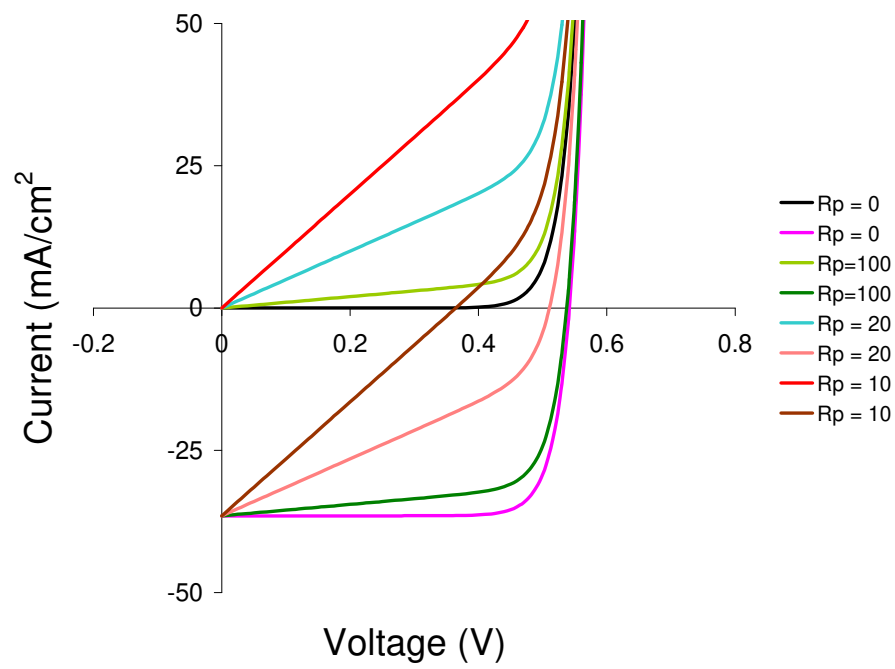
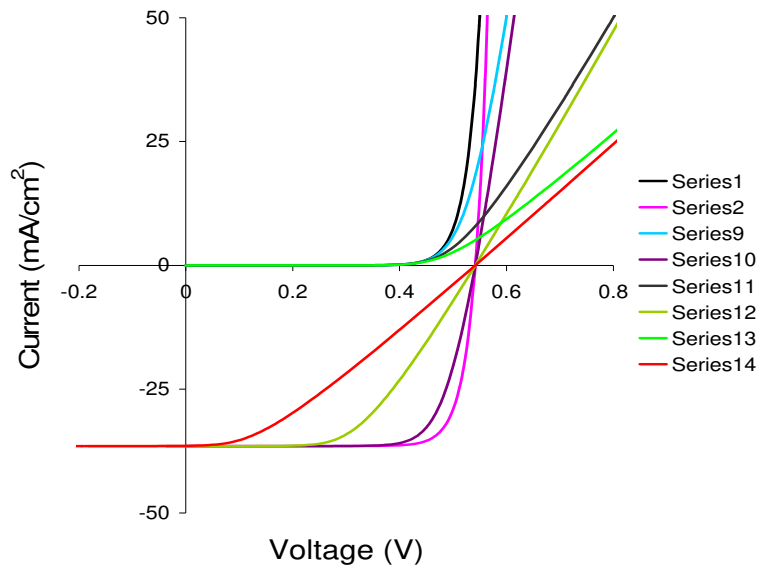


Figure 8 : Effect of series and shunt resistance on current-voltage curve

Under open circuit voltage and short circuit current conditions, the power is zero. The maximum power is the product of optimum values of voltage and current. Fill Factor (FF) is another important factor in efficiency measurement of solar cell. The Fill-Factor is defined as the ratio of peak power to the product of open circuit voltage and  $J_{sc}$ . FF describes how closely the current-voltage curve resembles the rectangle  $V_{oc}I_{sc}$ .

$$FF = \frac{V_{m_p} I_{mp}}{V_{oc} I_{sc}} \dots\dots\dots (30)$$

Where,

$V_m$  and  $I_m$  are the optimum voltage and optimum current at the maximum power point.

The photovoltaic conversion efficiency of a solar cell is given by the relation [12]:

$$\eta = \frac{V_{oc} I_{sc} FF}{P_{in}} \dots\dots\dots (31)$$

The photovoltaic conversion efficiency depends on short circuit current density ( $J_{sc}$ ), open circuit voltage ( $V_{oc}$ ) and fill factor (FF). These factors in turn depend on the material quality and how effectively the light gets absorbed in the material. The ability of a semiconductor to absorb sunlight effectively is denoted as absorption co-efficient ( $\alpha$ ). A direct bandgap semiconductor such as copper-indium-gallium sulfide requires less thickness to absorb same amount of light as compared to an indirect bandgap semiconductor such as silicon. Low wavelength photons are usually absorbed within the built-in electric field while the high wavelength photons are absorbed away from the built-in electric field. The time during which the carriers remain active is called their lifetime. If during this lifetime, the carriers diffuse to the depletion region and thus come under the influence of a built-in electric field, they will be

propelled over to other regions and produce a current. The average distance a charge carrier travels towards the built-in field before recombination is termed as diffusion length, which is the product of diffusion coefficient and life-time of a carrier. Defects such as vacancies and grain boundary can affect the diffusion coefficient and carrier life-time. The Open circuit voltage depends on the built-in voltage of the device. The open circuit voltage can be reduced due to recombination centers which act as shunting paths. For a highly efficient cell, the shunt resistance should be infinity. Series resistance losses take place due to junction contact resistances between the layers of the cell. For an efficient cell, series resistance should be near zero. Current-voltage (I-V) and quantum efficiency (QE) measurements are used for the measurement of the photovoltaic parameters. Quantum efficiency denotes the effectiveness of a cell to convert photons of various wavelengths. If a cell shows very good response to low wavelength photons and poor response to high wavelength photons, it indicates that the charge carriers generated within the built-in electric field are effectively absorbed while the charge carriers generated away from the field in the bulk undergo recombination.

### **1.6. Motivation and definition of scientific problem**

The objective of the present work has been decided carefully after considering holistically all the metrics of the technology development of solar cells with respect to CIGS<sub>2</sub>. Apart from achieving higher efficiency, other metrics by which prospects of the technology are measured are: cost, ease of fabrication, throughput, reliability etc [13]. These parameters are also endorsed in the ‘Solar America Initiative’ proposal by the US Government. It will be interesting to study whether an approach can be developed such that while achieving higher efficiencies, a balance in ease of fabrication and costs involved can be still feasible. The knowledge gained by



this development will be useful for the photovoltaic community in developing the technology of large scale manufacture.  $\text{CuIn}_{1-x}\text{Ga}_x\text{S}_2$  (CIGS2) thin films having chalcopyrite structure are being considered for use in high-efficiency photovoltaic cells. CIGS2 thin-film solar cells are of interest for space power applications because of near optimum bandgap for AM0 solar radiation outside the earth's atmosphere [14-17]. Copper indium sulfide modules are being manufactured by Sulfurcell in Germany. At FSEC PV Materials Laboratory, the record efficiency of 11.99% has been achieved on a 2.7  $\mu\text{m}$  CIGS2 thin film prepared by sulfurization [18]. CIGS2 thin films grown by sulfurization have been grown with copper-rich compositions, and excess cuprous sulfide is etched afterwards. In Cu-rich CIGS2, we get near stoichiometric composition after etching, corresponding to composition range of  $10^{17}$ - $10^{19}/\text{cm}^3$ . However, the desirable carrier concentration range should be typically around  $10^{16}$ - $10^{17}/\text{cm}^3$  [19]. This range can be achieved if we start with a copper-deficient composition. Also the etching step can be removed, thus making the fabrication a lot easier and less toxic. The question is if copper-deficient thin film CIGS2 solar cells can be fabricated in a higher efficiency range? Cuprous sulfide acts as a flux in Cu-rich CIGS2 films and helps the formation of alpha phase. It is difficult to produce device quality films in copper-deficient compositions because cuprous sulfide is unavailable. The CIGS2 phase may decompose into two or more phases due to narrowing of the phase diagram. Possible solution is to find some mechanism during the copper-deficient CIGS2 growth process which may make the CIGS2 phase formation stable.

There are several reports showing the effect of sodium addition on  $\text{CuIn}_{1-x}\text{Ga}_x\text{Se}_2$  absorbers [20-27]. Rudamann et al have studied CIGSe solar cells with sodium incorporated into the absorber layer showing high efficiency [20, 21]. The most common observations defining role of sodium in CIGSe as per literature are:

- Sodium acts as a fluxing agent, widens the alpha phase in the phase diagram and macro-defect formation is reduced by the presence of sodium
- Sodium enhances the grain structure and morphology of the absorber
- Sodium increases the p-type conductivity of the absorber

Most of the observations have been found to occur simultaneously after addition of sodium.

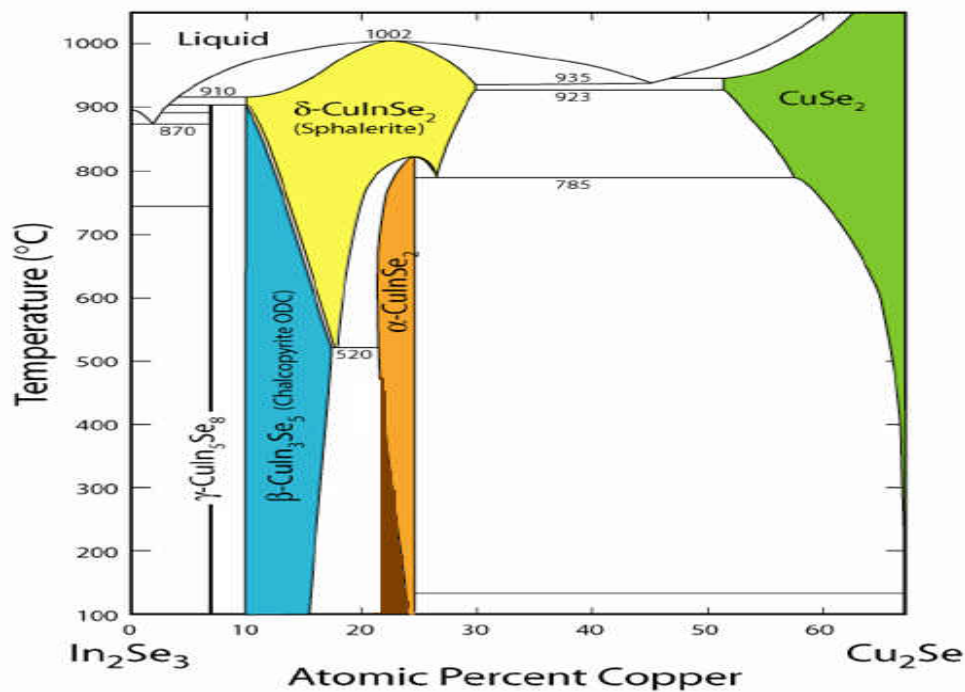


Figure 9 : Alpha phase widening due to sodium addition in CIGSeS

Figure 9 shows the role of sodium and gallium in widening the alpha phase and thus contributing towards stable phase formation. It may be noted that sodium acts generally on the copper-deficient side and gallium towards copper-rich side of the boundaries of the alpha phase.

According to the study by Braunger et al, sodium polyselenide ( $\text{Na}_2\text{Se}_x$ ) forms as a first reaction step in the CIGSe formation in the presence of sodium due to its lowest free energy [25].

$\text{Na}_2\text{Se}_x$  segregates along the grain boundaries of CIGSe and acts as a source for selenium.  $\text{Na}_2\text{Se}_x$  influences the reaction rate of formation of CIGSe and provides opportunity for grains to grow larger.

According to models in literature [26], increase in p-type conductivity can be due to elimination of the compensating antisite donor defect  $V_s$ ,  $\text{In}_{\text{Cu}}$  as well as it can be due to direct creation of acceptors such as antisite defect  $\text{Na}_{\text{In}}$ . An increase in open circuit voltage is a consequence of higher effective acceptor concentration. However, if Na concentration increases to a level that most of the InCu defects have already been eliminated, it will start to remove the acceptor  $V_{\text{Cu}}$ , thereby, reducing the hole density. Therefore, excessive amount of sodium is detrimental to the performance of solar cells after optimum level is reached.

Nakada et al [27] have shown that the net carrier concentration increased even for copper-deficient compositions below 0.7. This implies that high efficiency solar cells can be produced without precisely controlling the film composition, which may lead to a low-cost manufacturing.

It will be interesting to check if sodium can play a role in copper-deficient CIGS2 and if any model explained for CIGSe can explain the behavior of sodium in copper-deficient sulfides.  $\text{CuInS}_2$  films have already shown better device properties and increased p-type conductivity [28, 29]. It will be interesting to verify if sodium can play a role in Copper-deficient CIGS2 absorbers also. It has been found in the earlier studies (Luck et al) that sodium doesn't enhance or deteriorate the photovoltaic properties in copper-rich  $\text{CuInS}_2$  because  $\text{Cu}_2\text{S}$  is already available. [30]. Yamamoto et al report an increase in net hole concentration in copper deficient  $\text{CuInS}_2$  due to addition of sodium as a consequence of a decrease in the concentration of donors ( $V_s$ ,  $\text{In}_{\text{Cu}}$  and

In<sub>i</sub> sites.)[29]. None of the earlier contributions report formation of device quality films with acceptable efficiencies for CuInS<sub>2</sub> or CIGS<sub>2</sub>.

Large grain size that is desirable for obtaining high efficiency cells can be achieved by creating conditions of fewer nucleation sites and large mobilities of the deposited species. There are limits to employing very high temperature processing for increasing the mobility because of the softening temperature of the sodalime glass and excessive reaction of sulfur carrying precursors with the molybdenum back contact. Sodium may play a vital role by enhancing the atomic mobility and improving the coalescence even in thinner films; sodium incorporated In copper-rich CIGS<sub>2</sub> precursors, increased mobility and consequently absorber phase formation is obtained due to liquid-like behavior of pseudo-binary Cu<sub>2-x</sub>S phase region. Hence sodium may not play a vital role in copper-rich precursors. Also for the same purpose, copper-rich precursors for this purpose are prepared with excess copper. After sulfurization, the absorber film is etched to remove the excess copper-phase segregated at the surface. This would lead to the stoichiometric Cu/(In+Ga) of unity but not to the desired Cu-poor composition for attaining optimum doping level. This also makes the film rough. Copper-deficient absorber can produce a comparatively smooth film and better morphology. The efficiencies are limited in Copper-deficient sulfides due to extremely low hole concentration as compared to copper-rich sulfides. It is intended to study the morphology and device properties of CIGS<sub>2</sub> thin films with Copper-deficient absorbers after minute amounts of sodium are introduced on the Mo-coated substrate in the form of sodium fluoride layer prior to sputter deposition of copper-gallium alloy and, indium. The beneficial effects of sodium incorporation might improve film morphology, reduce defects and increase carrier concentration. Since the absorbers are prepared in Cu-deficient conditions,

the thickness of the absorber will automatically reduce thus satisfying the purpose of lower material consumption.

Currently the thickness of the absorber for the highest efficiency cell by sulfurization is 2.7  $\mu\text{m}$ . Recent research endeavors in the CIGS2 thin film photovoltaic community are directed towards thinner films because the availability and cost of indium as well as gallium are limiting factors [31]. The required amounts of expensive metals can be lowered by using thinner films. Since it will take less time to deposit precursors for producing reduced thickness of absorbers, it will also increase the throughput. Initially, small sized grains are formed during the film growth [32]. With continuing growth to larger thicknesses, more favorably oriented grains grow faster at the expense of others and coalesce to form compactly packed large-grain morphology. Hence certain minimum thickness of a thin film is essential for the grains to coalesce and grow. The solar cell performance in smaller grained chalcopyrite absorber deteriorates due to detrimental effects of the larger fraction of grain boundaries [33]. It is essential to hasten the grain growth through coalescence to obtain high- efficiency device properties even in thinner films. It will also be interesting to explore the changes in morphology when cu-rich absorbers are made thinner and also the mechanisms by which better performance can be achieved in these absorbers.

## 2. MATERIALS REVIEW

### 2.1 CIGS2 thin film solar cells

CIGS2 has a near ideal direct bandgap to absorb the most of the visible solar spectrum, also it has high absorption coefficient. Highest efficiency is 12.3% by co-evaporation and 11.99% by sulfurization [18], while module level efficiencies are in the range of 8-9%. Being a wide band gap material, CIGS2 has following advantages [34]:

- Near optimum bandgap
- Better temperature coefficient, thus perform well under real-world operating conditions
- Better suitable for space applications since the degradation of open-circuit voltage due to radiation is less critical in devices with high open-circuit voltages
- Can be used in tandem solar cells with other materials to embrace combinations of bandgaps

A wide variety of methods are available for manufacturing CIGS2 thin films. Some of the methods are spray-pyrolysis [35], electrochemical deposition [36, 37], physical vapor deposition (PVD) techniques, sulfurization of sputtered metallic precursors (Cu-In-Ga) in H<sub>2</sub>S ambient [38-47] and evaporation/co-evaporation [48-54]. Device quality CIGS2 absorbers have been grown mostly with the cu-rich composition. Each method has its advantages and disadvantages [55]. An important advantage of sputter deposition is that even the highest melting point materials are easily sputtered. Sputter deposited films have a composition close to that of the source material. Sputtered films typically have a better adhesion on the substrate than evaporated films. Sputtering process is scalable. The defect structure of these films is very complex due to a

number of elements involved in its formation. The phase diagrams have been studied by Godecke et al. [56].

## 2.2 Optical properties

CIGS2 is a material ideal for solar cells due to its direct band gap and high absorption coefficient. Due to its direct band gap CIGS2 absorbs light much more efficiently, and requires small amount of material. On the contrary, silicon is an indirect band gap material and requires more material for light absorption. The optical absorption coefficient is a function of energy of incident photons.

$$I(h\nu, x) = I_0(h\nu, x) e^{-\alpha(h\nu)x} \dots\dots\dots 2.1$$

The typical absorption coefficient,  $\alpha(h\nu)$  of CuInS<sub>2</sub> is  $\sim 10^5$  / cm for a photon energy of  $h\nu = E_g + 0.2$  eV, where  $E_g$  is the bandgap energy of the respective material [6]. The wavelength dependence of the absorption coefficient (Figure 10) implies that all high-energy photons will be absorbed in CIGS2 very close to the surface, while photons with energies only slightly larger than the band gap of the absorber will penetrate more deeply into the CIGS2.

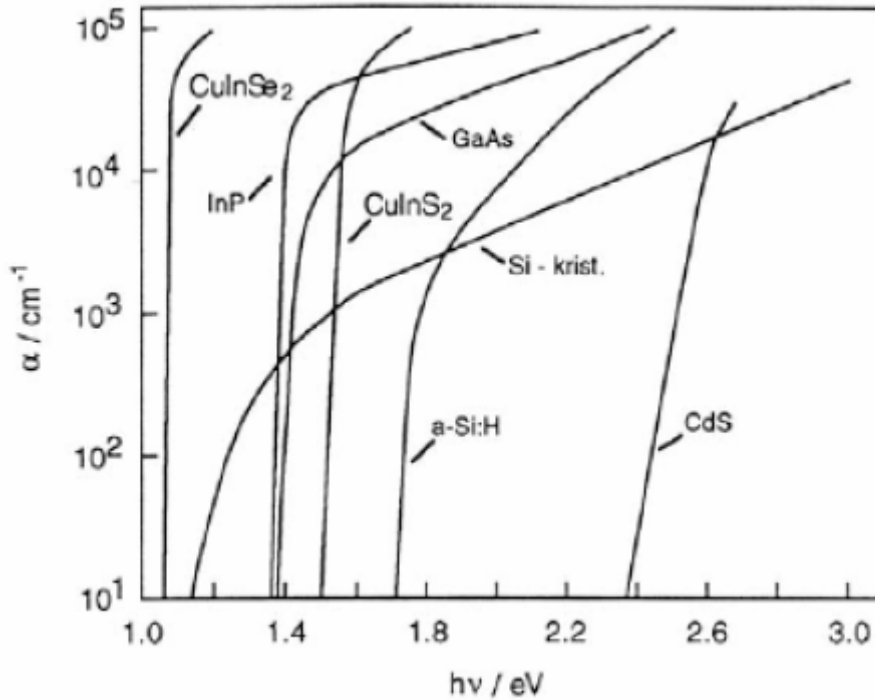


Figure 10 : Dependence of the absorption coefficient on the photon energy for selected semiconductors [6].

### 2.3 Crystal Structure

The lattice structure of Copper-Indium-disulfide ( $\text{CuInS}_2$ ) is tetragonal and the lattice parameters  $a$  and  $c$  are 5.523 and 11.141 Å, respectively. Sulfur is tetrahedrally coordinated to two indium atoms and two copper atoms. Also each copper atom and indium atom is tetrahedrally coordinated to four Sulfur atoms. Although  $\text{CuInS}_2$  has a tetragonal structure, it is very similar to a stack of two face centered cubic structures, where  $c \sim 2a$  [57]. (111) is the close packed plane for face centered cubic structures.  $\text{CuInS}_2$  also grows in the close packed plane, which in this case is the (112) plane analogous to (111) plane of a FCC structure. Figure 10 shows a schematic tetragonal  $\text{CuInS}_2$  structure.  $\text{CuInS}_2$  has a direct band gap (1.55eV); hence it



has very good potential for solar energy conversion. The consequences are lower minority carrier diffusion length and higher absorption coefficient.

$\text{CuGaS}_2$  has a structure similar to that of  $\text{CuInS}_2$ ; and has a band gap of 2.42 eV. Gallium is in the same group of indium in the periodic table. Thus, by substituting gallium for indium in some places in the lattice, the band gap of  $\text{CuIn}_{1-x}\text{Ga}_x\text{S}_2$  (CIGS2) can be varied from  $1.55 \text{ eV} < E_g < 2.42 \text{ eV}$  [58]. Addition of gallium can be considered as alloying between the ternary compounds  $\text{CuInS}_2$  and  $\text{CuGaS}_2$ . Material properties can be optimized due to gallium incorporation and its addition also changes other properties and characteristics such as defect chemistry, defect levels within the gap, electron and hole affinities, carrier concentration, resistivity, crystal structure and lattice constants.

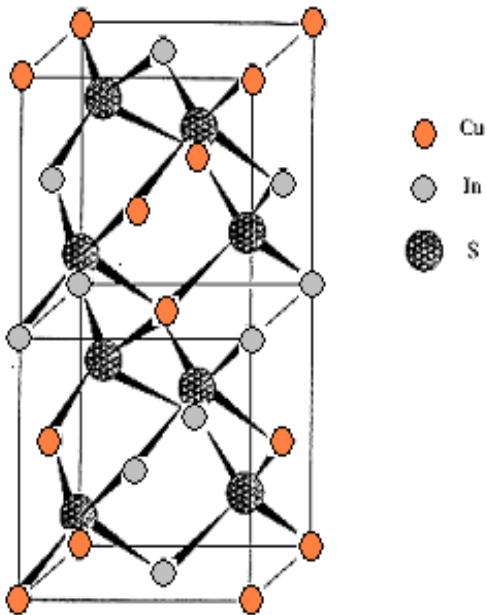


Figure 11 : Schematic diagram of the crystal structure of  $\text{CuInS}_2$

The overall electrical properties of CIGS2 films depend upon stoichiometry and compositional uniformity, which are in turn related to the film growth parameters. It becomes essential to grow large grain films with the appropriate composition ratio of Cu/(In+Ga) below 1. A wide variety of techniques have been explored to grow CIGS2 thin films for photovoltaic applications. Most of the improvement in cell performance has been achieved by skillful empirical optimization based on intuition, at times aided by phenomenological models of cell design, and absorber preparation. The bandgap of  $\text{CuIn}_{1-x}\text{Ga}_x\text{Se}_2$  (CIGS) and  $\text{CuIn}_{1-x}\text{Ga}_x\text{S}_2$  (CIGS2) can be increased respectively over the ranges 1.0-1.73 eV and 1.5-2.4 eV by incorporation of gallium. Schock and coworkers [59] have found that the open-circuit voltage of chalcopyrites for thin film PV cells does not increase proportionately with increase in the bandgap. The open-circuit voltage increases in a superlinear fashion up to gallium content, x of 0.3 while it is sublinear at higher Ga content, leading to considerable deterioration.

## **2.4 Phase diagram**

Figure 12 shows an equivalent ternary phase diagram comprising Cu-In-S compounds that have been identified along the tie line of  $\text{Cu}_2\text{S} - \text{In}_2\text{S}_3$  [60]. A simple pseudobinary phase diagram can be deduced from this ternary diagram along the tie line between  $\text{Cu}_2\text{S}-\text{In}_2\text{S}_3$  (central line in Figure 12). The bold points along this line indicate photovoltaic quality material.  $\text{CuInS}_2$  can be formed by combining these two compounds:



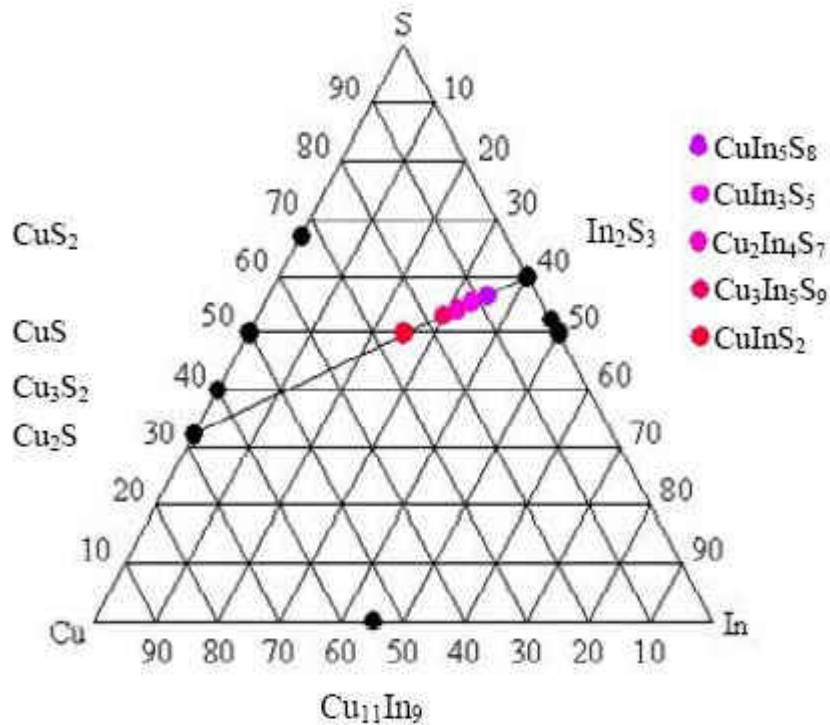


Figure 12 : Ternary component diagram of Cu-In-S [60].

Figure 13 shows the pseudobinary phase diagram. Four different phases have been found relevant in this range:  $\alpha$  – phase (CuInS<sub>2</sub>),  $\beta$  – phase (CuIn<sub>3</sub>S<sub>5</sub>), the  $\delta$  – phase (high temperature sphalerite phase) and Cu<sub>2-x</sub>S phase. The phases adjacent to  $\alpha$  – phase have similar structure. The  $\beta$  – phase is a defect chalcopyrite phase built by ordered arrays of defect pairs (copper vacancies and In-Cu antisites). This defect pair is electrically neutral and forms only at the surface. This phase is not a photovoltaic quality material [6].

The range in which  $\alpha$  – phase exists in pure Cu<sub>2</sub>S-In<sub>2</sub>S<sub>3</sub> at room temperature extends from a copper content of 24% to 24.5% on a quasi-binary tie line [60]. This range is quite small and does not include the stoichiometric composition of 25% copper. The copper content is typically 22 and 24 at% for efficient films. At the growth temperature of 450 °C – 550 °C this region ends

up in a single phase  $\text{CuInS}_2$  region. However at room temperature it ends up in the two phase  $\alpha + \beta$  region [60]. Hence  $\text{CuInS}_2$  may separate in two phases after deposition. Addition of gallium considerably widens the single phase  $\text{CuInS}_2$  region at room temperature [60]. Also if  $\text{CuInS}_2$  is grown in copper excess regime, the excess copper forms  $\text{Cu}_{2-x}\text{S}$  quasi-liquid phase at the grain boundaries and on the surface of  $\text{CuInS}_2$  thin film. The  $\text{Cu}_{2-x}\text{S}$  is a phase acts as a flux during the growth of  $\text{CuInS}_2$  thin films. The formation of this copper excess phase slows the growth of  $\text{CuInS}_2$ , and helps in incorporating sulfur into  $\text{CuInS}_2$  lattice.

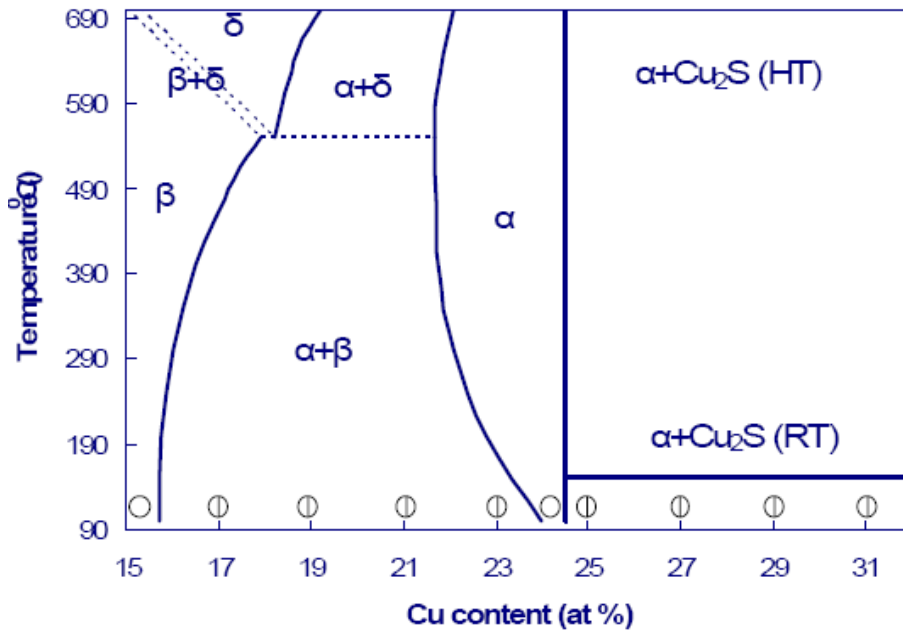
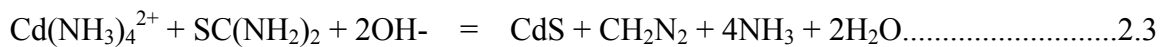


Figure 13 : Pseudo binary phase diagram of  $\text{Cu}_2\text{S}-\text{In}_2\text{S}_3$  [60].

#### **2.4 Heterojunction partner – Cadmium sulfate (CdS)**

$\text{CdS}$  is predominantly used as a heterojunction partner and it has been successfully deposited using various techniques to obtain device quality solar cells [61]. The bandgap of  $\text{CdS}$  is approximately 2.45 eV and it forms an n-type on p-type  $\text{CIGS}_2$ . It is also called as a window

ween 60 to 70°C. As a result, thiourea decomposes releasing S<sub>2</sub>- ions. The complete reaction is



Some of the advantages of CdS layer are:

1. CdS provides a conformal coating on the rough absorber surface.
2. The layer protects from any damages that may occur during further depositions.

**2.5 Transparent conducting oxide window bilayer– intrinsic ZnO and Zinc oxide doped with aluminum (ZnO:Al)**

Intrinsic ZnO (i:ZnO) is a resistive layer. A very thin layer of i:ZnO prevents (ZnO:Al) to come in the direct contact with CIGS<sub>2</sub> absorber or Mo back contact and avoids any shunting

paths. The critical parameter is the thickness of i:ZnO . A smaller value than critical thickness may lead to leakage currents, while a more than critical thickness leads to an increase in the series resistance, thereby reducing the current density. The i-ZnO layer thickness affects the Open circuit voltage [64]. ZnO is an easily available material with low-cost. It has a bandgap of 3.3 eV, which results in transparency to most of the visible spectrum of light. Group III elements can be used as dopants to ZnO and higher conductivity values can be obtained [65]. i:ZnO is generally deposited using RF sputtering , while both RF or DC sputtering techniques can be implemented to deposit ZnO:Al.

### **3. EXPERIMENTAL TECHNIQUE**

The main objective in this research is to prepare thinner, device quality CIGS2 thin films and efficient CIGS2/CdS thin film solar cells and correlate their material and device properties. CIGS2 thin films are prepared by sulfurization of metallic precursors. Initially a stack of elemental layers of copper, gallium, and indium metallic precursors are deposited on molybdenum coated glass substrates using DC magnetron sputtering. Subsequently it is sulfurized at elevated temperatures in the presence of H<sub>2</sub>S gas diluted in nitrogen (4-8% H<sub>2</sub>S). Materials characterization is carried out for CIGS2 thin films for optimizing process parameters. CIGS2/CdS thin film solar cells are completed by the deposition of n-type CdS layer by chemical bath deposition (CBD) followed by transparent conducting bilayer window of intrinsic ZnO (i-ZnO) and doped ZnO:Al by RF magnetron sputtering and Cr/Ag front contact fingers through metal masks by thermal evaporation.

#### **3.1 Substrate preparation**

6 inch x 4 inch size molybdenum coated glass substrates are washed in running tap water. Cotton swabs are used to clean the surface with soap solution. This is followed by a thorough rinsing with tap water and finally washing with deionized (DI) water. The substrate is finally blow-dried using compressed nitrogen gas. Now the substrate is ready for mounting into the DC magnetron sputtering chamber. It is maintained overnight in high vacuum of  $\sim 3 \times 10^{-6}$  Torr prior to the deposition of metallic precursors.

### **3.2. NaF deposition**

Sodium has been deposited in earlier studies on CIGSe using precursors  $\text{Na}_2\text{Se}$ ,  $\text{Na}_2\text{O}$ ,  $\text{NaF}$  and  $\text{Na}_2\text{S}$  [66]. Sodium Fluoride ( $\text{NaF}$ ) is non-hygroscopic, stable in air.  $\text{NaF}$  doesn't have bad odor like  $\text{Na}_2\text{Se}$  and is cheaper. Hence  $\text{NaF}$  was chosen as a precursor for sodium incorporation. This is the very first effort in which effect of sodium on CIGS2 thin films has been studied and an effort has been made to fabricate device quality thin films.  $\text{NaF}$  was deposited by thermal evaporation from a Joule-heated Mo-boat on glass substrates. Subsequently CIGS2 thin films were prepared and cells were completed. Amount of sodium fluoride was systematically increased and trends in device properties were compared with materials properties in order to determine the optimum amount of Na required to fabricate device quality CIGS2 thin films. Four different thicknesses of sodium fluoride ( $\text{NaF}$ ) were chosen: no  $\text{NaF}$ , 40 Å of  $\text{NaF}$ , 80 Å of  $\text{NaF}$  and 120 Å of  $\text{NaF}$  respectively.

### **3.3 Deposition of Copper gallium and indium metallic precursors**

Deposition of copper, gallium and indium metallic precursors is carried out by DC magnetron sputtering. The sputtering system is shown in Figure 14. Two large-area sputtering units have been designed, fabricated and installed earlier at the FSEC PV Materials laboratory. The internal dimensions of vacuum chambers of the two systems are 38.5" x 18.5" x 6" and 26.5" x 18.5" x 6". High vacuum is obtained in the chambers with cryopumps having pumping speeds of 1500 liters/second and 800 liters/second. The deposition parameters for metallic precursors are optimized to obtain an absorber thickness of  $\sim 1.8 \mu\text{m}$  for copper-deficient route and in the range of 1.2-1.5  $\mu\text{m}$  for copper rich route. A precursor film of copper-gallium is sputtered from a copper-gallium alloy target having 22 atomic weight percent of gallium. Indium



metallic precursors were sputtered from indium target. Copper-gallium alloy film is deposited at the power of 350 W and argon pressure of  $1.5 \times 10^{-3}$  Torr while indium is deposited at the power of 230 W and argon pressure of  $7 \times 10^{-4}$  Torr. Linear substrate moving mechanism is used to move the substrates at the requisite speed to achieve desired thickness.

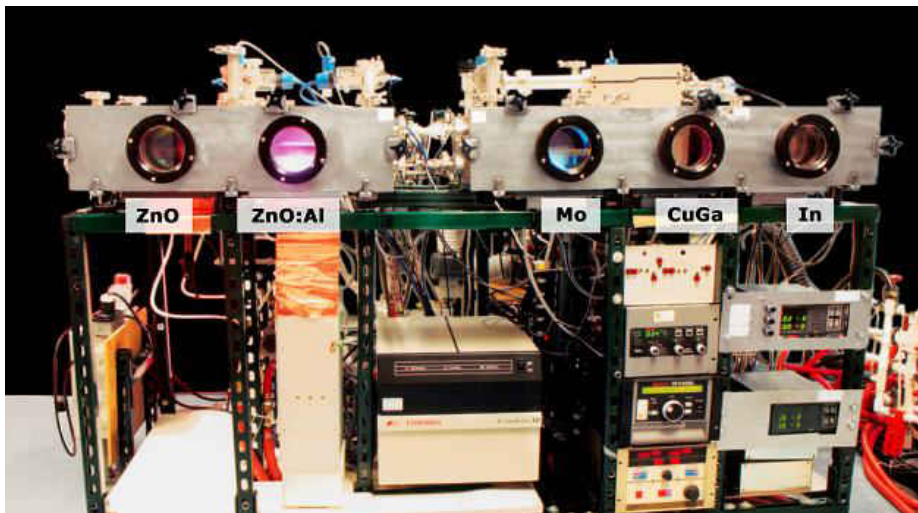


Figure 14 : DC and RF magnetron sputtering units

### **3.4. Sulfurization**

A Lindberg furnace used for sulfurization is shown in Figure 15. The furnace (3" diameter tube, 3 zone, 24" heated length) is a model 55347 with the control console model 58434-P fitted with a quartz tube and gas flow set-up for sulfurization in Nitrogen/H<sub>2</sub>S mixture. 4-8% dilute H<sub>2</sub>S is used for a sulfurization temperature between 450-500 °C. The ramp rates used for the sulfurization process is 50 °C/minute. The excess copper forms a quasi-liquid Cu<sub>2-x</sub>S phase. This phase helps in the kinetics of formation of CIGS<sub>2</sub> phase and enhances the incorporation of sulfur into the CIGS<sub>2</sub> structure by eliminating the sulfur vacancies that act as donor impurity. This phenomenon also promotes the coalescence of grains and thus helps in the

formation of highly crystalline CIGS2. Finally the  $\text{Cu}_{2-x}\text{S}$  phase mostly segregated on top of a stoichiometric CIGS2 layer was removed by etching in 10% KCN for 3 minutes. The sheet resistance of CIGS2 indicates whether the films are Cu-rich or Cu-poor. Generally the sheet resistance values below  $100 \text{ } \Omega/\text{square}$  indicate Cu-rich CIGS2 films and values above  $10 \text{ k}\Omega/\text{square}$  indicate Cu-poor CIGS2 films. Two end pieces of 1 inch x 1 inch are cut from the CIGS2 thin film sample and are used for materials characterization while the central 4 inch x 1 inch piece is used for the completion of the cells. Out of the two end pieces, a few pieces are analyzed without etching and a few are etched before studying their material properties.



Figure 15 : Sulfurization furnace

### **3.5. CdS deposition**

After the CIGS2 layer is completed, next step is the deposition of heterojunction partner layer, CdS. The copper-rich phase is etched in dilute KCN before CdS deposition.

Heterojunction partner layer of CdS is deposited using chemical bath deposition (CBD) technique. Earlier a chemical bath deposition setup has been designed and built for 4 inch x 4 inch size substrates . The chemical bath consists of required amount of distilled deionized water, 0.015M CdSO<sub>4</sub>, ammonium hydroxide (NH<sub>4</sub>OH), and 1.5M (NH<sub>2</sub>)<sub>2</sub>CS. The substrates are kept inside a beaker containing chemical bath. Then, the beaker containing the substrates and the chemical bath is placed inside another larger beaker containing hot water. The temperature of water in the outside bath is controlled carefully to achieve the desired temperature of the CdS deposition in the chemical bath. The ramp rate to achieve maximum temperature depends on the volume of solution in the chemical bath. Figure 16 shows the experimental setup for chemical bath deposition.

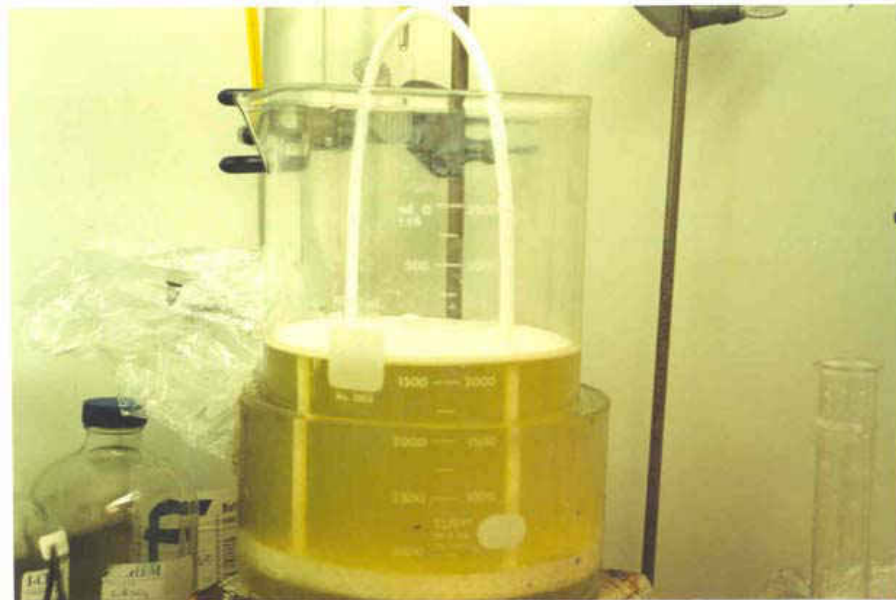


Figure 16 : Set-up for the Chemical Bath Deposition.

### **3.6. Front contact bilayer deposition**

After CdS heterojunction partner is deposited, the sample is again mounted vacuum in the RF magnetron sputtering chamber and is kept overnight in vacuum shown in Figure 14. A bilayer of i-ZnO/ZnO:Al is deposited using RF magnetron sputtering. Linear substrate moving mechanism is used to move the substrates at the requisite speed to achieve desired thickness. The parameters for both the layers have been optimized in the work done earlier and these parameters were used as a starting point for the current work. A thin layer i-ZnO layer is deposited at RF power of 200 W and argon pressure of  $1.5 \times 10^{-3}$  Torr and it is followed by a layer of ZnO:Al at 425 W and argon pressure of  $1.0 \times 10^{-3}$  Torr. The RF power for the ZnO:Al was varied between 300 – 425 W to achieve the required conductivity corresponding to the sheet resistance of the ZnO:Al films of 75-100  $\Omega/\square$  .

### **3.7. Contact Fingers deposition**

CIGS2 thin film solar cells are completed by Cr/Ag contact fingers deposition by thermal evaporation through shadow masks. The thermal evaporation setup is as shown in Figure 17.



Figure 17 : Thermal evaporation setup.

### **3.8. Antireflection coating**

MgF<sub>2</sub> anti-reflection coating is deposited on selected higher efficiency cells. The MgF<sub>2</sub> coating is calibrated and a thickness of ~1000 Å is deposited by thermal evaporation. The final cell structure is as follows:

Glass/Mo/graded CIGS<sub>2</sub>/CdS/i:ZnO/ZnO:Al/Cr/Ag/MgF<sub>2</sub>. Final cross-sectional view is as shown in Figure 18.

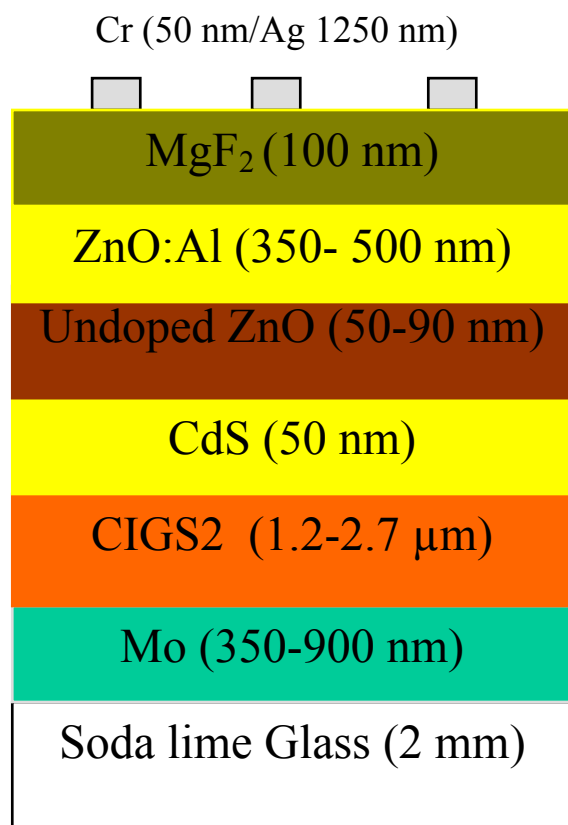


Figure 18 : Cross-sectional view of CIGS2 thin film solar cell

### **3.9. Materials Characterization**

Absorber films are first examined visually for their appearance, color, unusual features and any tendency to peel. Optical microscope is used for this purpose. Thickness and roughness of the sample are measured using a DekTak profilometer. Surface morphology of the CIGS2 thin film is studied using scanning electron microscopy (SEM). X-ray diffraction (XRD) is used to identify the crystalline phases and to measure lattice parameters. Chemical composition is analyzed by employing electron probe microanalysis (EPMA) and EDAX.. Variation of elemental composition with depth is studied using Auger electron spectroscopy (AES) in

conjunction with ion etching. More detailed microstructural study is done using a transmission electron microscope (TEM). Thickness is measured using a profilometer.

### **3.10. Current-Voltage characterization**

A reliable and robust current – voltage (I-V) measurement setup has been developed at FSEC PV Materials Lab. The setup consists of an aircooled illumination set-up which also accommodates the solar cells, which are illuminated with AM 1.5 illumination. High-accuracy power supply and multimeters have been attached to the set-up. A LabVIEW program has been developed to measure and plot the I-V characteristics. I-V measurements are carried out both in the dark and with light. Dark I-V analysis is carried out to obtain values of the fundamental parameters of the solar cell as a p-n junction diode, such as: reverse saturation current density ( $J_0$ ) and diode factor A. Analysis of light I-V characteristics of CIGS2/CdS thin film solar cells is carried out to obtain the relevant photovoltaic parameters: open circuit voltage  $V_{oc}$ , short circuit current density  $J_{sc}$ , series resistance  $R_s$ , shunt resistance  $R_p$  and fill factor (FF) and efficiency. Higher efficiency cells are sent to NREL for official I-V measurements of CIGS2/CdS thin film solar cells under AM1.5 conditions. Current-voltage characteristics are measured at NREL using Spectrolab X-25 solar simulator. The spectrum and intensity of the solar simulator are set using a spectroradiometer, primary reference cells and spectral mismatch correction factors to give the performance under the Global Reference Spectrum (IEC 60904).

### **3.11. Electrical characterization**

Electrical analysis is carried out using current-voltage set-up as explained earlier as well as quantum efficiency, capacitance-voltage measurement techniques and light beam induced current (LBIC) analysis. Quantum efficiency measures the effectiveness of a cell in converting

light of various energies into electricity. C-V technique measures the response of change in capacitance against applied voltage and can be used to find out doping density in the sample. LBIC again measures carrier collection efficiency. The technique induces the creation of electron and hole pairs in the semiconductor sample through the use of a light source and can be effectively used to find out defects in a particular region of the cell. C-V and LBIC analyses have been carried out at the Colorado State University.



## 4. RESULTS AND DISCUSSIONS

### 4.A. Cu-deficient CIGS2 absorbers

#### 4.A.1 Introduction

It is intended to vary the amount of sodium systematically. Four different thicknesses of sodium fluoride (NaF) were chosen: no NaF, 40 Å of NaF, 80 Å of NaF and 120 Å of NaF respectively. NaF was deposited by thermal evaporation on molybdenum coated glass samples. Subsequently CIGS2 thin films were prepared as explained in the experimental section.

#### 4.A.2. Materials Characterization

Large density of hillocks was observed in the sample without NaF at 500X as shown in an optical micrograph in Figure 19

These hillocks were uniformly spread all over the sample. These features were retained to some extent in the sample with 40 Å NaF (Figure 20) the shape was different than those seen in Figure 19 and here the features looked like protrusions out of a uniform film. The sample with 80 Å NaF and with 120 Å NaF contained no predominant features (Figure 21 and 22).

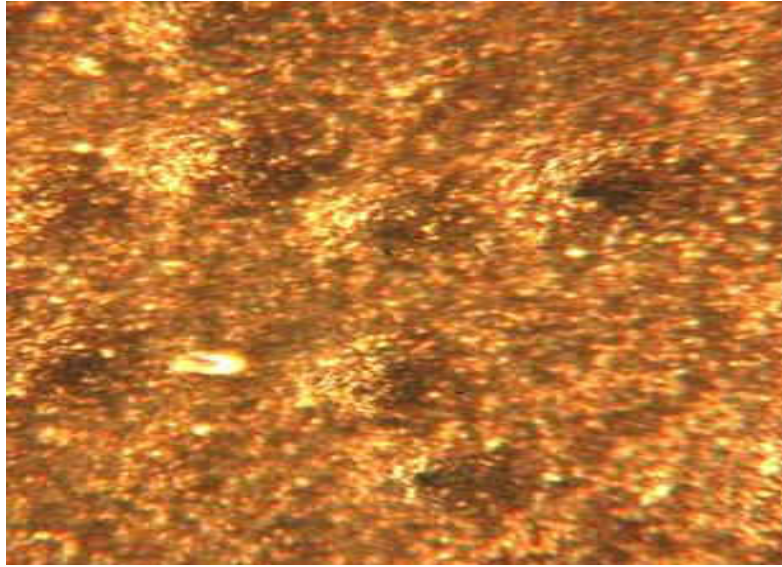


Figure 19 : Optical micrographs of a sample without NaF

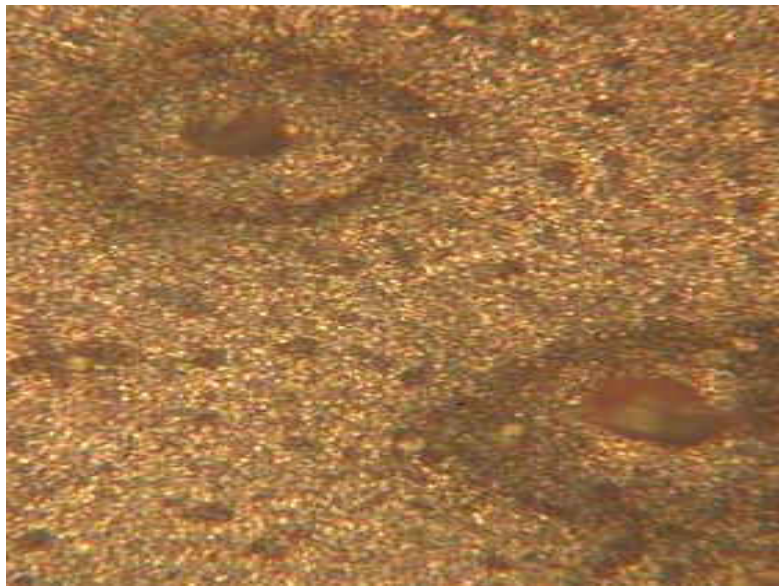


Figure 20 : Optical micrographs of a sample with 40 Å NaF

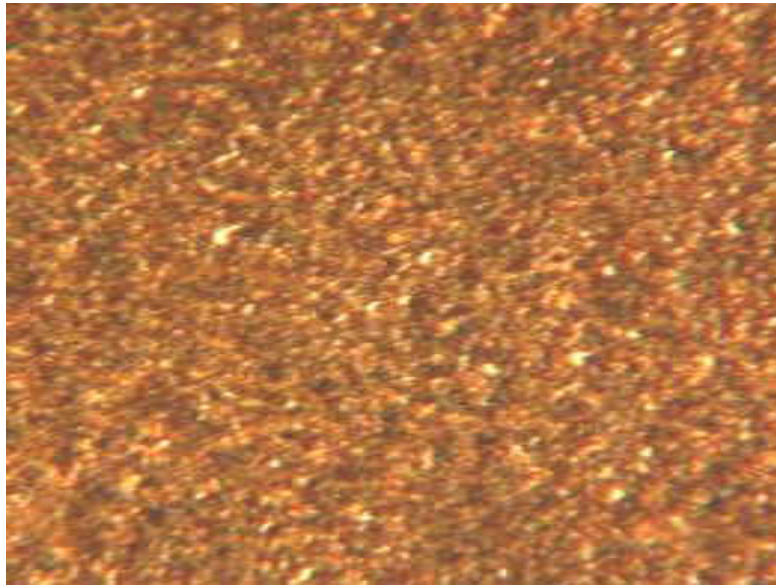


Figure 21 : Optical micrographs of a sample with 80Å NaF

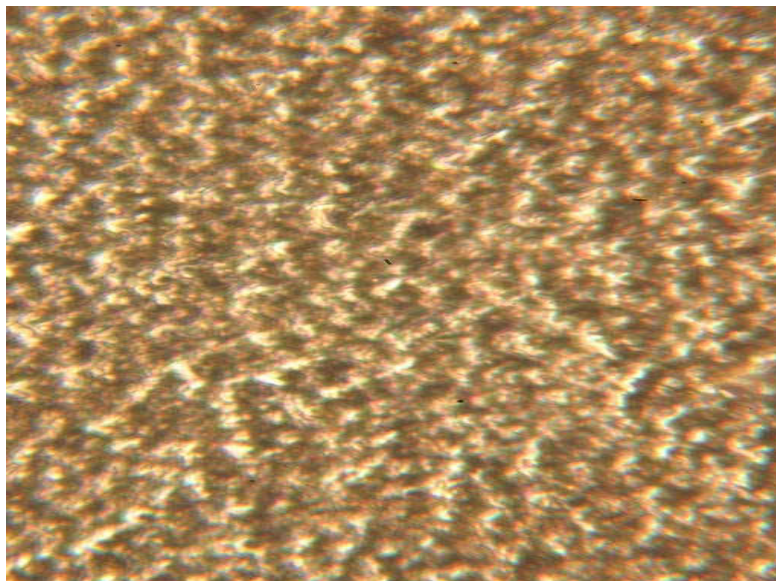


Figure 22 : Optical micrographs of a sample with 120 Å NaF

Scanning electron microscope showed features similar to those observed by optical microscopy. The sample without NaF contained predominant hillock shaped features on the background of a uniform grain structure (Figure 23) and some of these features were still

retained in the sample with 40 Å NaF as seen in Figure 24; whereas the samples with 80 Å and 120 Å NaF contained no predominant features and uniform grain structure was observed as shown in Figure 25 and 26. Some grain growth was also observed in the sample with 120 Å NaF as seen in Figure 25. The SEM images are taken at 4500X. X-Ray Energy Dispersive Spectroscopy (XEDS) spectra show that there is segregation of indium-rich phase as seen in Figure 27. Sodium enhances mobility of depositing species in the film and makes film uniform with no indium rich features as seen in Figure 28.

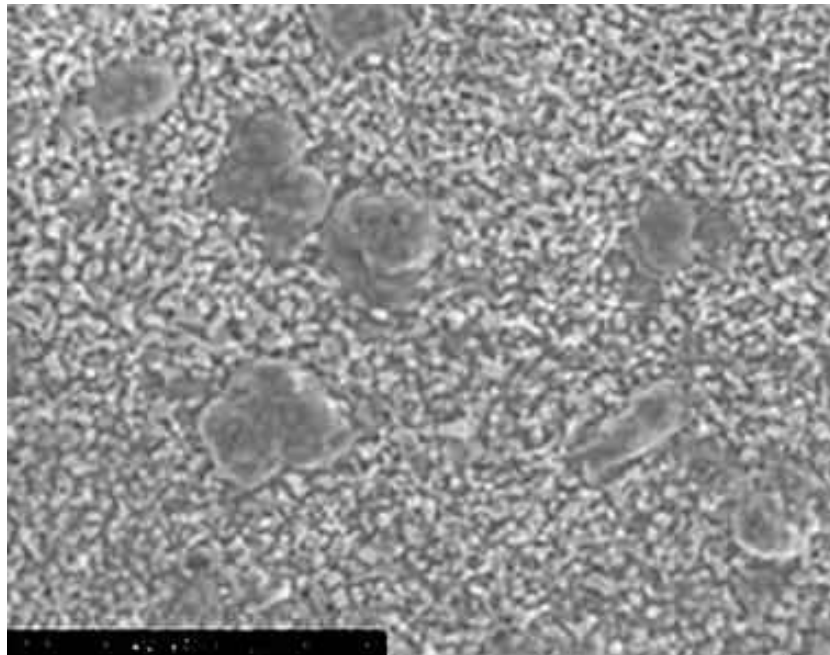


Figure 23 : SEM images of a sample without NaF

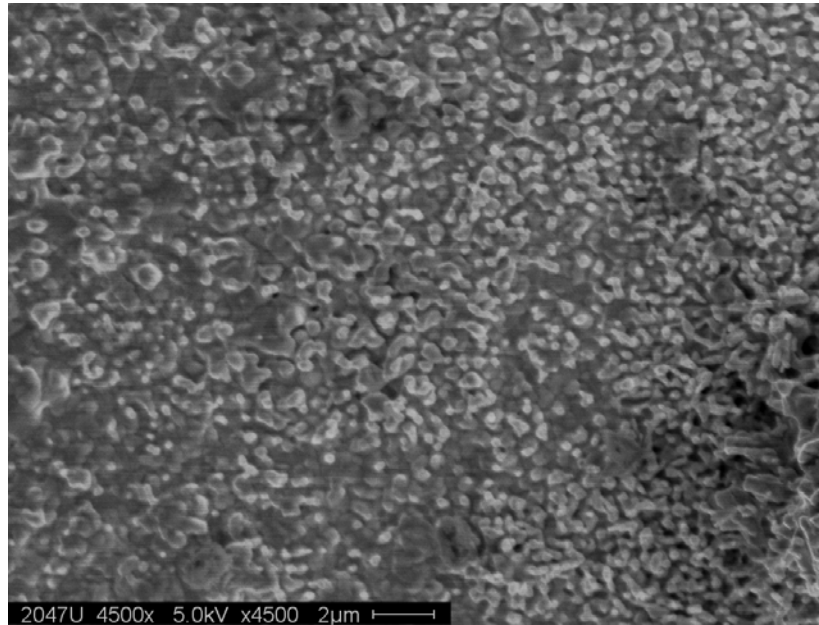


Figure 24 : SEM images of a sample with 40 Å NaF

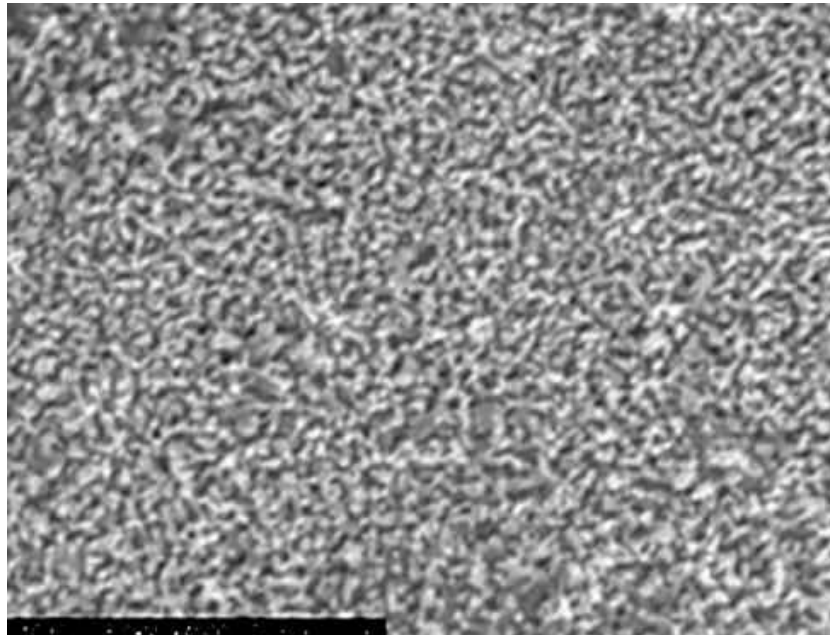


Figure 25 : SEM images of a sample with 80 Å NaF

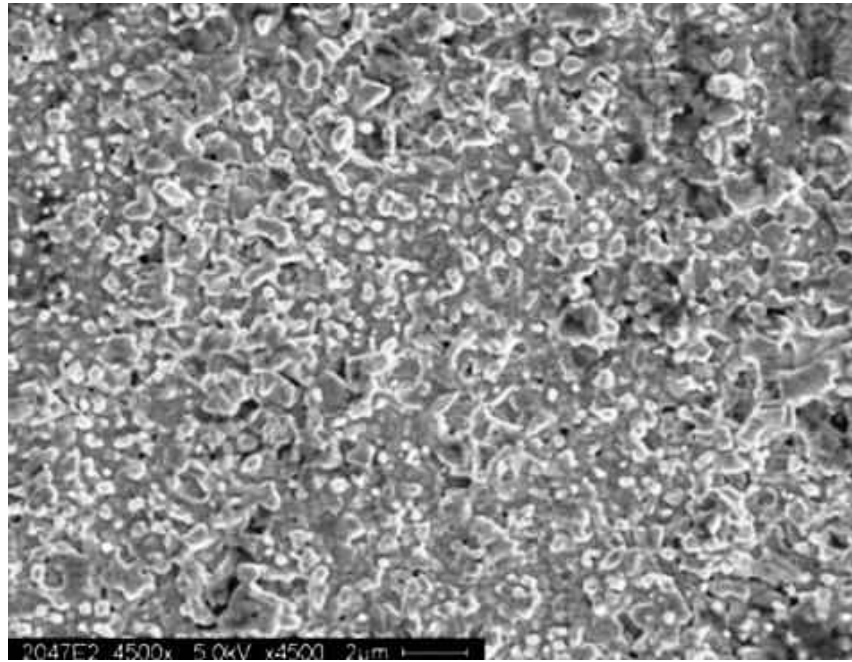


Figure 26 : SEM images of a sample with 120 Å NaF

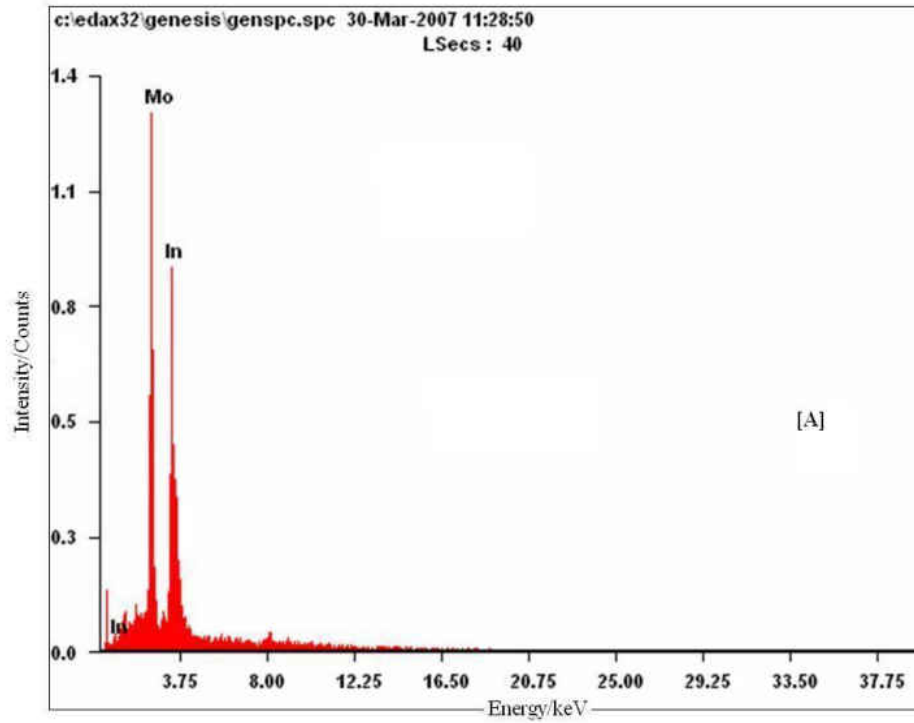


Figure 27 : XEDS spectra of indium rich hillocks region

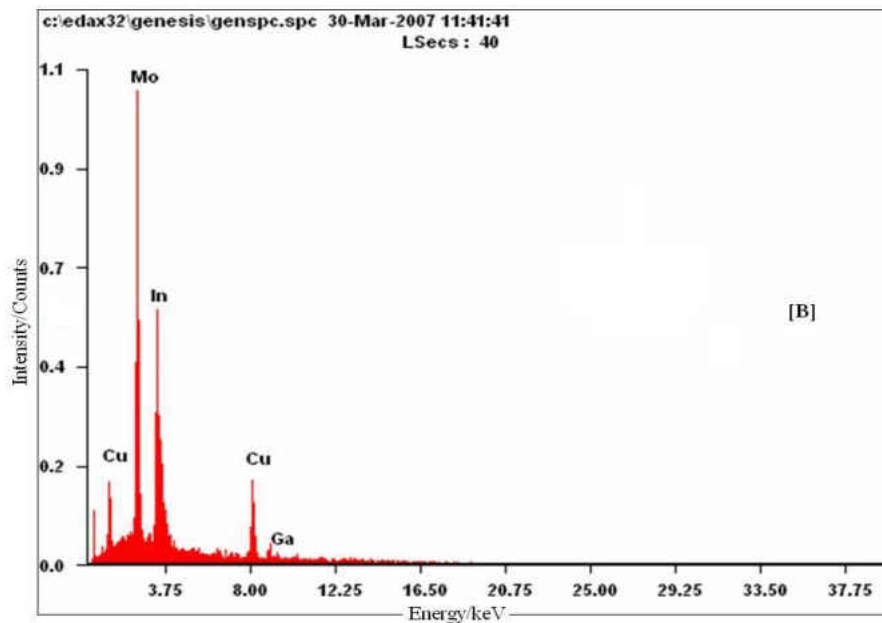


Figure 28 : XEDS spectra of film

It is clear that sodium enhances the morphology by defect reduction and increase in grain size. This is consistent with the possible models suggested by Grenata et al [26] for improvement in solar cell performance by sodium addition. In this paper, it is suggested that there are four possibilities about the mechanism by which Na works and one possibility is sodium acts as a fluxing agent and aids in defect reduction. Thus sodium results in increased mobility of depositing species and helps in effective coalescence while reducing hillock-like defects.

XRD pattern of etched CIGS2 thin film in Figure 29 shows (101), (112), (103), (200), (220), (312), (400), and (316) reflections of highly crystalline chalcopyrite CIGS2 and also reflections from molybdenum. The strongest reflection was from (112) plane at  $2\theta = 27.4^\circ$ . The calculated lattice parameters were  $a = 5.52 \text{ \AA}$  and  $c = 11.04 \text{ \AA}$  for the highest sodium containing absorber. Molybdenum reflection was observed at  $2\theta = 40.6^\circ$ . The measured maximum peak

intensity ratio of I(112)/I(220/204), for these films, was 2.7 for film without any NaF. This shows a preferred {112} orientation. The maximum peak intensity ratio increases to 2.9 for 40 Å, 3.2 for 80 Å and 3.7 for 120 Å. Strong (112) orientation with addition of NaF is consistent with results presented elsewhere in the literature [25].

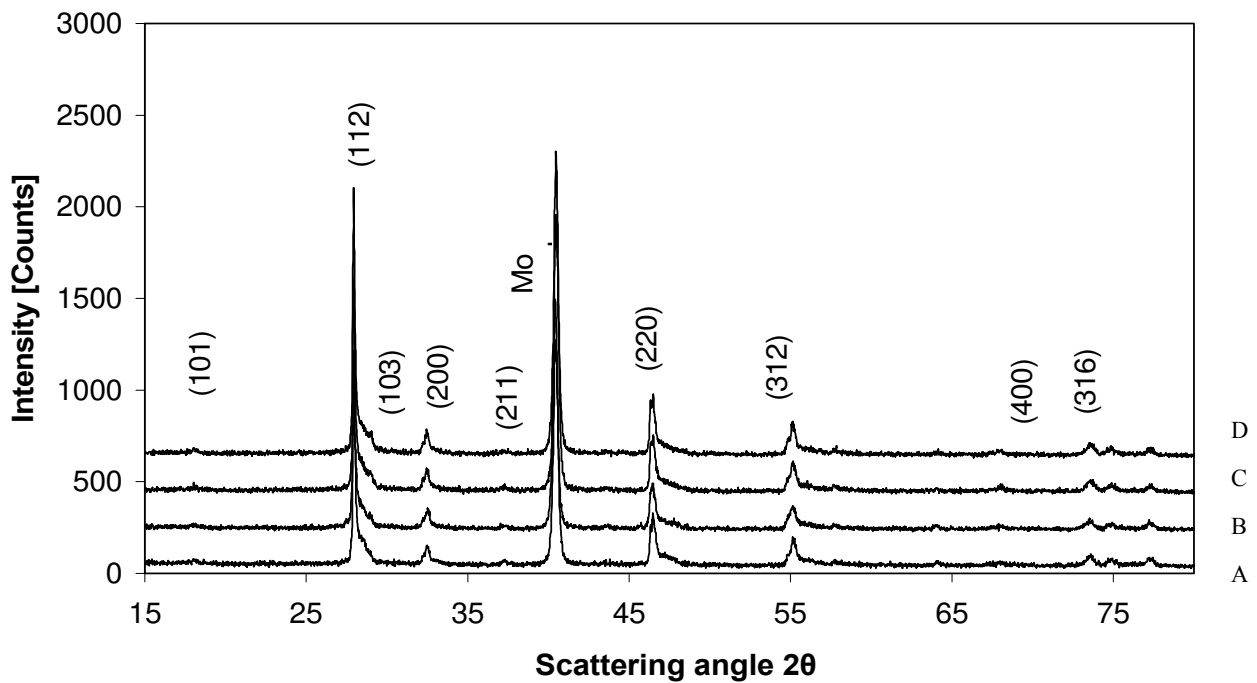


Figure 29 : XRD patterns of CIGS2 thin films for A] without NaF, B] 40 Å NaF, C] 80 Å NaF and with D] 120 Å NaF.

#### 4.A.3. Photovoltaic characteristics

Photovoltaic characteristics of CIGS2 thin film solar cells were studied using current-voltage (I-V) characteristics. The sample without any NaF has predominant hillock shaped features as seen in the micrographs earlier. These may result in possible shunting paths, thus reducing the shunt resistance. Figure 30 and Figure 31 show I-V and Q-E characteristics of the



sample without NaF respectively. It can be seen that the efficiency is very low (4.86%) and from the Q-E curve, it can be seen that there are considerable losses both in the long as well as short wavelength region. There is some improvement in the performance for the sample with 40 Å NaF as seen in Figure 32. The efficiency is 6.69% and from the Q-E curve (Figure 33), it can be seen that there are still predominant losses.

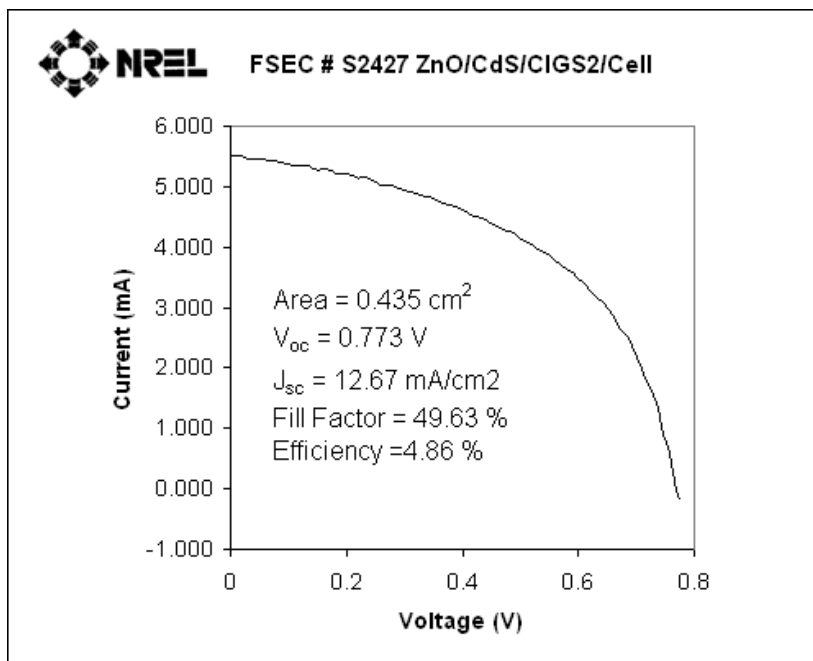


Figure 30 : I-V characteristics for sample without NaF

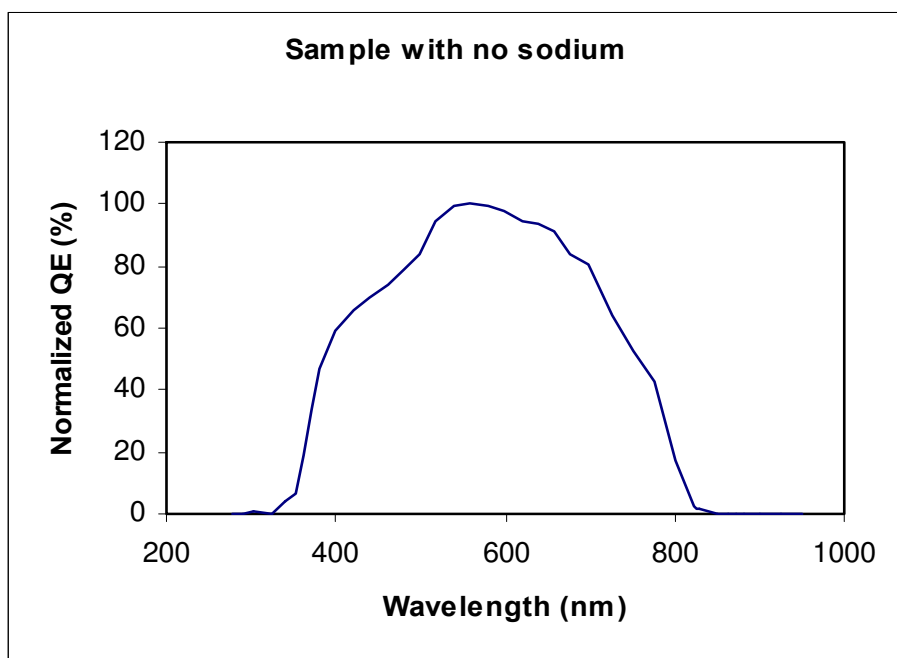


Figure 31 : Q-E characteristics for sample without NaF

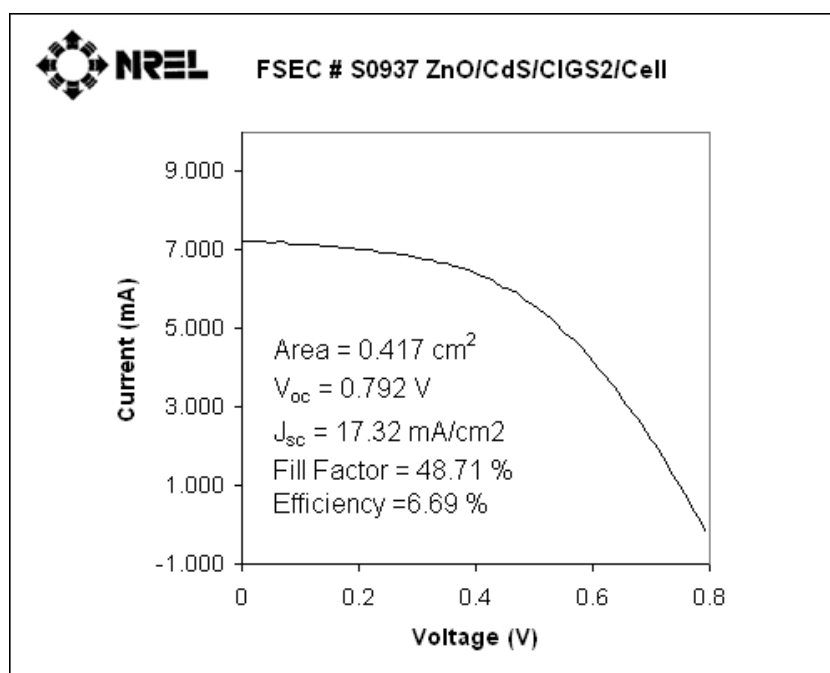


Figure 32 : I-V characteristics for sample with 40 Å NaF

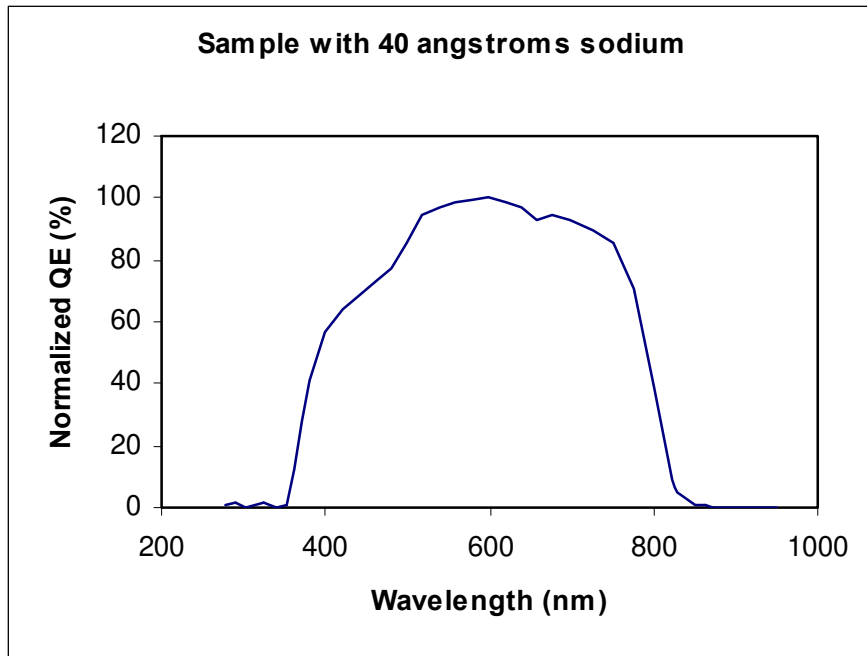


Figure 33 : Q-E characteristics for sample with 40 Å NaF

As seen in Figure 34, the efficiency for the sample with 80 Å NaF is 8.55% and from the Q-E curve in Figure 35, it can be seen that the losses are minimized. Trends in the performance for all three samples were plotted in Figure 36. Open circuit Voltage and current density shows asymptotic behavior. However, FF shows increasing trend; hence one higher level of thickness (120 Å) was experimented. As seen in Figure 37, the sample with 120 Å NaF has the efficiency of 9.15%. Figure 38 shows the Q-E curve for the sample which the best among all four samples showing minimum losses both in long as well as short wavelength region. The trends in performance for all four samples were plotted again as seen in Figure 39. Here Open circuit Voltage ,current density as well as Fill-factor start showing asymptotic behavior. Comparative quantum efficiency behavior can be seen from Figure 40.

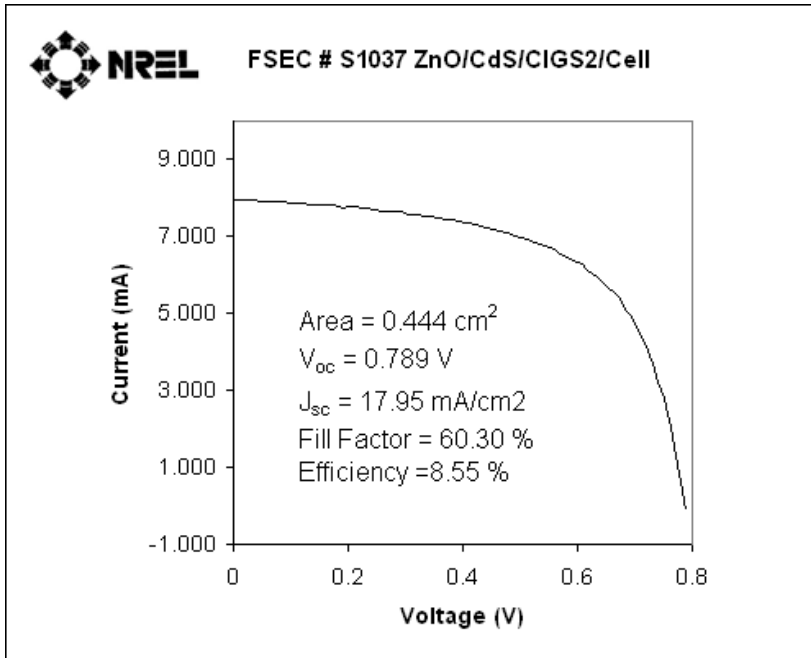


Figure 34 : I-V characteristics for sample with 80 Å NaF

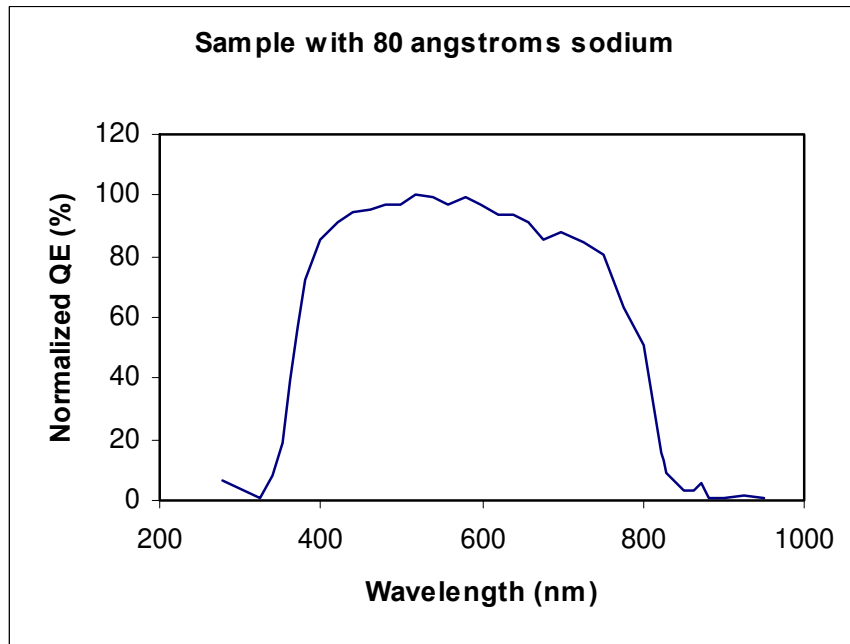


Figure 35 : Q-E characteristics for sample with 80 Å NaF

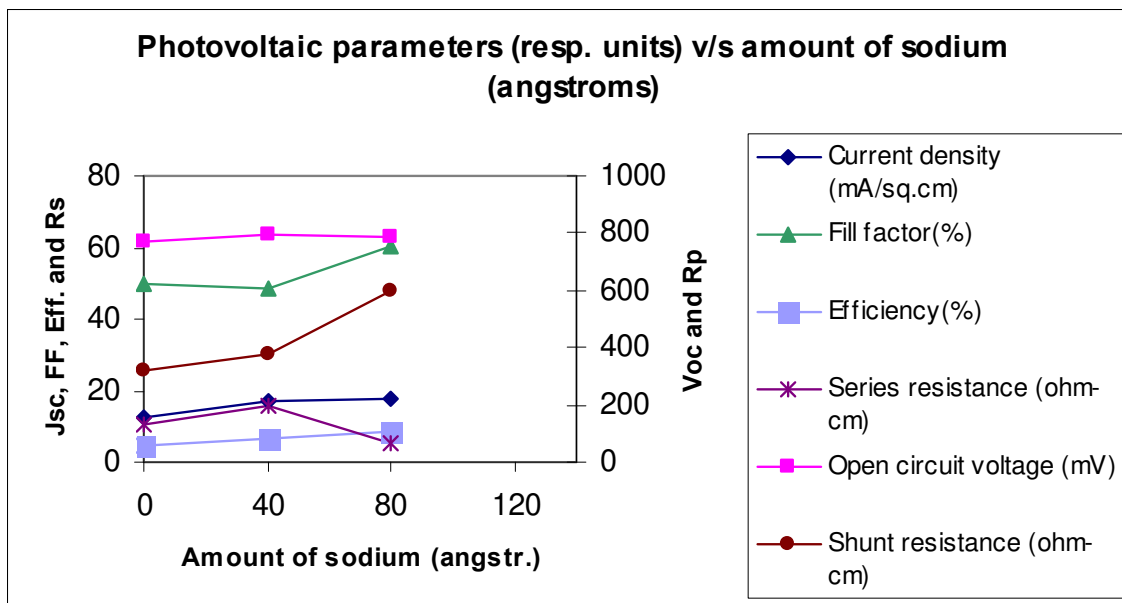


Figure 36 : Trends in performance after addition of 80 Å NaF

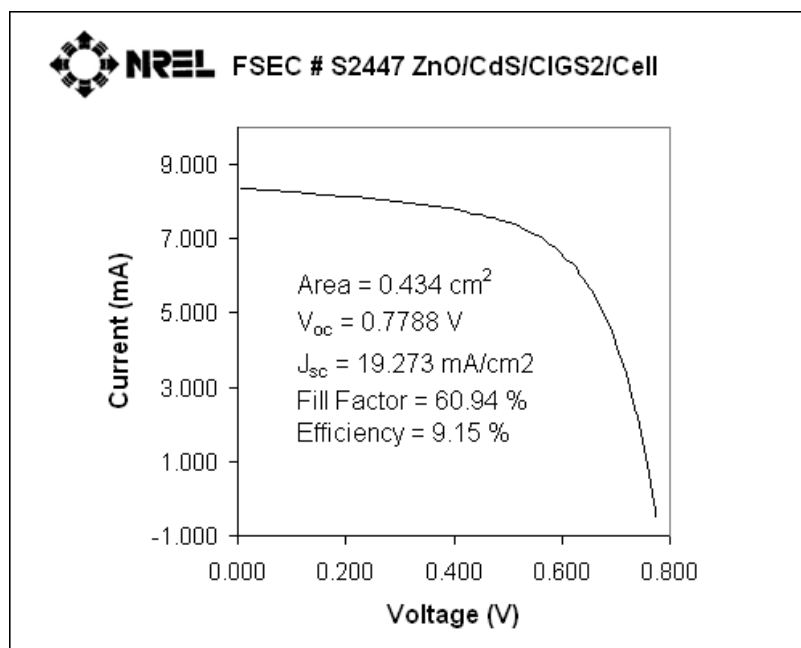


Figure 37 : I-V characteristics for sample with 120 Å NaF

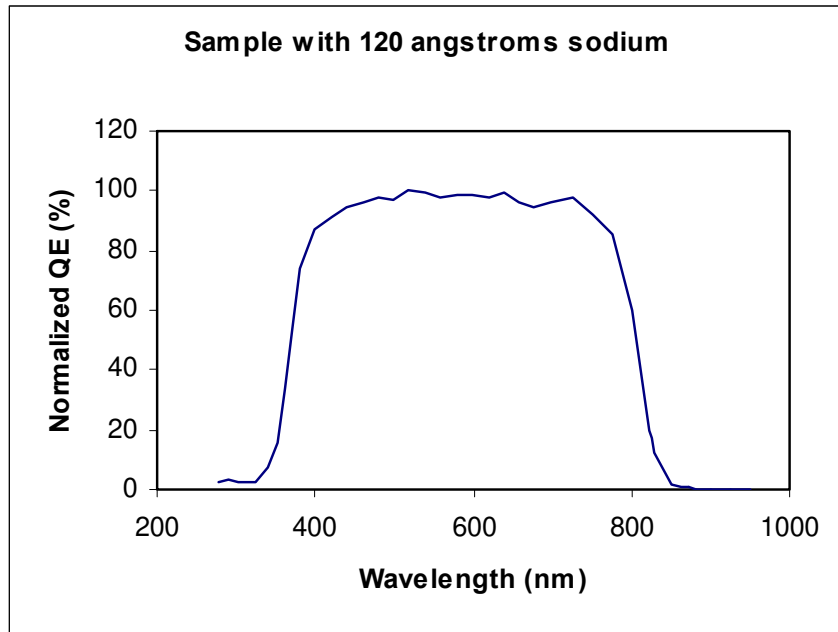


Figure 38 : Q-E characteristics for sample with 120 Å NaF

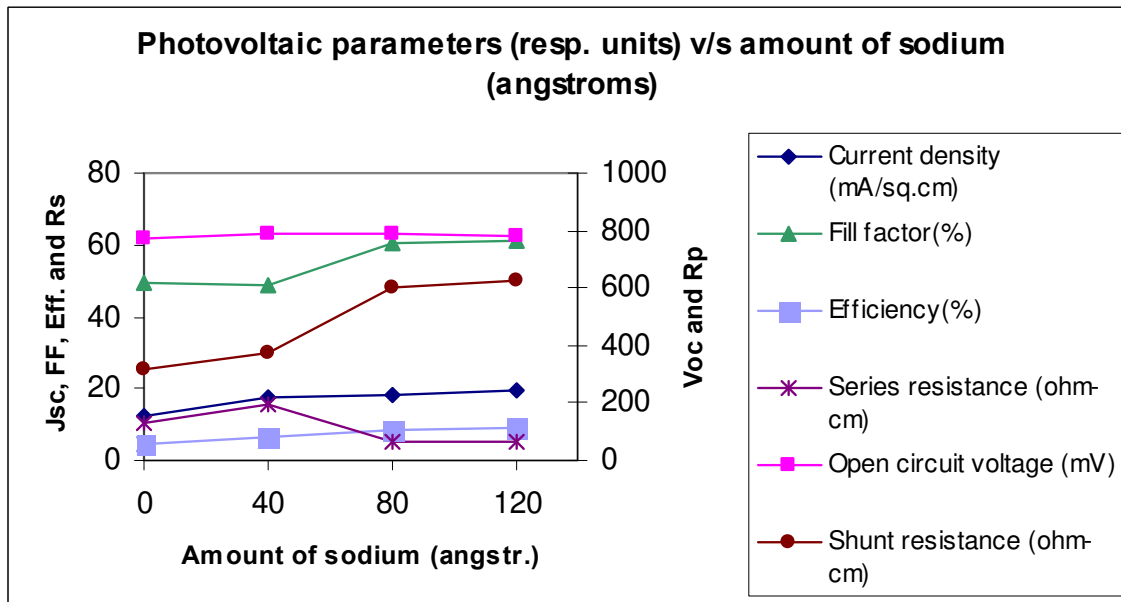


Figure 39 : Trends in performance after addition of 120 Å NaF

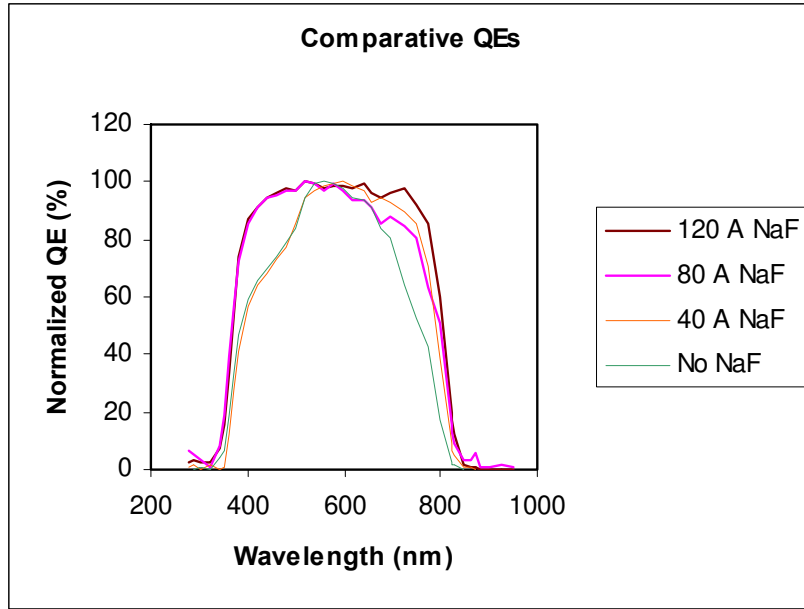


Figure 40 : Comparative Q-E curves

The efficiency data is summarized in Table I for samples of all four types.

Table I : Photovoltaic characteristics showing effect of addition of sodium

Sample	$J_{sc}$ mA/cm <sup>2</sup>	$V_{oc}$ mV	FF%	Efficiency %	$R_s$ ( $\Omega$ -cm)	$R_p$ ( $\Omega$ -cm)
No NaF	12.67	773	49.63	4.86	10.31	320.25
40 A <sup>0</sup>	17.32	792	48.71	6.69	15.42	375.56
80 A <sup>0</sup>	17.95	789	60.30	8.55	5.26	600.62
120 A <sup>0</sup>	19.27	778	60.94	9.15	5.12	625.54

Systematic addition of NaF is found to enhance the efficiencies for 80 Å and 120 Å. The change in the photovoltaic parameters for the 40 Å NaF sample is not significant because some defects are still present.

Figure 37 shows current-voltage characteristics of the highest efficiency cell. It is also seen from the table that there is considerable improvement in series and shunt resistance due to addition of sodium. It is clear that the consistent better performance after addition of sodium is due to reduction in the macro-defects. It was found that the Ra value of roughness measured using DekTakTM profilometer of the films (300-400 Å) is lower than that of copper-rich absorbers (700-800 Å). Smoothing of the films leads to lower series resistance values. Series resistance, Rs can affect current density and shunt resistance can affect open circuit voltage. Since CIGS2 films were grown in Cu-deficient regime, automatically the thickness of the films produced was smaller than those of typical films grown in Cu-rich regimes. The thickness of the films was found to be approximately 1.8 µm.

## **4.B. Cu-rich thinner CIGS2 absorbers**

### **4.B.1. Introduction**

Since CIGS2 films showed an efficiency of 9.15% even for Cu-deficient regimes for thinner films approximately 1.8 µm thickness, it was planned to reduce the thickness of CIGS2 absorbers further to 1.2 – 1.5 µm and using a copper-rich regime for which highest efficiency was already obtained at larger absorber thickness (40). In a series of experiments, CIGS2 solar cell parameters were optimized for an absorber thickness of 1.2 – 1.5 µm. To start with, the deposition and sulfurization parameters from the highest efficiency (11.99%) cell were used and



were modified appropriately as the thickness of the precursors was proportionately reduced to get an absorber thickness between 1.2 and 1.5  $\mu\text{m}$ .

#### **4.B.2. Optimization of precursor thickness**

The precursor film of copper gallium was sputtered from an alloy target containing 22 at% gallium. The sputtering parameters were 350 W power and  $1.5 \times 10^{-3}$  Torr Argon pressure. The parameters for indium were 230 W power and  $0.7 \times 10^{-3}$  Torr Argon pressure. The parameters from the highest efficiency cell were used as a starting point and the precursor deposition parameters were reduced proportionately to get absorbers in the thickness range of 1.2 to 1.5  $\mu\text{m}$ . However, the initial series of experimentation yielded the cell efficiencies in the range 4-5%; The series resistance values were higher (15 ohm-cm) and the current density values were lower ( $12.6 \text{ mA/cm}^2$ ). Since the series resistance values were higher, undoped ZnO optimization was chosen as the next step in the optimization

#### **4.B.3. Optimization of undoped-ZnO thickness**

Since CIGS2 films become rough after KCN etching, direct deposition of ZnO:Al on CdS may introduce shunting paths, hence a very thin layer of undoped ZnO is usually introduced. Undoped ZnO is a resistive layer and has an optimum value. Thickness below the optimum value leads to shunting paths and loss in open circuit voltage and more than optimum thickness leads to an increased series resistance and lower current density. It was observed that the roughness values of the thinner absorbers were better as compared to their thicker counterparts. The roughness values lowered to 300-400  $\text{\AA}$  from 700-800  $\text{\AA}$ . Hence the thickness of undoped ZnO used for original highest efficiency cell may not be needed for thinner absorbers. These

absorbers were optimized for undoped ZnO thickness value and almost half of the original optimum thickness was found to give higher efficiencies.

#### **4. B.4. Introduction of post-sulfurization dwell**

Two different sets of sulfurization processes were carried out to study the effect of post-sulfurization dwell on the properties of 1.5  $\mu\text{m}$  CIGS2 samples. First set was sulfurized using usual parameters of a dwell at 475°C for 30-60 min. Second set was sulfurized with a dwell of 30 minutes at 475°C and a post-sulfurization dwell at 500°C for 30 minutes was carried out without any  $\text{H}_2\text{S}$ .

#### **4. B.5. Materials Characterization**

SEM micrographs of a 1.5  $\mu\text{m}$  CIGS2 samples are shown in Figures 41 and 42. The SEM images are taken at 5500 X. Figure 41 shows sample without end dwell and Figure 42 shows sample with post-sulfurization dwell at 500°C for 30 minutes without  $\text{H}_2\text{S}$ . The grain size as measured by the line intercept method was 1.0  $\mu\text{m}$  for the sample with no end dwell and 1.4  $\mu\text{m}$  for the sample with end dwell. Figure 42 shows well-faceted, compact grains for the sample with 1.5  $\mu\text{m}$  thick absorber. It can be seen that post-sulfurization dwell has improved the grain size. It was seen that samples with this end dwell treatment exhibit better photo-conversion efficiencies Hence the same process was used for carrying out experiments on a 1.2  $\mu\text{m}$  absorber. Figure 43 shows sample with 1.2  $\mu\text{m}$  thick absorber.

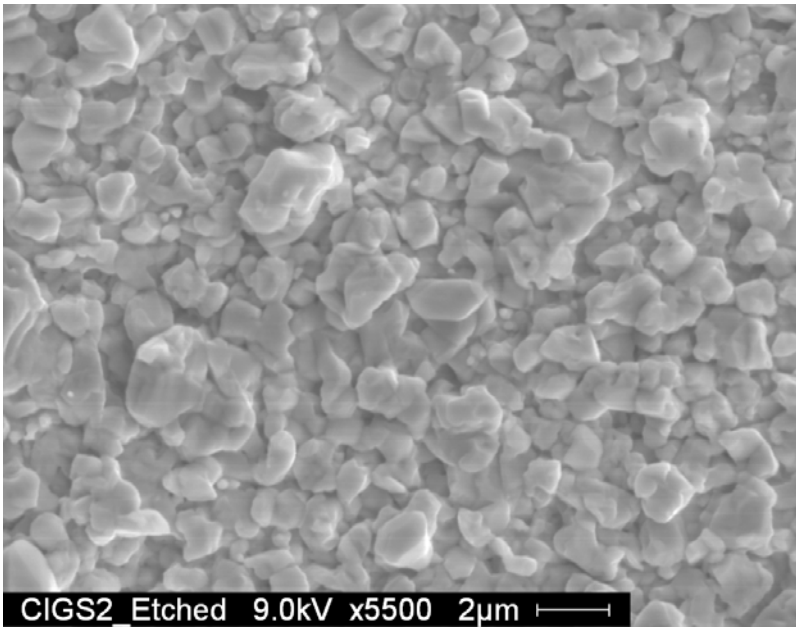


Figure 41 : 1.5 μm absorber sample without dwell.

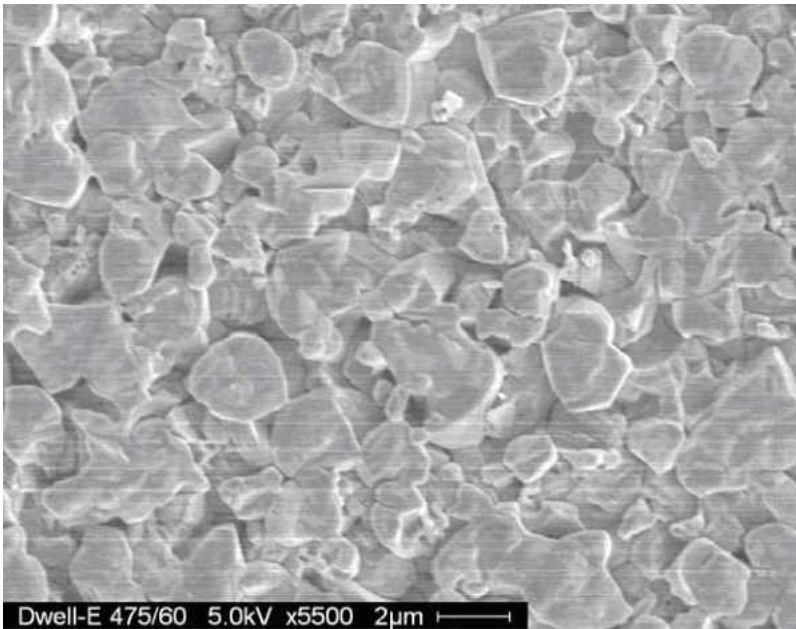


Figure 42 : 1.5 μm absorber sample with end dwell at 500°C for 30 minutes.

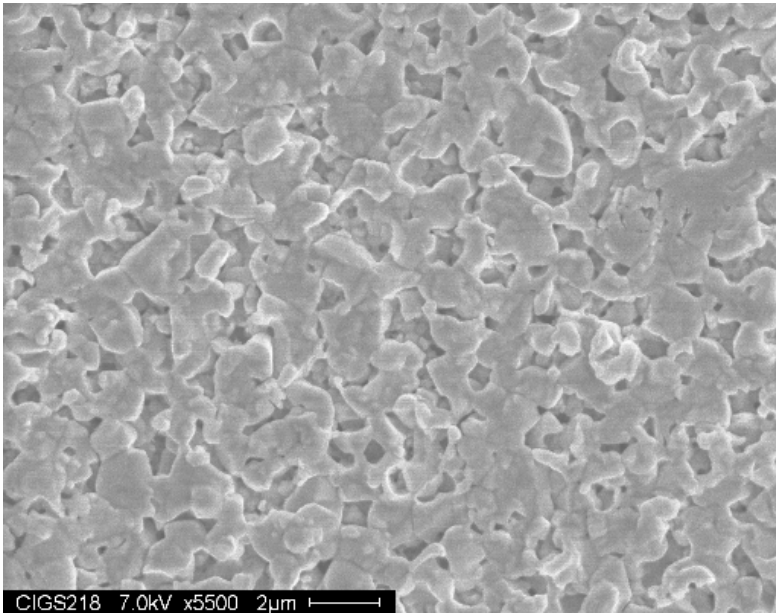


Figure 43 : 1.2  $\mu\text{m}$  absorber sample with end dwell at 500°C for 30 minutes.

XRD pattern of an etched CIGS2 thin film shows (101), (112), (103), (200), (220), (312) and (316) reflections of highly crystalline chalcopyrite CIGS2 and also reflections from molybdenum (Figure 44) for a sample with absorber thickness 1.5  $\mu\text{m}$  sulfurized with an end dwell. The strongest reflection was from (112) plane at  $2\theta = 28.04^\circ$ . The calculated lattice parameters were  $a = 5.49 \text{ \AA}$  and  $c = 11.12 \text{ \AA}$ . Molybdenum reflection was observed at  $2\theta = 40.66^\circ$ . XRD peaks exhibit reduction in peak intensity with reduction in absorber thickness while as expected Mo peak becomes stronger for a 1.2  $\mu\text{m}$  absorber.

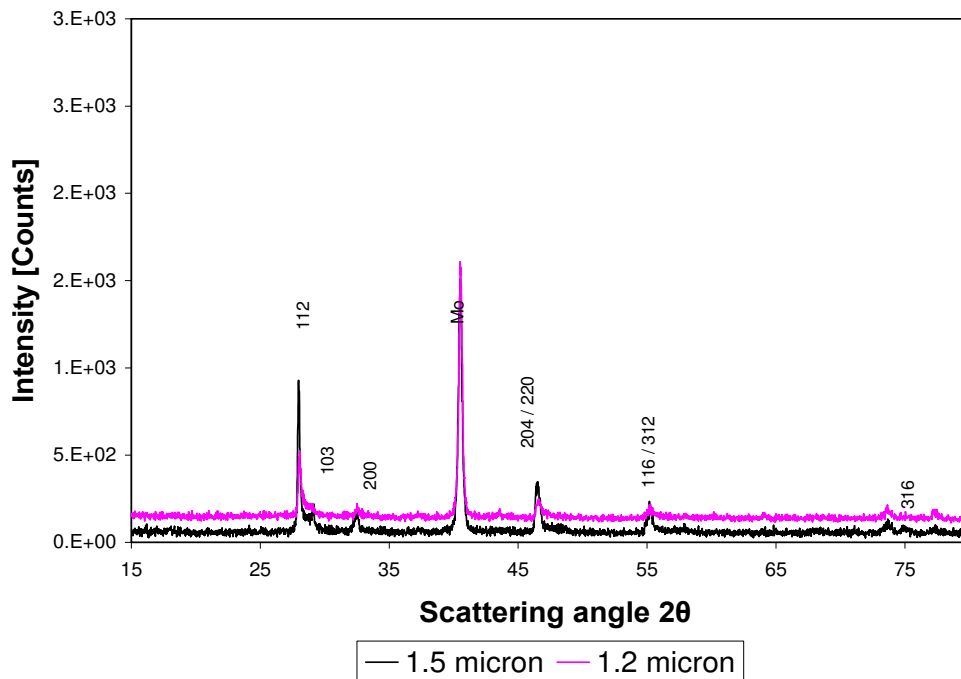


Figure 44 : XRD spectra for 1.5  $\mu\text{m}$  and 1.2  $\mu\text{m}$  absorbers (with end dwell)

Figure 45 and Figure 46 show AES depth profiles for CIGS2 samples with 1.5  $\mu\text{m}$  and 1.2  $\mu\text{m}$  absorber thicknesses. 1.5  $\mu\text{m}$  sample does not show any gallium gradient towards the backcontact. Copper and sulfur intensities are constant in the CIGS2 thickness. As has been observed earlier, for sample with thickness 1.2  $\mu\text{m}$ , gallium is increasing towards back contact while indium is decreasing. This happens as the reaction of gallium with sulfur is slower than that of indium with sulfur. Hence, gallium is not incorporated in the top layer and accumulates at the bottom of the solar cell near the back contact forming a gallium rich chalcopyrite layer. This is also due to the tendency of smaller atoms viz. Ga to migrate towards the region of stress.

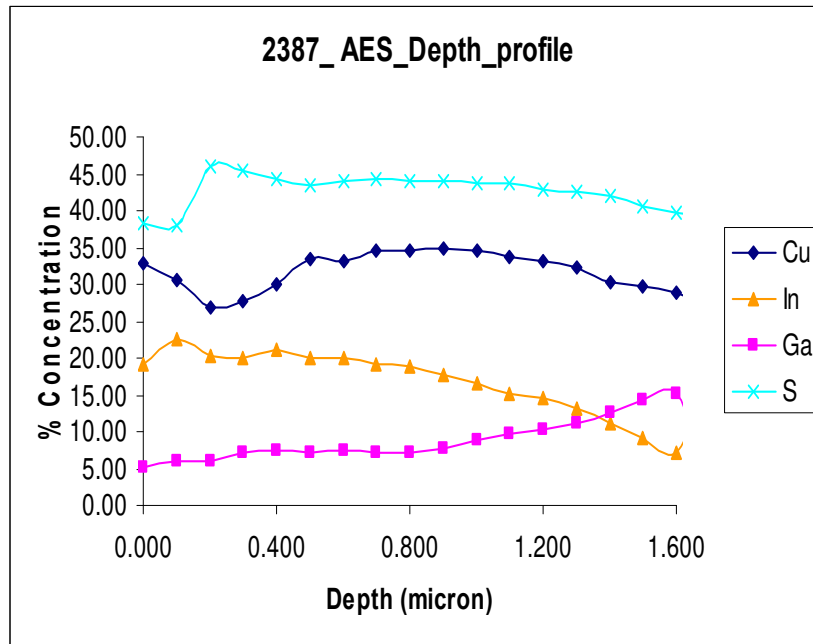


Figure 45 : AES depth profile for a 1.5 μm absorber sample (with end dwell)

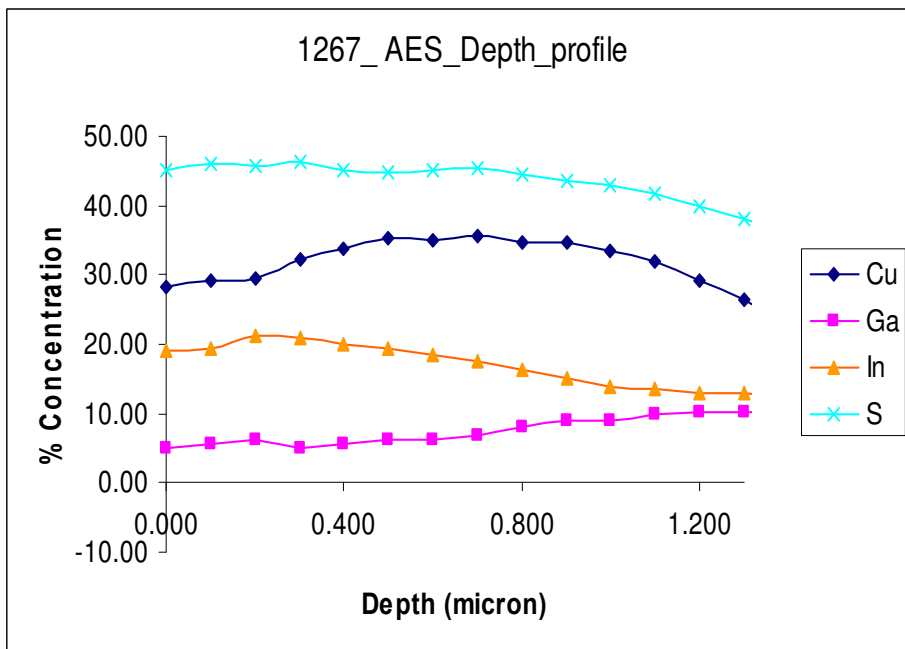


Figure 46 : AES depth profile for a 1.2 μm absorber sample (with end dwell)

Figures 47, 48 and 49 show TEM images for a CIGS2 solar cell with 1.2  $\mu\text{m}$  absorber thickness. TEM images show no porosity at the CIGS2/Mo interface and there is some porosity in the bulk. This porosity may be already present in absorber or may also have been introduced during the TEM sample preparation.

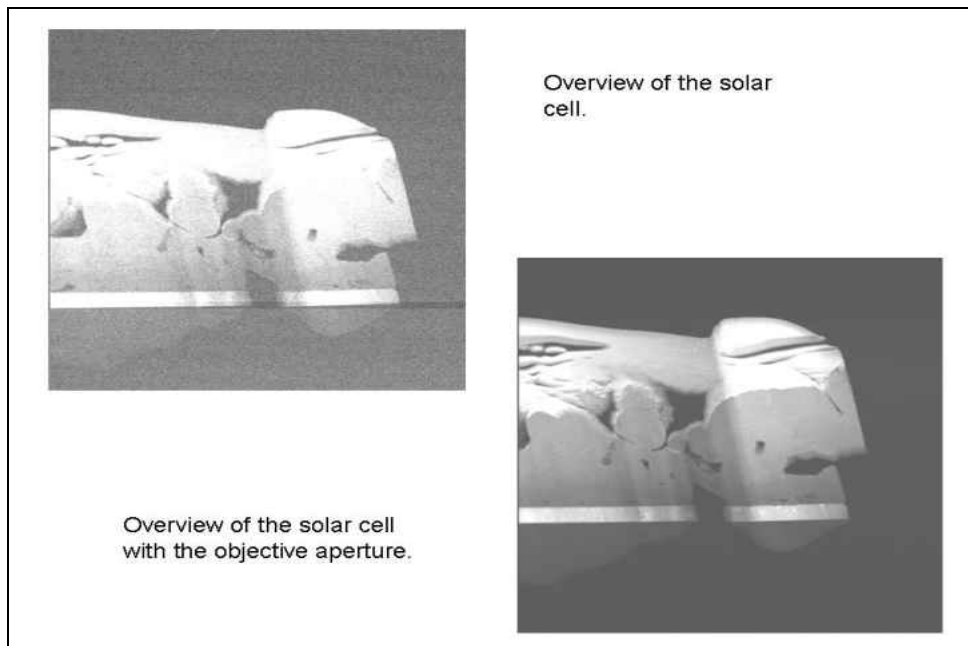


Figure 47 : TEM overview of the 1.2  $\mu\text{m}$  absorber sample solar cell

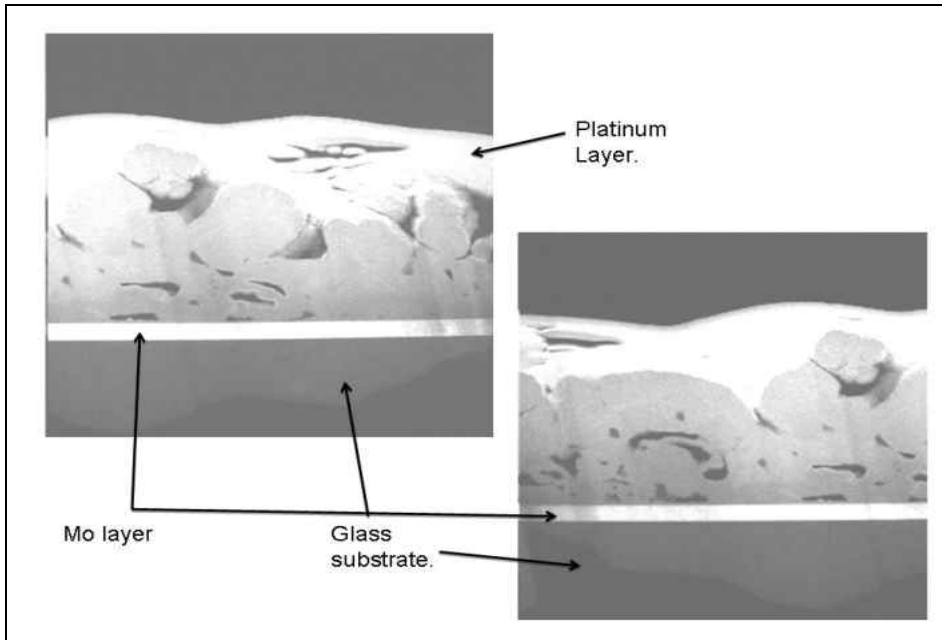


Figure 48 : TEM cross-section of the sample

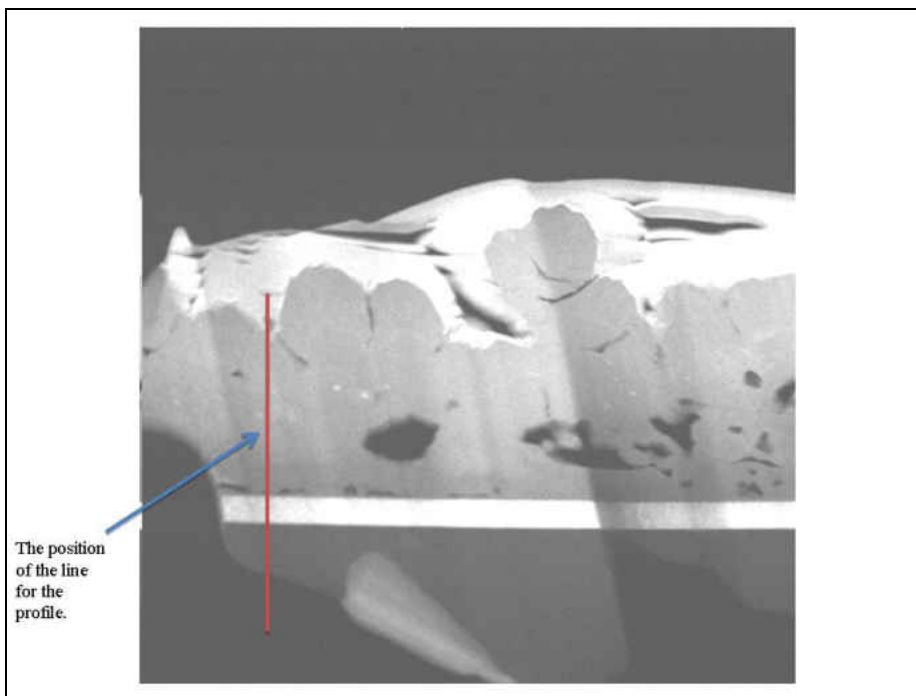


Figure 49 : TEM image showing position of the line scan in the cross-section



Figure 50 shows a line scan profile of peak height of elements versus depth. The oxygen peak (red) seen beneath the back contact is due to the sodalime substrate. At the depth of  $\sim 2 \mu\text{m}$  on the X-axis, two very intense molybdenum peaks (orange and purple) are seen from the Mo back contact. Between X-axis depth positions of  $0.7 \mu\text{m}$  to  $2 \mu\text{m}$ , elemental peaks from CIGS2 absorber layer are seen. Sulfur peak (orange) shows the maximum intensity followed by copper peak (yellow). Copper and sulfur signals are constant in the absorber bulk. This is followed by indium (orange) peak decreasing towards back contact and gallium (azure) peak increasing towards back contact. The cadmium (red) peak in the absorber region may be due to the inward diffusion of Cadmium in CIGS2. Zinc (green) and Oxygen (red) peaks are seen from the surface to a depth of  $0.7 \mu\text{m}$  from the transparent and conducting ZnO/ZnO: Al bilayer. Gallium signal is also seen in the ZnO region. This is due to the trace amount of gallium introduced during the focused ion beam (FIB) sample preparation.

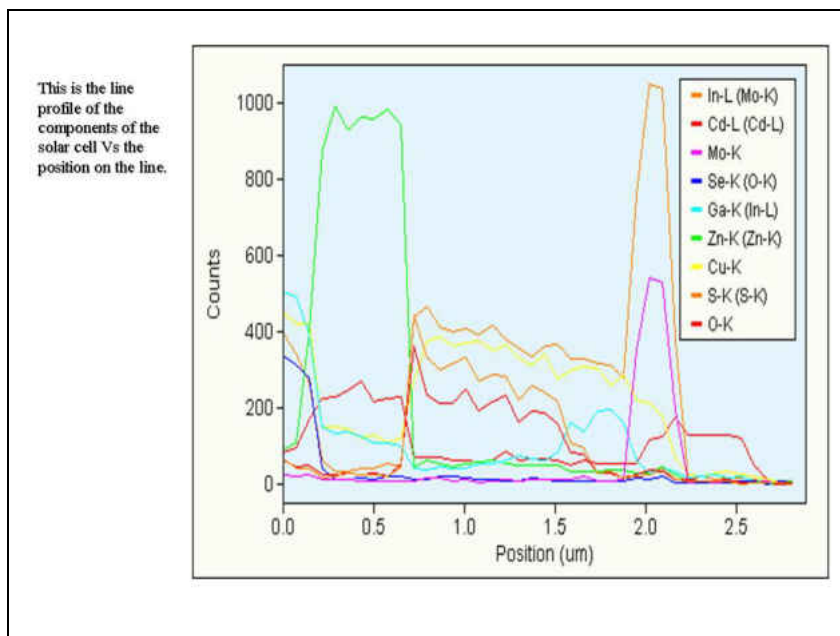


Figure 50 : Line profile of the components of the solar cell against the position on the line

#### 4. B.6. Electrical characterization

The sample sulfurized with no end dwell was studied thoroughly for various types of electrical characterization. Figure 51 shows the I-V characteristics measured at the National Renewable Energy Center (NREL) under AM1.5 conditions. Photovoltaic characteristics of the were as follows: short circuit current density,  $J_{sc}$  of  $17.52 \text{ mA/cm}^2$ , open circuit voltage,  $V_{oc}$  of  $751.8 \text{ mV}$ , fill factor, FF of  $66.34\%$  and photovoltaic conversion efficiency,  $\eta$  of  $8.74\%$ .

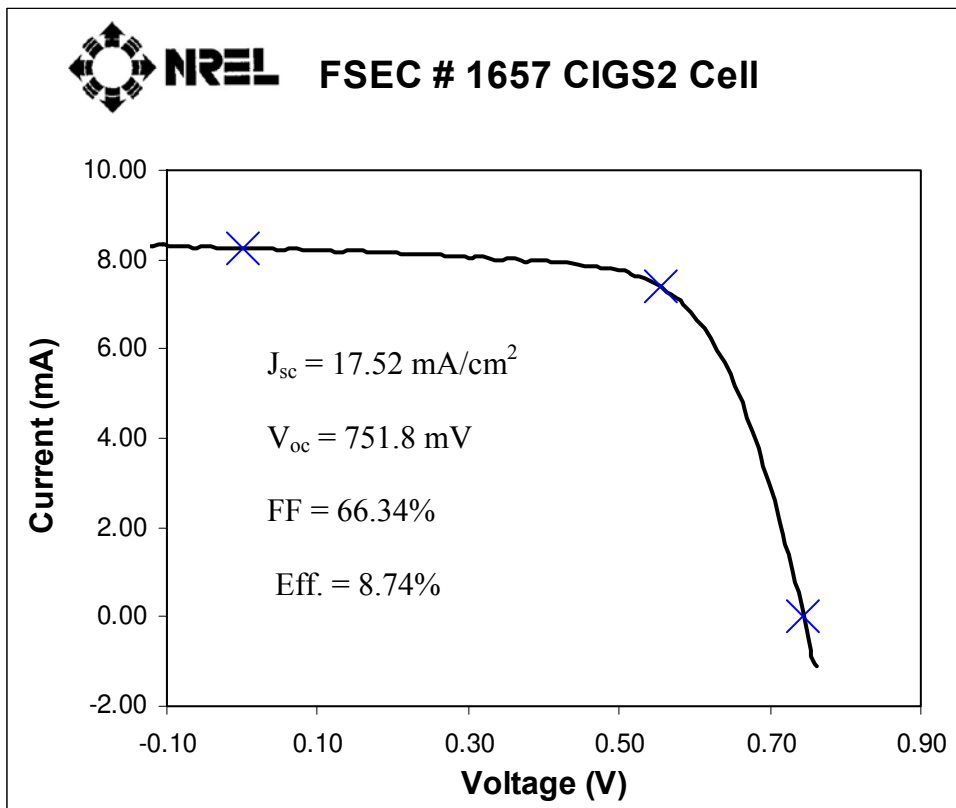


Figure 51 : I-V characteristics of the 1657 cell

Plot of  $dJ/dV$  with voltage was plotted from the J-V characteristics as shown in Figure 52. The dark curve gives a shunt resistance of  $4206 \Omega\text{-cm}^2$ . This is even better as compared to

that of the champion cell ( $2500 \Omega\text{-cm}^2$ ) [67]. The improvement in shunt resistance again indicates good heterojunction partner layer and an optimized layer of i-ZnO, due to which, there are small number of shunting paths [68]. Figure 53 shows a plot of the diode factor, A and reverse saturation current,  $J_0$  versus  $\ln [J (\text{dark})]$  for the cell. As compared to the champion cell, the diode factor increased from 1.69 to 2.18 and reverse saturation current density increased from  $1.04 \times 10^{-10} \text{ mA/cm}^2$  to  $1.78 \times 10^{-8} \text{ mA/cm}^2$  [67]. There is an increase in diode factor and reverse saturation current density when the absorber thickness is decreased. Deterioration in these photovoltaic parameters indicates an increase in the space charge region (SCR) recombination due to the presence of more non-radiative recombination centers. Detailed investigations of the recombination mechanisms have established that space charge region recombination is the dominant limiting factor [69]. Grain boundaries act as non-radiative recombination centers. Hence deterioration in the values of A and  $J_0$  can be attributed to a decrease in the grain size when the absorber thickness is decreased.

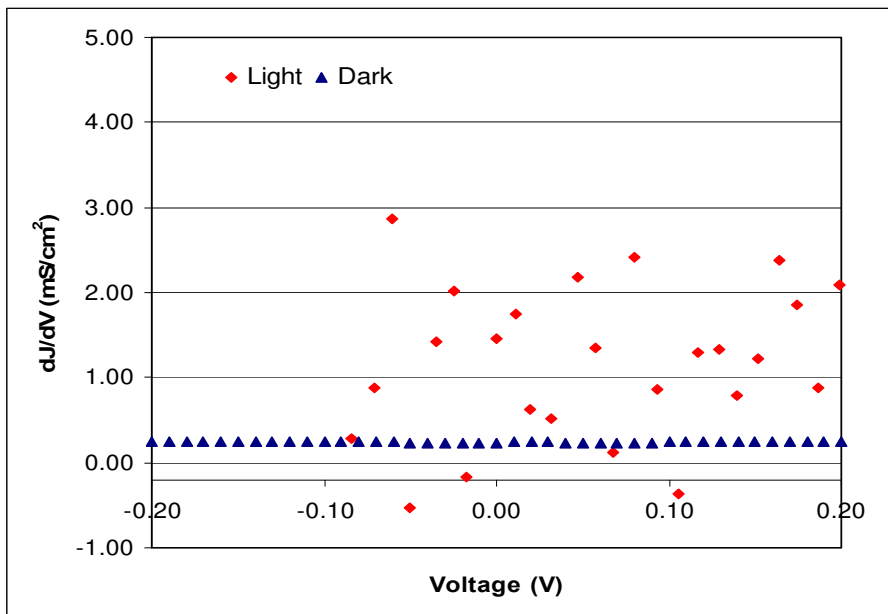


Figure 52 : Plot of  $dJ/dV$  v/s V

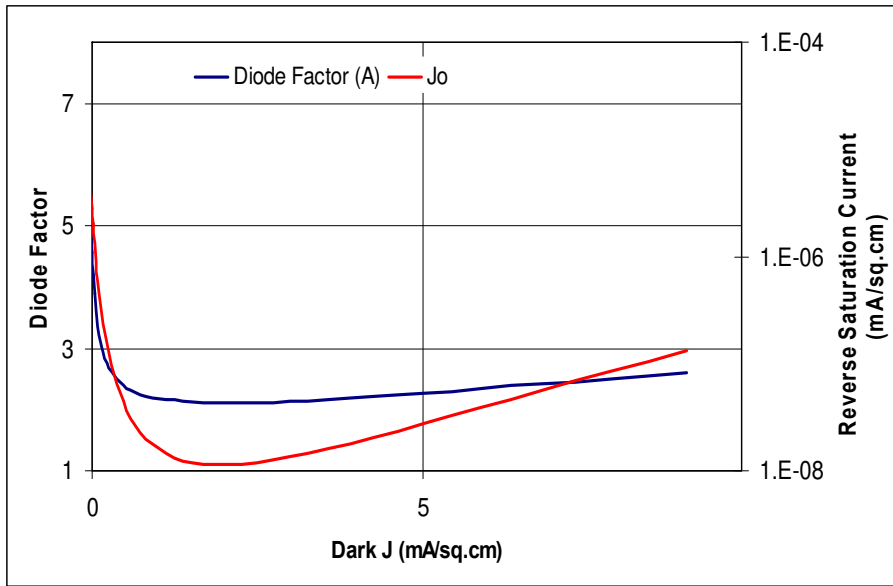


Figure 53 : Plot of the diode factor, A and reverse saturation current, Jo versus Ln [J (dark)]

Figure 54 shows dependence of the open circuit voltage on temperature. Intercept of the linear extrapolation with the  $V_{OC}$  (T) axis again suggests an absorber band gap value of approximately 1.4 eV.

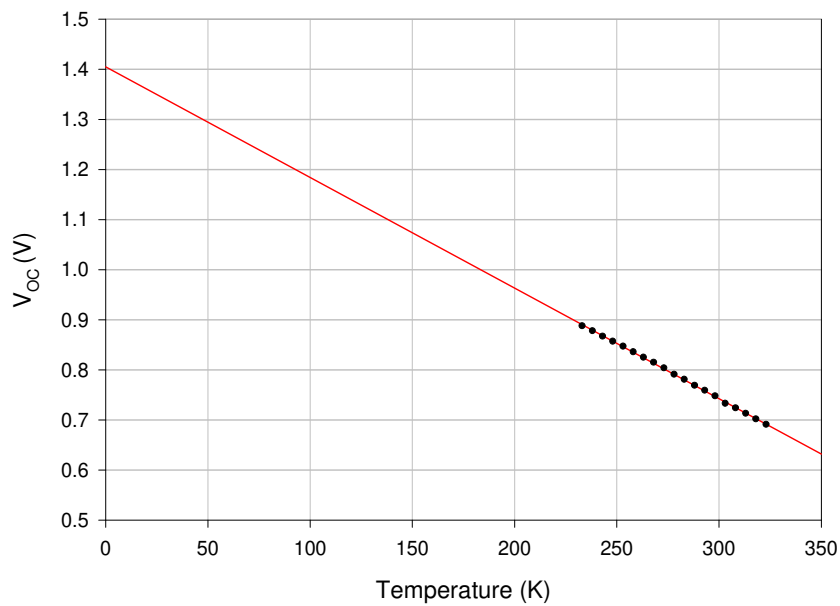


Figure 54 : Bandgap determination

Figure 55 shows  $C^{-2}$  dependence on voltage.

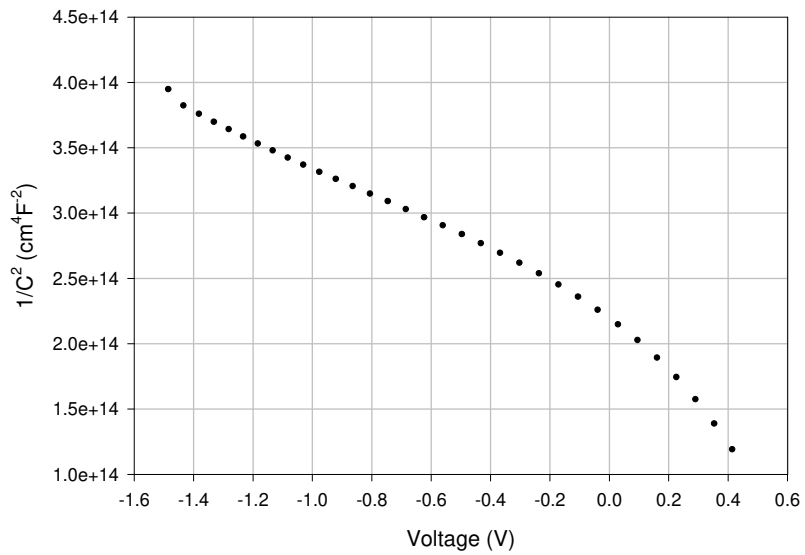


Figure 55 :  $1/C^2$  versus V

Figure 56 shows carrier density dependence on position relative to the junction.

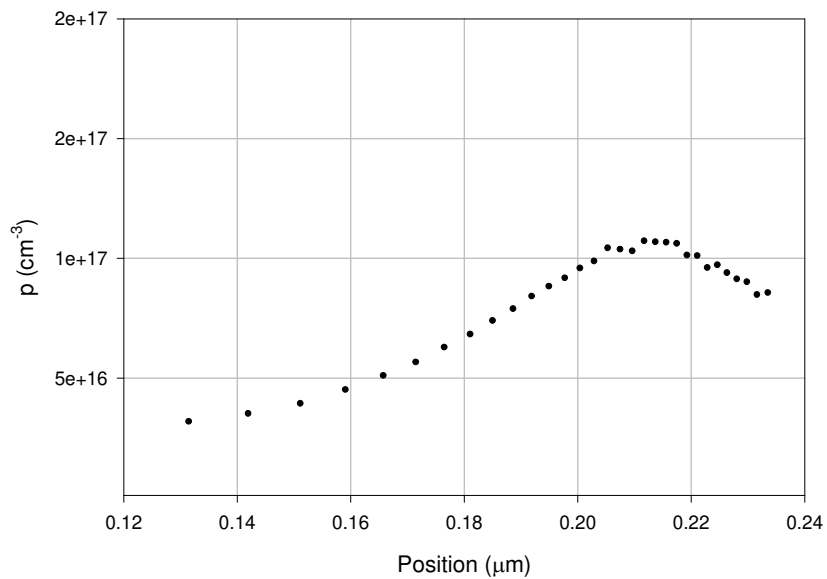


Figure 56 : Carrier density dependence on position relative to the junction.

Figure 57 shows Fermi level relative to the valence band as function of distance from the p-n junction obtained from capacitance-voltage measurements at room temperature. Fermi level is approximately 0.14 eV above the valence band in the bulk.

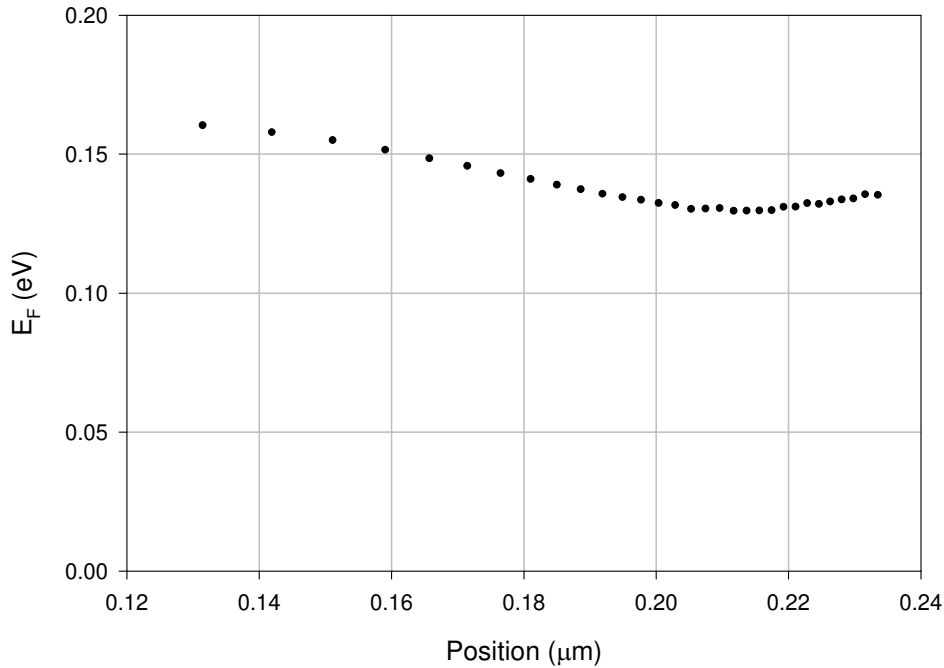


Figure 57 : Fermi level relative to the valence band as a function of distance from the p-n junction.

Results from light beam induced current (LBIC) measurements performed with 638-nm laser at three different resolutions are shown in Figures 58, 59 and 60. LBIC map is accompanied with a histogram which gives a slightly more quantitative estimate of device uniformity. One of the devices was scanned at different voltages with low resolution and one feature on that device was also scanned with a medium resolution at four different voltages.

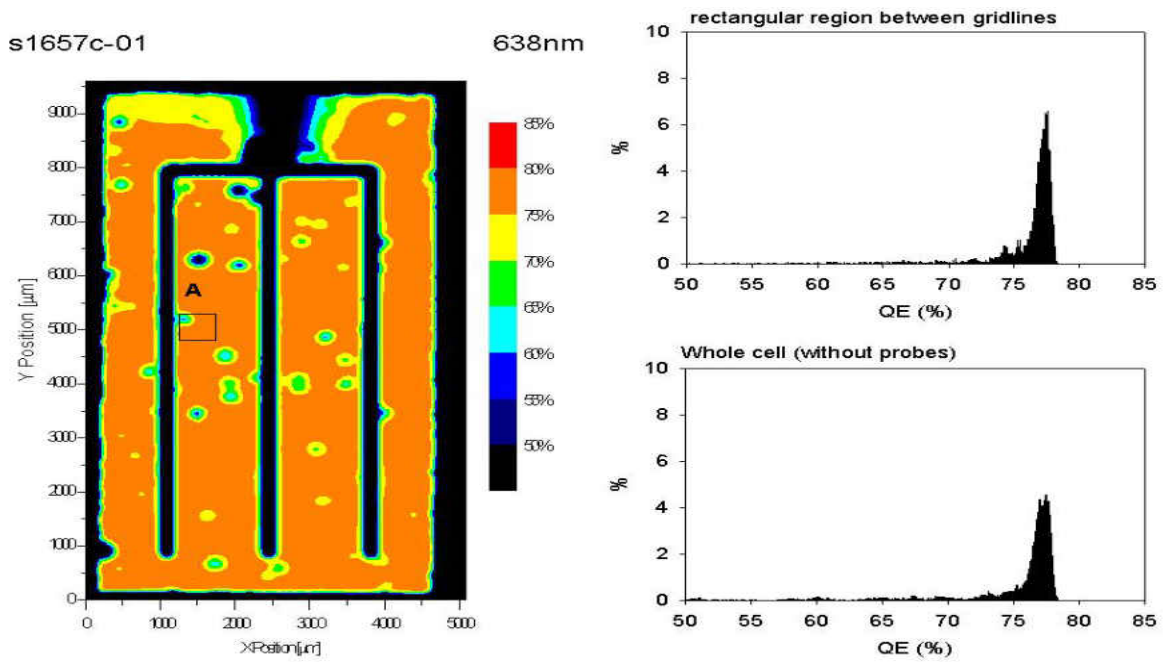


Figure 58 : LBIC images.

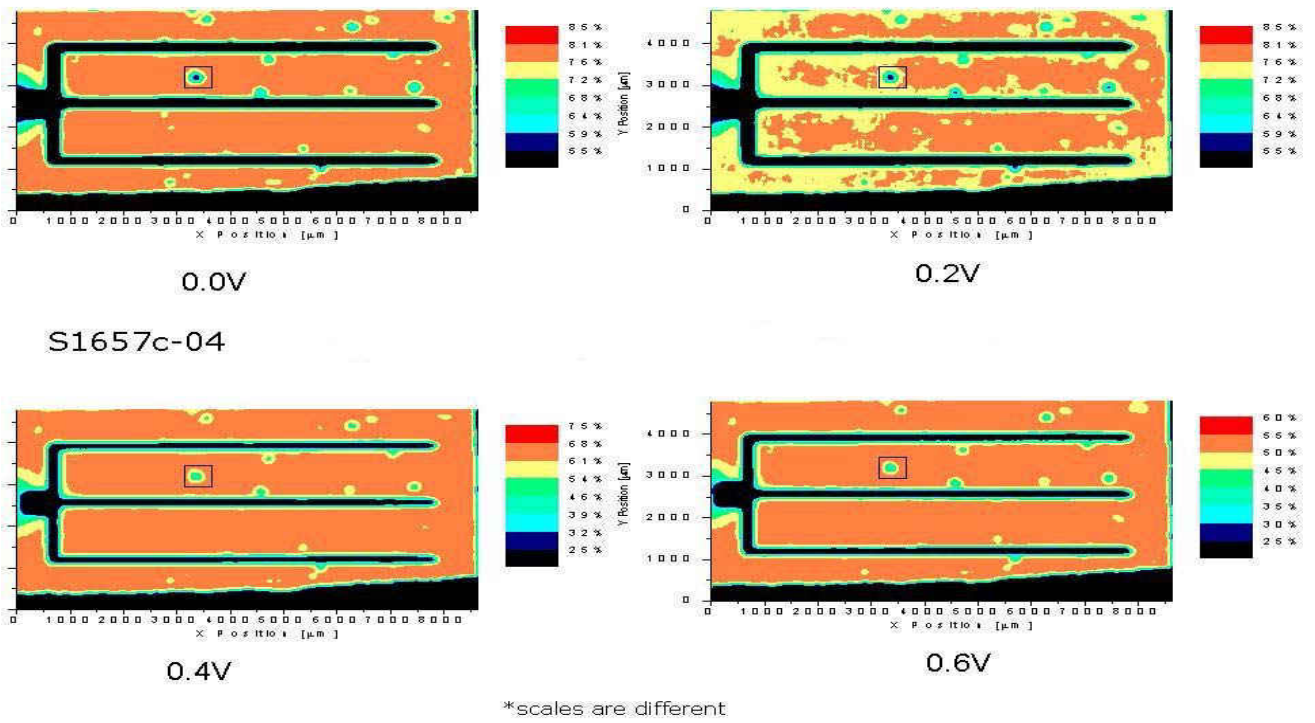


Figure 59 : LBIC at different operating biases.

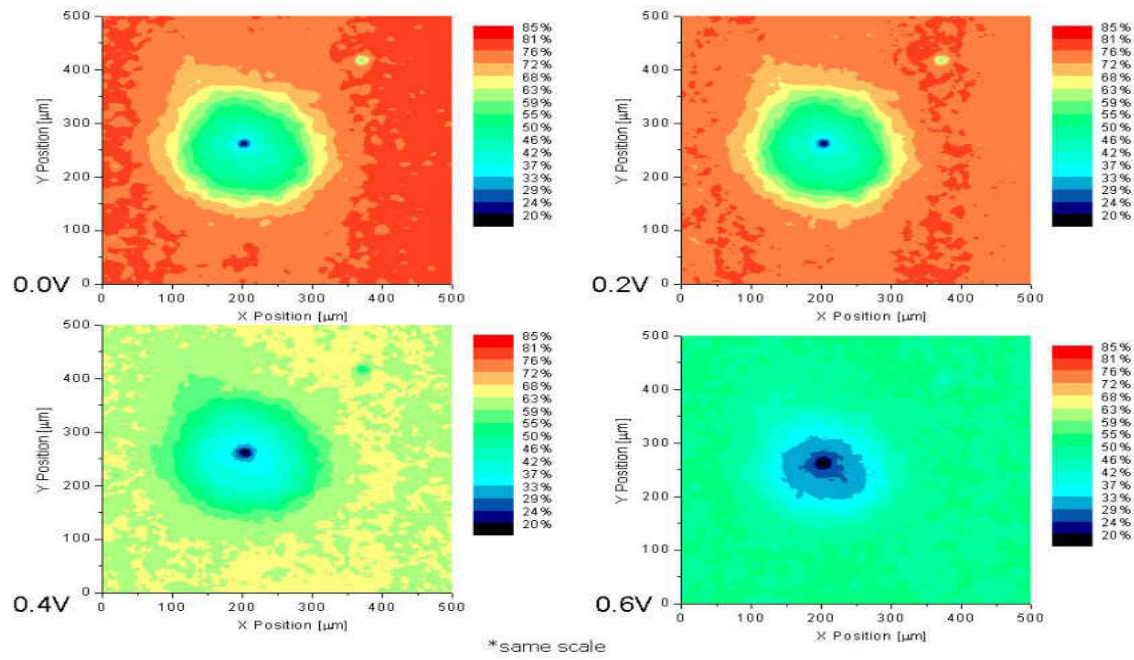


Figure 60 : High resolution of the square portion from Figure 59.

Figure 61 shows cross sections of the features. The shape of the cross section does not change with voltage, which suggests that it is not a local shunt. The fact that all points on the curve shift down by almost the same amount suggests that it might be an optical defect.



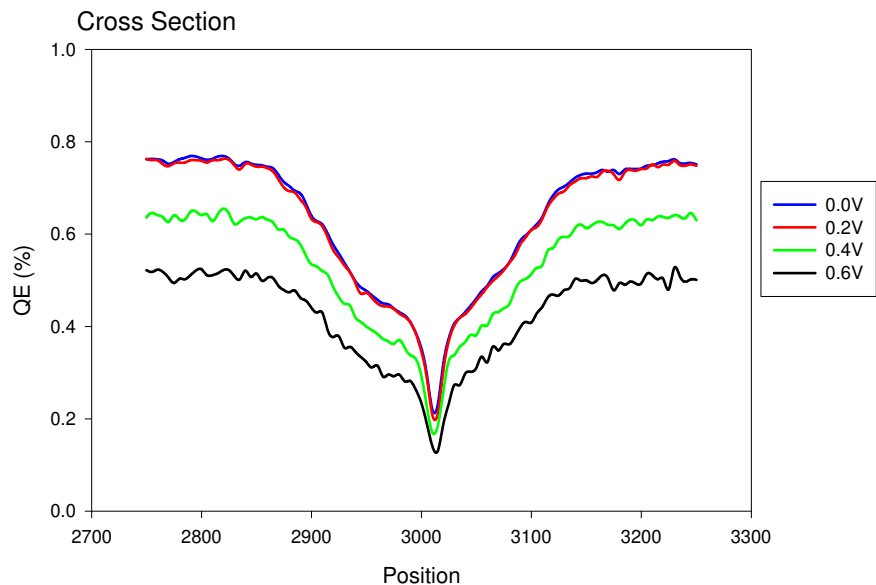


Figure 61 : Cross-sections of the features shown in Figure 60.

#### 4. B.7. Photovoltaic Characterization of the highest efficiency cells

Photovoltaic performance of CIGS2 thin film solar cells were studied using current-voltage (I-V) characteristics. The maximum efficiency measured for a sample of a 1.5  $\mu\text{m}$  absorber prepared using original parameters and no post-sulfurization dwell was 8.74% as explained earlier. This was due to predominate grain boundaries acting as recombination centers as elucidated in section 4.3.2. Using a post-sulfurization dwell, the efficiency was increased to 10.12% with other photovoltaic characteristics as follows: short circuit current density,  $J_{sc}$  of 19.46  $\text{mA}/\text{cm}^2$ , open circuit voltage,  $V_{oc}$  of 765.9 mV and fill factor, FF of 67.85%. Figure 62 shows the I-V characteristics of CIGS2 solar cell of 1.5  $\mu\text{m}$  absorber (with post-sulfurization dwell) measured at the National Renewable Energy Center (NREL) under AM1.5 conditions. Figure 63 shows QE characteristics. Figure 64 and Figure 65 exhibit I-V and QE characteristics for a 1.2  $\mu\text{m}$  absorber (with post-sulfurization dwell) respectively. Photovoltaic characteristics of the CIGS2 thin film solar cells (1.2  $\mu\text{m}$  absorber) were as follows: short circuit current density,  $J_{sc}$  of 18.94  $\text{mA}/\text{cm}^2$ , open circuit voltage,  $V_{oc}$  of 775.9 mV, fill factor, FF of 65.40% and photovoltaic conversion efficiency,  $\eta$  of 9.62%. The band-gap value of CIGS2 absorber as

calculated from the QE analysis is 1.495 eV. From the QE analysis it can be seen that the CdS heterojunction partner layer is well optimized as losses in  $<520$  nm (corresponding to CdS bandgap of 2.42 eV) wavelength are comparatively low. Also it can be seen from the QE analysis that absorber quality can be improved near the molybdenum back-contact to improve the collection efficiency in the long wavelength region. The curves are steep in the long wavelength region, showing the uniformity of composition.

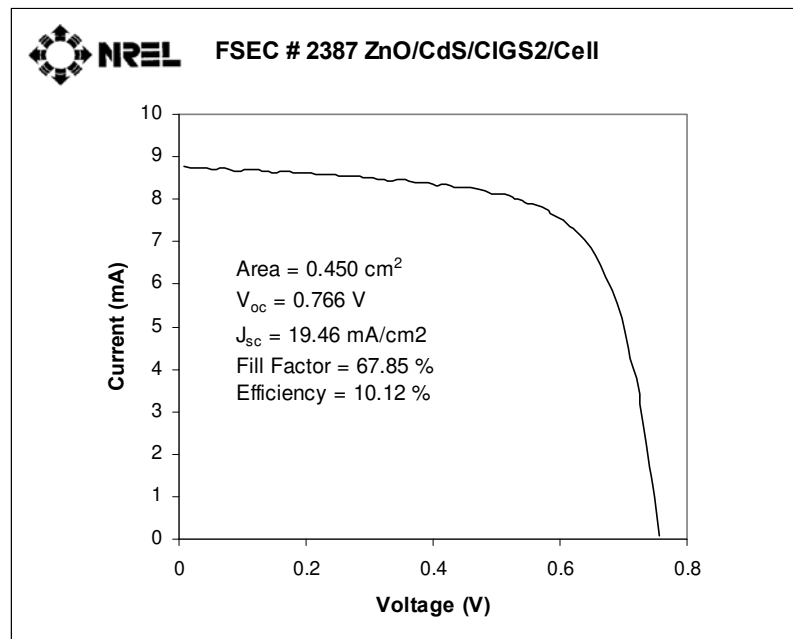


Figure 62 : I-V characteristics of CIGS2 solar cell of 1.5  $\mu$ m absorber (with end dwell)

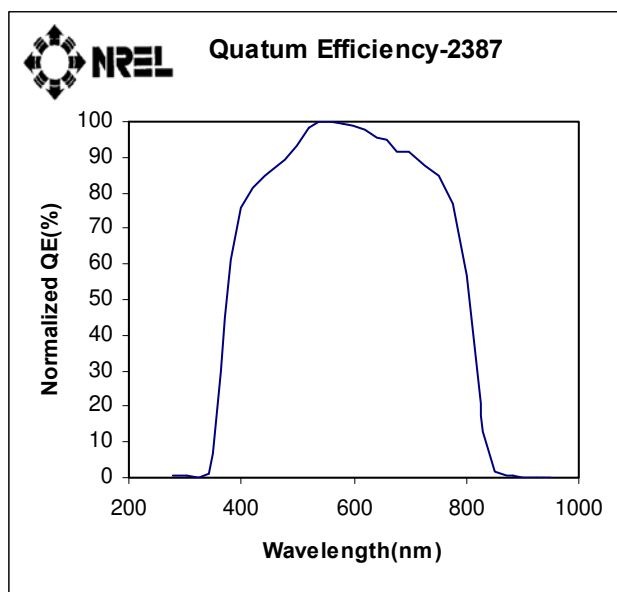


Figure 63 : Q-E characteristics of CIGS2 solar cell of 1.5  $\mu\text{m}$  absorber (with end dwell)

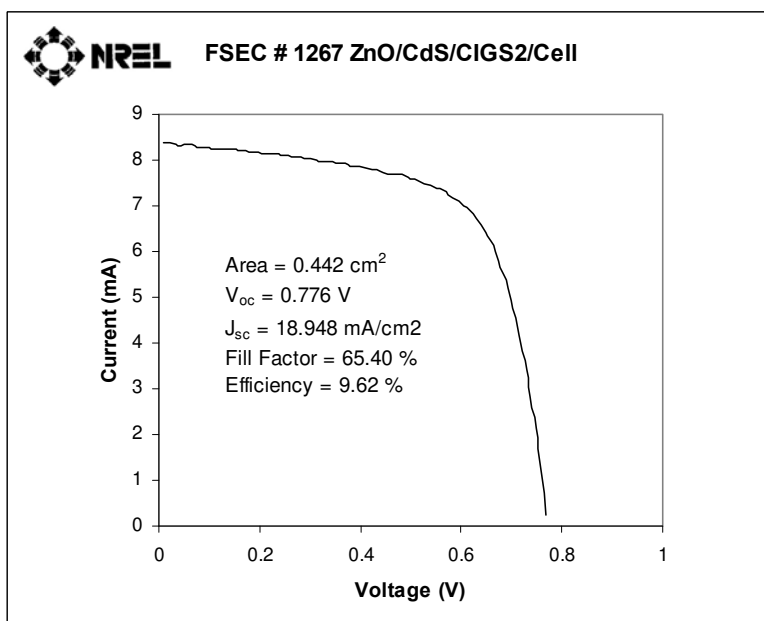


Figure 64 : I-V characteristics of CIGS2 solar cell of 1.2  $\mu\text{m}$  absorber (with end dwell)

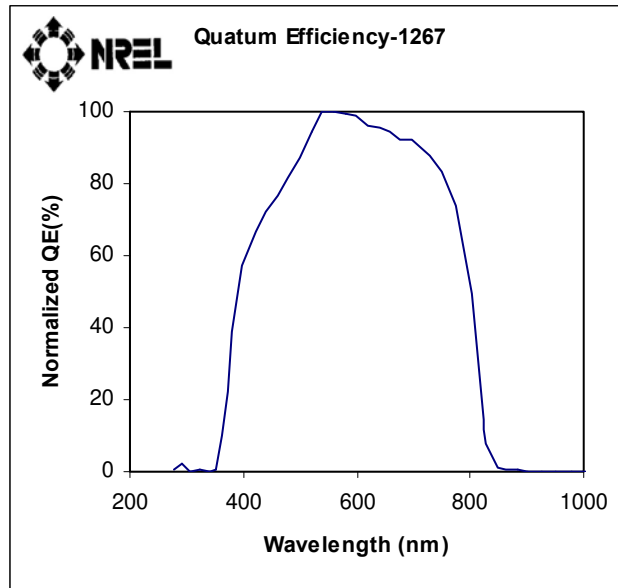


Figure 65 : Q-E characteristics of CIGS2 solar cell of 1.2  $\mu\text{m}$  absorber (with end dwell)

The trends in photovoltaic performance at various experimental stages are plotted in Figure 66. After initial stage of experiments, there was higher  $R_s$  ( $15 \Omega\text{-cm}$ ) and lower  $J_{sc}$  ( $12.6 \text{ mA/cm}^2$ ), resulting in lower efficiency (4.97%). After optimization of undoped ZnO,  $R_s$  is reduced ( $6.5\Omega\text{-cm}$ ), so  $J_{sc}$  ( $17.5 \text{ mA/cm}^2$ ), and efficiency (8.74%) increase. Finally, post-sulfurization annealing treatment leading to better grain size.  $J_{sc}$  ( $19.46 \text{ mA/cm}^2$ ), and efficiency (10.12%) increase further.

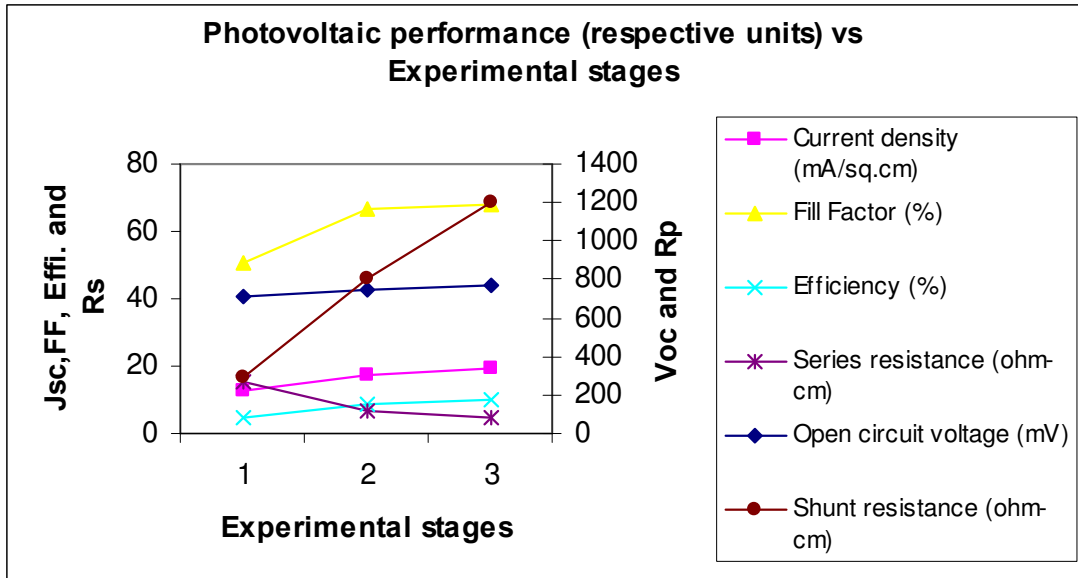


Figure 66 : Trends in photovoltaic performance towards optimization of 1.5  $\mu\text{m}$  Cu-rich CIGS2 films

## **5. CONCLUSIONS AND RECOMMENDATIONS FOR FUTURE WORK**

### **5.1 Conclusions**

This work is one of the very few attempts in which device quality films were prepared even in copper-deficient regimes with the addition of sodium. Efficiencies  $\sim 10\%$  have been reported for the first time with copper-deficient CIGS2 thin films. It was found that growing films in copper-deficient regimes produces large macroscopic defects. Sodium has played an important role in Cu-deficient absorbers in enhancing the mobilities of the species. Sodium addition has led to macroscopic defect reduction due to fluxing action. Fabrication of CIGS2 films has become easier and also less toxic due to removal of etching step by KCN.

Fabrication of copper-deficient CIGS2 thin films not only provides better control over composition range and consequently making their fabrication easier, but there is also a tremendous potential to perform a study on CIGS2 similar to the study by Nakada et al on CIGSe, and find out whether similar compositional flexibility can be achieved in CIGS2 thin films also. This will certainly add to the momentum generated in the present contribution due to compositional control by further widening of the compositional range and better flexibility in terms of composition. The wider process window will lead to a low-cost manufacturing.

Role of sodium in Cu-poor CIGS2 absorbers is manifested through the reduction in the defect density and a strong preferred (112) orientation. Substrates other than sodalime glass can also be effectively used due to this method. This has tremendous potential in terms of solar cells used on lighter substrates, where wide band gap solar cells like CIGS2 are used.

Due to fluxing action of sodium, higher mobilities of species can be obtained without the need of using very high sulfurization temperatures, thus avoiding excessive reaction of sulfur with molybdenum

Absorber thickness for Cu-rich CIGS2 films has been reduced in the range 1.2 to 1.5 microns and consistent efficiencies have been obtained (>10%). The highest efficiency for a 1.5 micron thick absorber cell is 10.12% and the highest efficiency for a 1.2 micron thick absorber cell is 9.68%. It can be deduced that low-cost thin film CIGS2 solar cells can be fabricated without losing significantly on the efficiency end. This will have a larger impact when these processes are scaled up to an industry level. Thinner absorber films results in lower consumption of indium and gallium, thus reducing the material requirements. Thinner absorbers also reduce the processing time and thus improving the throughput. CIGS2 solar cells were optimized by optimizing i:ZnO and by employing a post-sulfurization dwell for lower thickness values of absorber.

Following chart compares reduction in respective parameters when the absorber thickness is reduced from earlier highest efficient CIGS2 cell to CIGS2 cells in the present contribution:

Table II : Trade-off showing efficiency and material consumption/sputtering time

<b>Reduction in material consumption</b>	<b>Reduction in time for sputtering of precursors</b>	<b>Reduction in efficiency for the highest efficiency cell</b>
~56%	~60%	~15%

Materials characterization was carried out using SEM, EDAX, AES, XRD and TEM. Electrical characterization was carried out using I-V, C-V, QE and LBIC methods.

## **5.2. Recommendations for future work**

Exact quantification of the carrier concentrations in both copper-rich and copper-deficient absorbers will be an interesting idea for future work. Such a study will elucidate how the carrier concentration has changed with the addition of sodium. One of the limitations of the CIGS2 films has been that these films do not form a buried homojunction as those of CIGS films. This has been because typically the CIGS2 films have been grown in copper-rich regimes. Now since CIGS2 films have exhibited encouraging results even in copper-deficient regimes, it will be interesting to study as a part of future work whether a buried homojunction can be formed in CIGS2 films. Also the process parameters can be further fine-tuned for thinner copper-rich absorbers and a lower thickness value such as 0.9  $\mu\text{m}$  can be tried for getting better efficiencies.



## REFERENCES

- [1] M. Archer and R. Hill, *Clean Electricity from Photovoltaics.* , vol. 1, Imperial College Press, 2001,
- [2] J. Zhao, A. Wang, M. A. Green and F. Ferrazza, "19.8% efficient "honeycomb" textured multicrystalline and 24.4% monocrystalline silicon solar cells," *Applied Physics Letters*, vol. 73, pp. 1991, 1998.
- [3] S. W. Glunz, S. Rein, W. Warta, J. Knobloch and W. Wettling. (2001, 1). Degradation of carrier lifetime in cz silicon solar cells. *Solar Energy Materials and Solar Cells*, 65(1-4), pp. 219-229.
- [4] F. Pfisterer and W. H. Bloss. (1984, 0). Development of Cu<sub>2</sub>S/CdS thin film solar cells and transfer to industrial production. *Solar Cells*, 12(1-2), pp. 155-161.
- [5] N. G. Dhere. (1990, 12/15). Recent developments in thin film solar cells. *Thin Solid Films*, 193-194(Part 2), pp. 757-768.
- [6] Y. Hamakawa, *Thin Film Solar Cells – Next Generation Photovoltaics and its Application*. Springer-Verlag Berlin Heidelberg New York, 2004,
- [7] K. Ramanathan, M. A. Contreras, C. L. Perkins, S. Asher, F. S. Hasoon, J. Keane, D. Young, M. Romero, W. Metzger, R. Noufi, J. Ward and A. Duda. (2003, Properties of 19.2% efficiency ZnO/CdS/CuInGaSe<sub>2</sub> thin-film solar cells. *Prog Photovoltaics Res Appl* 11(4), pp. 225-230. Available: <http://dx.doi.org/10.1002/pip.494>

[8] J. S. Ward, K. Ramanathan, F. S. Hasoon, T. J. Coutts, J. Keane, M. A. Contreras, T. Moriarty and R. Noufi. (2002, A 21.5% efficient cu(in,ga)Se<sub>2</sub> thin-film concentrator solar cell. *Prog Photovoltaics Res Appl* 10(1), pp. 41-46. Available: <http://dx.doi.org/10.1002/pip.424>

[9] X. Wu, J. C. Keane, R. G. Dhere, C. DeHart, D. S. Albin, T. Duda, A. Gessert, S. Asher, D. H. Levi and P. Sheldon, *Proceedings of the 17th European Photovoltaic Solar Energy Conference*, 2002, pp. 995.

[10] A. L. Fahrenbruch and R. Bube, *Fundamentals of Solar Cells: Photovoltaic Solar Energy Conversion*. Academic Press, 1983,

[11] R. S. Muller, T. I. Kamins and M. Chan, *Device Electronics for Integrated Circuits*. ,3rd ed. John Wiley & Sons, 2002,

[12] A. Luque and S. Hegedus, *Handbook of Photovoltaic Science and Engineering*. John Wiley and Sons, 2003,

[13] O. Lundberg, M. Bodegård, J. Malmström and L. Stolt. (2003, Influence of the cu(in,ga)Se<sub>2</sub> thickness and ga grading on solar cell performance. *Prog Photovoltaics Res Appl* 11(2), pp. 77-88. Available: <http://dx.doi.org/10.1002/pip.462>

[14] S. G. Bailey and D. J. Flood, "Space Photovoltaics," *Progress in Photovoltaics: Research and Applications*, vol. 6, pp. 1-14, 1998.

[15] N. G. Dhere, S. R. Kulkarni, S. S. Chavan and S. R. ghongadi, "Cu(in,ga)S<sub>2</sub> thin-film solar cells prepared by H<sub>2</sub>S sulfurization of CuGa-in precursor," in *Proc. 16th Space Photovoltaic Research and Technology Conference (SPRAT XVI)*, 1999,

- [16] N. G. Dhere, S. R. Kulkarni and P. K. Johnson, "Bandgap optimization of CIGS<sub>2</sub> space solar cells," in *Proc. 16th European Photovoltaic Solar Energy Conference*, 2000,
- [17] D. J. Flood, "Advanced space solar cells," *Progress in Photovoltaics: Research and Applications*, vol. 6, pp. 187-192, 1998.
- [18] A. H. Jahagirdar and N. G. Dhere. (2007, 9/22). Photoelectrochemical water splitting using CuIn<sub>1-x</sub>Ga<sub>x</sub>S<sub>2</sub>/CdS thin-film solar cells for hydrogen generation. *Solar Energy Materials and Solar Cells*, 91(15-16), pp. 1488-1491.
- [19] R. Noufi, R. Axton, C. R. Herrington and S. Deb, " Electronic-properties versus composition of thin-films of CuInS<sub>2</sub> " *Applied Physics Letters*, vol. 45, pp. 668-670, 1984.
- [20] D. Rudmann, D. Brémaud, A. F. da Cunha, G. Bilger, A. Strohm, M. Kaelin, H. Zogg and A. N. Tiwari. (2005, 6/1). Sodium incorporation strategies for CIGS growth at different temperatures. *Thin Solid Films*, 480-481pp. 55-60.
- [21] D. Rudmann, G. Bilger, M. Kaelin, F. - . Haug, H. Zogg and A. N. Tiwari. (2003, 5/1). Effects of NaF coevaporation on structural properties of cu(in,ga)Se<sub>2</sub> thin films. *Thin Solid Films*, 431-432pp. 37-40.
- [22] K. Sakurai, A. Yamada, P. Fons, K. Matsubara, T. Kojima, S. Niki, T. Baba, N. Tsuchimochi, Y. Kimura and H. Nakanishi. (2003, 9). Adjusting the sodium diffusion into CuInGaSe<sub>2</sub> absorbers by preheating of Mo/SLG substrates. *Journal of Physics and Chemistry of Solids*, 64(9-10), pp. 1877-1880.

- [23] M. Igalson, A. Kubiacyk, P. Zabierowski, M. Bodegård and K. Granath. (2001, 5/29). Electrical characterization of ZnO/CdS/Cu(in,ga)Se<sub>2</sub> devices with controlled sodium content. *Thin Solid Films*, 387(1-2), pp. 225-227.
- [24] M. Lammer, U. Klemm and M. Powalla. (2001, 5/29). Sodium co-evaporation for low temperature cu(in,ga)Se<sub>2</sub> deposition. *Thin Solid Films*, 387(1-2), pp. 33-36.
- [25] D. Braunger, D. Hariskos, G. Bilger, U. Rau and H. W. Schock. (2000, 2/21). Influence of sodium on the growth of polycrystalline cu(in,ga)Se<sub>2</sub> thin films. *Thin Solid Films*, 361-362pp. 161-166.
- [26] G. E. Granata, J. R. Sites, S. Asher and R. J. Matson, "Quantitative incorporation of sodium in CuInSe<sub>2</sub> and cu(in,ga)Se<sub>2</sub> photovoltaic devices," in *26th PVSC* 1997, pp. 387-390.
- [27] T. Nakada, H. Ohbo, M. Fukuda and A. Kunioka. (1997, 12). Improved compositional flexibility of cu(in,ga)Se<sub>2</sub>-based thin film solar cells by sodium control technique. *Solar Energy Materials and Solar Cells*, 49(1-4), pp. 261-267.
- [28] I. Luck, J. Kneisel, K. Siemer, J. Bruns, R. Scheer, R. Klenk, N. Janke and D. Bräunig. (2001, 3). Influence of na on the properties of cu-rich prepared CuInS<sub>2</sub> thin films and the performance of corresponding CuInS<sub>2</sub>/CdS/ZnO solar cells. *Solar Energy Materials and Solar Cells*, 67(1-4), pp. 151-158.
- [29] T. Yamamoto, K. Fukuzaki and S. Kohiki. (2000, 6). Influence of incorporation of na on p-type CuInS<sub>2</sub> thin films. *Applied Surface Science*, 159-160pp. 345-349.
- [30] I. Luck, J. Kneisel, K. Siemer, J. Bruns, R. Scheer, R. Klenk, N. Janke and D. Bräunig. (2001, 3). Influence of na on the properties of cu-rich prepared CuInS<sub>2</sub> thin

films and the performance of corresponding CuInS<sub>2</sub>/CdS/ZnO solar cells. *Solar Energy Materials and Solar Cells*, 67(1-4), pp. 151-158.

[31] B. A. Anderson, C. Azar, J. Holmberg and S. Karlsson, "Material constraints for thin-film solar cells," *Energy*, vol. 23, pp. 407-411, 1998.

[32] J. L. Vossen and W. Kern, *Thin Film Processes*. Newyork academic press, 1978,

[33] K. Taretto, U. Rau and J. H. Werner. (2005, 6/1). Numerical simulation of grain boundary effects in cu(in,ga)Se<sub>2</sub> thin-film solar cells. *Thin Solid Films*, 480-481pp. 8-12.

[34] S. Siebentritt and U. Rau, *Wide-Gap Chalcopyrites*. Newyork: Springer, 2005,

[35] A. N. Tiwari, D. K. Pandya and K. L. Chopra. (1987, 2). Analysis of the photovoltaic properties of sprayed CuInS<sub>2</sub>/SnOx: F solar cells. *Solar Energy Materials*, 15(2), pp. 121-133.

[36] G. Hodes, T. Engelhard, D. Cahen, L. L. Kazmerski and C. R. Herrington. (1985, 6/14). Electroplated CuInS<sub>2</sub> and CuInSe<sub>2</sub> layers: Preparation and physical and photovoltaic characterization. *Thin Solid Films*, 128(1-2), pp. 93-106.

[37] Y. Onuma, K. Takeuchi, S. Ichikawa, Y. Suzuki, R. Fukasawa, D. Matono, K. Nakamura, M. Nakazawa and K. Takei. (2006, 1). Preparation and properties of CuInS<sub>2</sub> thin film prepared from electroplated precursor. *Solar Energy*, 80(1), pp. 132-138.

[38] A. Antony, A. S. Asha, R. Yoosuf, R. Manoj and M. K. Jayaraj. (2004, 3/1). Growth of CuInS<sub>2</sub> thin films by sulphurisation of Cu- In alloys. *Solar Energy Materials and Solar Cells*, 81(4), pp. 407-417.

- [39] S. Bandyopadhyaya, S. Chaudhuri and A. K. Pal. (2000, 2/1). Synthesis of CuInS<sub>2</sub> films by sulphurization of Cu/In stacked elemental layers. *Solar Energy Materials and Solar Cells*, 60(4), pp. 323-339.
- [40] N. G. Dhere and S. R. ghongadi, "CIGS<sub>2</sub> thin film solar cells on stainless steel foil," in *Mat. Res. Soc. Symp. Proc.* 2001, pp. H3.4.1-H3.4.6.
- [41] N. G. Dhere, S. R. ghongadi, M. B. pandit, A. A. Kadam, A. H. Jahagirdar and V. S. Gade, "AFM, micro-PL, and PV analyses of CuIn<sub>1-x</sub>GaxS<sub>2</sub> thin films solar cells on stainless steel foil," in *IEEE PVSEC*, 2002, pp. 876-879.
- [42] K. Müller, S. Milko and D. Schmeißer. (2003, 5/1). Preparation of stoichiometric CuInS<sub>2</sub> surfaces—an XPS and UPS study. *Thin Solid Films*, 431-432pp. 312-316.
- [43] K. Müller, R. Scheer, Y. Burkov and D. Schmeißer. (2004, 3/22). Preparation of stoichiometric CuInS<sub>2</sub> surfaces. *Thin Solid Films*, 451-452pp. 120-123.
- [44] Y. Ogawa, A. Jäger-Waldau, Y. Hashimoto and K. Ito, "In<sub>2</sub>O<sub>3</sub>/CdS/CuInS<sub>2</sub> Thin-Film Solar Cell with 9.7% Efficiency," *Japanese Journal of Applied Physics*, vol. 33, pp. L1775-L1777, 1994.
- [45] R. Scheer, R. Klenk, J. Klaer and I. Luck. (2004, 12). CuInS<sub>2</sub> based thin film photovoltaics. *Solar Energy*, 77(6), pp. 777-784.
- [46] T. Watanabe and M. Matsui, "Solar Cells Based on CuInS<sub>2</sub> Through Sulfurization of Precursors Prepared by Reactive Sputtering H<sub>2</sub>S Gas," *Japanese Journal of Applied Physics*, vol. 35, pp. L1681-L1684, 1996.

- [47] R. P. Wijesundera and W. Siripala. (2004, 2/6). Preparation of CuInS<sub>2</sub> thin films by electrodeposition and sulphurisation for applications in solar cells. *Solar Energy Materials and Solar Cells*, 81(2), pp. 147-154.
- [48] R. Scheer, M. Alt, I. Luck and H. J. Lewerenz. (1997, 12). Electrical properties of coevaporated CuInS<sub>2</sub> thin films. *Solar Energy Materials and Solar Cells*, 49(1-4), pp. 423-430.
- [49] R. Scheer and H. J. Lewerenz. (1995, July-Aug.). Formation of secondary phases in evaporated CuInS<sub>2</sub> thin films: A surface analytical study. *J Vac Sci Technol A* 13(4), pp. 1924-1929.
- [50] R. Scheer and H. J. Lewerenz. (1994, Photoemission study of evaporated CuInS<sub>2</sub> sub 2 thin films: I, surface stoichiometry and phase segregation. *Journal of Vacuum Science and Technology A* 12(1), pp. 51-55.
- [51] R. Scheer, I. Luck, S. hessler, H. Sehnert and H. J. Lewerenz, "Binary phase segregation in CuInS<sub>2</sub> thin films for efficient solar energy conversion," in *First WCPEC*, 1994, pp. 160-163.
- [52] R. Scheer, I. Luck, H. Sehnert and H. J. Lewerenz. (1996, 6). Scavenging of excess cu atoms in CuInS<sub>2</sub> films by sulphur annealing. *Solar Energy Materials and Solar Cells*, 41-42pp. 261-270.
- [53] R. Scheer, T. Walter, H. W. Schock, M. L. Fearheiley and H. J. Lewerenz. (1993, 13 Dec.). CuInS<sub>2</sub> based thin film solar cell with 10.2 percent efficiency. *Appl. Phys. Lett.* 63(24), pp. 3294-3296.

- [54] Y. L. Wu, H. Y. Lin, C. Y. Sun, M. H. Yang and H. L. Hwang. (1989, 1/1). On the growth of CuInS<sub>2</sub> thin films by three-source evaporation. *Thin Solid Films*, 168(1), pp. 113-122.
- [55] M. Kemell, M. Ritala and M. Leskela, "Thin film deposition methods for CuInSe<sub>2</sub> solar cells," *Critical Reviews in Solid State and Materials Sciences*, vol. 30, pp. 1-31, 2005.
- [56] T. Godecke, T. Haalboom and F. Ernst, "Phase equilibria of Cu-In-Se I. Stable States and Nonequilibrium States of the In<sub>2</sub>Se<sub>3</sub>-Cu<sub>2</sub>Se Subsystem," *Zeitschrift Fur Metallkunde*, vol. 8, pp. 622-634, 2000.
- [57] R. Ahuja, S. Auluck, O. Eriksson, J. M. Wills and B. Johansson. (1998, 6/10). Calculated optical properties of a solar energy material: CuGaS<sub>2</sub>. *Solar Energy Materials and Solar Cells*, 53(3-4), pp. 357-366.
- [58] S. J. Fonash, *Solar Cell Device Physics*. Academic press Newyork, 1981,
- [59] U. Rau, M. Schmidt, A. Jasenek, G. Hanna and H. W. Schock. (2001, 3). Electrical characterization of cu(in,ga)Se<sub>2</sub> thin-film solar cells and the role of defects for the device performance. *Solar Energy Materials and Solar Cells*, 67(1-4), pp. 137-143.
- [60] T. Halboom, T. Godecke, F. Ernst, M. Ruhle, R. Herberholz, H. -. Schock, C. Beilharz and K. W. Benz, "Phase relations and microstructure in bulk materials and thin films of the ternary system cu-in-se," in *Proceedings 11th International Conference on Ternary and Multinary Compounds*, 1997, pp. 249-252.
- [61] K. L. Chopra and S. R. Das, *Thin Film Solar Cells*. Plenum press – New York, 1983,



- [62] R. W. Birkmire and E. Eser, "Polycrystalline Thin Film Solar Cells: Present Status and Future Potential," *Annual Review of Material Science*, vol. 27, pp. 625, 1997.
- [63] I. Kaur, D. K. Pandya and K. L. Chopra, "Growth Kinetics and Polymorphism of Chemically Deposited CdS Films," *Journal of Electrochemical Society*, vol. 127, pp. 940, 1987.
- [64] S. Ishizuka, K. Sakurai, A. Yamada, K. Matsubara, P. Fons, K. Iwata, S. Nakamura, Y. Kimura, T. Baba, H. Nakanishi, T. Kojima and S. Niki. (2005, 5). Fabrication of wide-gap  $\text{Cu}(\text{In}_{1-x}\text{Ga}_x)\text{Se}_2$  thin film solar cells: A study on the correlation of cell performance with highly resistive i-ZnO layer thickness. *Solar Energy Materials and Solar Cells*, 87(1-4), pp. 541-548.
- [65] B. Sang, K. Kushiya, D. Okumura and O. Yamase. (2001, 3). Performance improvement of CIGS-based modules by depositing high-quality Ga-doped ZnO windows with magnetron sputtering. *Solar Energy Materials and Solar Cells*, 67(1-4), pp. 237-245.
- [66] U. Rau and H. W. Schock, "Electronic properties of  $\text{Cu}(\text{In,Ga})\text{Se}_2$  heterojunction solar cells-recent achievements,current understanding, and future challenges," *Applied Physics A*, vol. 69, pp. 131-147, 1999.
- [67] N. G. Dhere, A. H. Jahagirdar and S. R. Ghongadi, "Performance analysis of CIGS2 thin film solar cells based on semiconductor properties," in *Proceedings of SPIE*, pp. 665104-1.

[68] A. H. Jahagirdar, A. A. Kadam and N. G. Dhere, "Role of i-ZnO in optimizing open circuit voltage of CIGS2 and CIGS thin film solar cells," in *IEEE 4th World Conference on Photovoltaic Energy Conversion*, 2006, pp. 557-559.

[69] M. A. Contreras, M. J. Romero and R. Noufi. (2006, 7/26). Characterization of cu(in,ga)Se<sub>2</sub> materials used in record performance solar cells. *Thin Solid Films*, 511-512pp. 51-54.